

Development of All-Organic Magnetic Mixed Micelles Aiming at Biomedical Application

Kota Nagura

論 文 要 旨

論文題目 Development of All-Organic Magnetic Mixed Micelles Aiming at Biomedical Application
(生物医療応用を目指した純有機磁性混合ミセルの開発)

申請者 名倉康太

論文要旨 最近、五員環ニトロキシドラジカルをスピンソースとする純有機ラジカル液晶化合物が、低磁場存在下の液晶状態で強い磁気相互作用（「正の磁気液晶効果」と命名）を示すことが報告された。その原因として、液晶中で隣接ラジカル分子間に働くスピン分極により、スピングラス様の不均一な磁気ドメイン構造が形成された可能性が高いと考えられている。そこで申請者は、長鎖アルキル側鎖を有する五員環ニトロキシドラジカル化合物を、同様の長鎖アルキル側鎖を有する界面活性剤カプセルに内包させることができれば、両者のアルキル側鎖間の疎水性相互作用とラジカル間の CH/π や CH/O 相互作用により、安定な磁性混合ミセルが生成すると予想した。本ミセルが得られた場合、その応用範囲は広いと考えられる。特に申請者が注目したのは、磁気共鳴画像（MRI）法により追跡可能な薬剤送達システム（DDS）のキャリアとしての利用である。これまで、同様の目的でマグネタイトやガドリニウムなどの金属イオンをスピン源として用いた磁性ナノ粒子の開発が行われてきたが、純有機ナノ粒子の報告例はなかった。

申請者は界面として長鎖アルキル基をもつポリエチレングリコール（PEG）系の非イオン性界面活性剤を用い、これと同程度の鎖長のアルキル側鎖をもつ種々のラジカル誘導体を合成し、ミセルの調製を試みた。その結果、安定な混合ミセルを得るとともに、疎水性蛍光色素や抗癌剤の内包に成功し、さらに、それらの生物医療応用も検討した。

本論文は4章で構成されている。第一章は序論であり、常磁性液晶化合物が示す「正の磁気液晶効果」のメカニズムと磁性混合ミセル設計の経緯について述べる。

第二章では、界面活性剤として棒状構造を有する界面活性剤 Brij 58 と長鎖アルキル側鎖を持つラジカルから調製された安定な混合ミセルの作製とその MRI 造影剤としての応用について述べる。

第三章では、第二章で確立した混合ミセル調製法に基づいて、さらに低毒性の混合ミセルの調製を行い、これらミセルの構造、安定性、生物医療応用について検討した結果を述べる。

第四章では、末端にグルコースを有する新規ラジカル化合物を内包させた混合ミセルの調製を行い、MRI 造影能力の著しい増強が確認されたことから、それをマウスのイメージングへ応用した結果について述べる。

以上、磁性混合ミセルの安定性、還元耐性、安全性、MRI 造影能、さらには、蛍光剤、抗がん剤を内包した磁性混合ミセルのそれらについても明らかにし、マウスのイメージングにも成功した。今後、本磁性混合ミセルが MRI 造影能を有する薬剤送達キャリアとして臨床応用されることが期待される。

Table of contents

Chapter 1: Introduction	6
1-1. Ferromagnetic organic radical crystals	6
1-2. Discovery of positive magneto-LC effect	6
1-3. Magnetic nanoparticles	10
1-4. Aim of this study	13
Chapter 2: Preparation of metal-free magnetic mixed micelles encapsulating low-molecular-weight nitroxide radicals and hydrophobic drugs directed toward MRI-visible targeted delivery	14
2-1. Introduction	14
2-2. Results and discussion	16
2-2-1. Preparation and colloidal stability of magnetic mixed micelles	16
2-2-2. Reduction resistance to ascorbic acid	21
2-2-3. DDS carrier ability	22
2-2-4. <i>In vitro</i> cytotoxicity	25
2-2-5. MRI measurement	26
2-3. Conclusions	29
2-4. Experimental section	30
2-4-1. Materials	30
2-4-2. Synthesis of nitroxide radical compounds 9_n	30
2-4-3. Preparation of magnetic mixed micelles in PBS	31
2-4-3-1. 6/9_n , 6/10 , 7/9_n and 8/9_n	31
2-4-3-2. 6/9₁₈/11 , 6/9₁₈/12 , 6/9₁₈/13 and 6/9₁₈/14	31
2-4-3-3. 6/9₁₈/15	32
2-4-4. DLS measurement	32
2-4-5. EPR spectroscopy	32
2-4-5-1. EPR measurement	32
2-4-5-2. Reduction resistance of the mixed micelles to excess ascorbic acid (VC)	
2-4-6. SANS measurement	33

2-4-7. UV and fluorescence spectroscopy	33
2-4-8. Evaluation method of <i>in vitro</i> cytotoxicity	33
2-4-9. <i>In vitro</i> MRI measurement	34
2-4-10. Animal study	34
2-4-11. <i>In vivo</i> MRI measurement of the mouse brain.....	34

Chapter 3: Size-tunable MRI-visible nitroxide-based magnetic mixed micelles: Preparation, stability, structure and theranostic application..... 36

3-1. Introduction	36
3-2. Results and discussion	38
3-2-1. Preparation and stability	38
3-2-1-1. Preparation and stability of magnetic mixed micelles of 18/9_n and 19/9_n ..	38
3-2-1-2. Preparation and stability of magnetic mixed micelles of 18/9₁₈/X	43
3-2-1-3. Stability of magnetic mixed micelles in the presence of a reducing agent ..	44
3-2-2. Theranostic application	45
3-2-2-1. <i>In vitro</i> cytotoxicity of magnetic mixed micelles against HeLa cell.....	45
3-2-2-2. MRI experiment.....	46
3-3. Conclusions	53
3-4. Experimental section	54
3-4-1. Materials	54
3-4-2. Preparation of magnetic magnetic mixed micelles in PBS.....	54
3-4-2-1. Magnetic mixed micelles.....	54
3-4-2-2. Magnetic mixed micelles containing guest (X)	54
3-4-2-2-1. X : Fluorophores	54
3-4-2-2-2. X : Anti-cancer drug	54
3-4-3. Characterization of magnetic mixed micelles	55
3-4-3-1. DLS measurement.....	55
3-4-3-2. SANS measurement	55
3-4-3-3. Fluorescence spectroscopy	57
3-4-3-4. EPR spectroscopy	57
3-4-3-4-1. EPR measurement.....	57
3-4-3-4-2. Determination of the magnetic mixed micelles reduction resistance to excess ascorbic acid	57
3-4-3-4-3. Fitting procedure for slow-and fast-motion EPR spectra.....	57

3-4-3-4-4. Calculation of the inertia tensors and the intramolecular rotation energy barriers for nitroxide radical.....	58
3-4-4. Evaluation method of <i>ini vitro</i> cytotoxicity	58
3-4-5. <i>In vitro</i> MRI measurement	59
3-4-6. <i>In vivo</i> MRI measurement.....	59
3-4-6-1. Animal preparations	59
3-4-6-2. <i>In vivo</i> MRI acquisition.....	59
3-4-7. TEM study.....	60
3-5. Appendix	61
3-5-1. Structural characterization of the magnetic mixed micelle 18/9 ₁₈	61
3-5-2. Results of EPR spectral simulation	65
3-5-3. TEM study of 18/9 ₁₈	72

Chapter 4: Magnetic Mixed Micelles Composed of Tween 80 and Nitroxide Radicals containing a Glucose Unit: Preparation, Properties and Application..... 74

4-1. Introduction	74
4-2. Results and discussion	76
4-2-1. Preparation, stability and in vitro MRI contrast ability of 18/20 _n	76
4-2-2. Reduction resistivity of 18/20 ₁₄ in the presence of ascorbic acid.....	82
4-2-3. Biomedical application of 18/20 ₁₄	83
4-3. Conclusions	86
4-4. Experimental section	87
4-4-1. General	87
4-4-2. Synthesis	87
4-4-3. Preparation of magnetic mixed micelles 18/20 _n (<i>n</i> = 14, 16 and 18) in PBS	89
4-4-4. DLS measurement.....	90
4-4-5. EPR spectroscopy	90
4-4-5-1. Determination of rotation diffusion coefficient (<i>D</i> _z).....	90
4-4-5-2. Measurement of reduction resistance of the mixed micelles to a large excess of ascorbic acid	90
4-4-6. Evaluation method of <i>in vitro</i> cytotoxicity	91
4-4-7. <i>In vivo</i> toxicology test	91
4-4-8. Evaluation method of <i>in vitro</i> MRI experiment	91

4-4-9. <i>In vivo MRI experiment</i>	92
4-5. Appendix	93
4-5-1. Stability of 6/20_n	93
4-5-2. Results of EPR spectral simulation	94
References	102
List of publications and patent	110
Acknowledgement	111

1-1. Ferromagnetic organic radical crystals

Since the discovery of the purely organic ferromagnet (critical temperature, $T_c = 0.6$ K) with respect to one of the several polymorphs of 2-(4-nitrophenyl)-4,4,5,5-tetramethylimidazolin-1-oxy-3-oxide by Kinoshita et al. in 1991 (Figure 1-1a), nitroxide radicals have been used as the spin source to develop all-organic solid magnetic materials [1,2,3,4]. In this molecular design, it was emphasized that the McConnell-type strong ferromagnetic interactions were required to lead to effective intermolecular spin-spin exchange. Although, up to the late 1990s, more than twenty nitroxide-based organic ferromagnets were reported [5], these organic nitroxide radical materials exhibited a paramagnetic behavior above the very low T_c due to the smaller intermolecular spin-spin exchange interaction than thermal energy. Thus far, the highest T_c value of 1.48 K was recorded for one of polymorphs of 1,3,5,7-tetramethyl-2,6-diazaadamane- N,N' -dioxyl prepared by Rassat et al. in 1993 (Figure 1-1b).

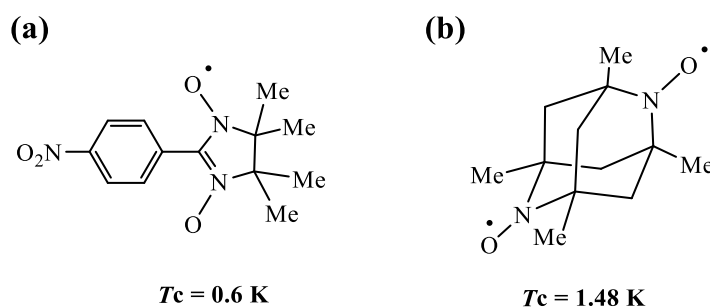


Figure 1-1. Molecular structures of all-organic ferromagnets. (a) 2-(4-nitrophenyl)-4,4,5,5-tetramethylimidazolin-1-oxy-3-oxide and (b) 1,3,5,7-tetramethyl-2,6-diazaadamane- N,N' -dioxyl prepared by Kinoshita and Rassat, respectively.

1-2. Discovery of positive magneto-LC effect

In general, the possibility of a ferromagnetic rod-like liquid crystalline (LC) material was considered unrealistic due to the inaccessibility of strong spin-spin dipole and exchange interactions between molecules which is caused by fast molecular rotation ($10^8 - 10^{10} \text{ s}^{-1}$) around the molecular long axis in the LC state [6], although theoretical considerations on the existence and dynamics of ferromagnetic liquid crystals had been reported [7]. In fact, there was no report on the observation of ferromagnetic interaction in metal-containing liquid crystals (metallomesogens) [8,9].

However, since 2008 it has been revealed that a sort of spin glass (SG)-like inhomogeneous magnetic interactions (average spin-spin exchange interaction constant $\bar{J} > 0$) occur in the various chiral or achiral, rod-like LC phases [nematic (N), chiral nematic (N^*), smectic C (SmC), and chiral smectic C (SmC*)] [10] shown in Figure 1-2 of monoradical compounds under low magnetic fields

(< 0.1 T), which contain a stable chiral five-membered nitroxide unit in the central core position and thereby possess a negative dielectric anisotropy ($\Delta\epsilon < 0$) [11,12,13,14].

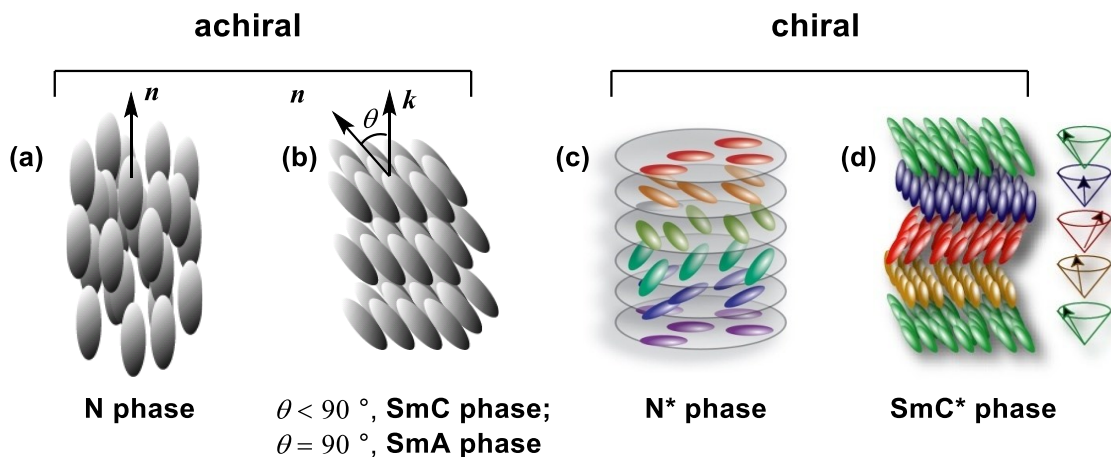


Figure 1-2. Molecular alignment of (a) N, (b) SmC, (c) N* and (d) SmC* phases. n denotes a director vector of a molecule, k represents a layer normal [10].

For example, all-organic radical liquid crystalline compound **1** was found to show superparamagnetic interactions ($\bar{J} > 0$) in the LC phases (Figure 1-3) [11]. Namely, a linear relation between H and M was not observed in all of the four LC phases of **1a** and **b**. However, they drew an S-curve which passed through the origin. These results by SQUID magnetometry indicated that no spontaneous magnetization occurred at a zero magnetic field. In addition, the deviation of the magnetization from the linearity under weak magnetic fields implied the generation of superparamagnetic interactions in applied magnetic fields. In contrast, such a superparamagnetic behavior was not observed in the crystalline phase of the same compounds before heating to the LC phases. This unique magnetic phenomenon, an increase in the molar magnetic susceptibility (χM) at the crystal-to-liquid crystal phase transition, was referred to as “positive magneto-LC effect” [11].

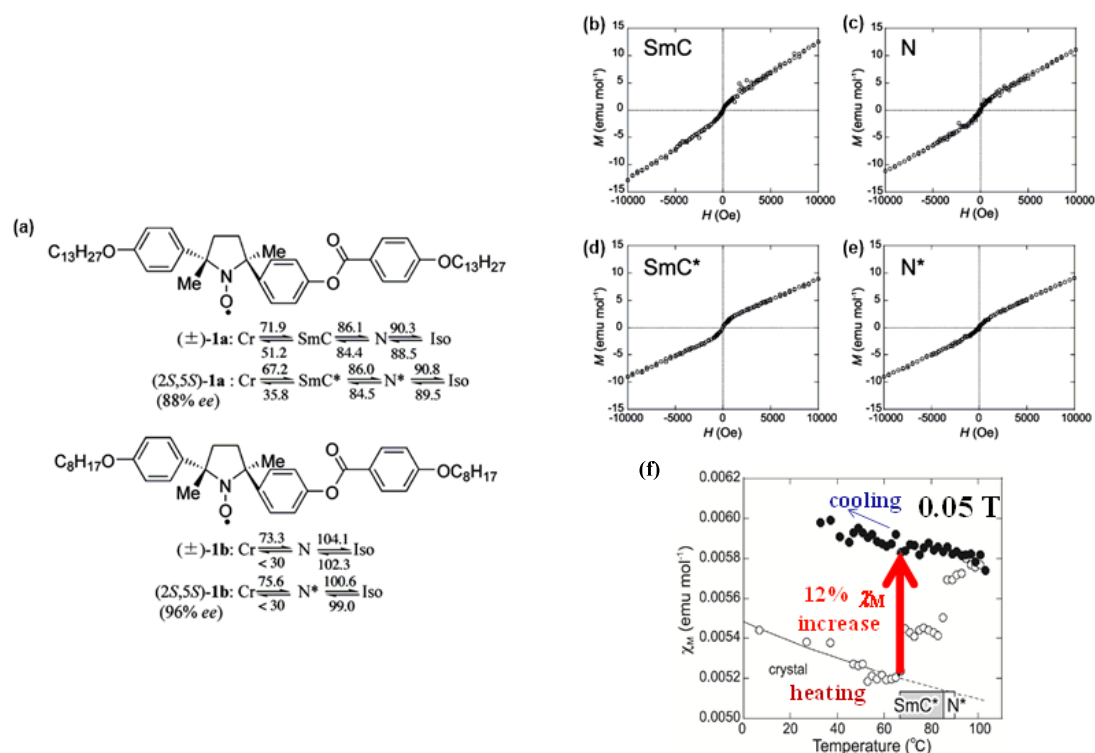


Figure 1-3. (a) Molecular structures of **1** and magnetic field (H) dependence of molar magnetization (M) at 77 °C for (b) the SmC phase of (\pm)-**1a**, (c) the N phase of (\pm)-**1b**, (d) the SmC* phase of (2*S*,5*S*)-**1a** (88% *ee*) and (e) the N* phase of (2*S*,5*S*)-**1b** (96% *ee*), and (f) temperature dependence of molar magnetic susceptibility (χ_M) at 0.05 T of (2*S*,5*S*)-**1a** (88% *ee*). In panel f, open and filled circles represent heating and cooling runs, respectively. Reprinted with permission from ref. 11. Copyright 2019 American chemical Society.

Electron paramagnetic resonance (EPR) spectroscopy and discrete Fourier transformation (DFT) calculations correlated this unique magnetic phenomenon with the preferential occurrence of ferromagnetic spin–spin dipole interactions in magnetic fields by a spin-polarization mechanism due to the inhomogeneous intermolecular contacts through CH/ π and/or CH/O interactions between neighboring cyclic nitroxide radical moieties [15]. Calculation for the molecular pair presented in Figure 1-4 proved that appreciable spin density is transferred on the distant aromatic ring in one molecule of the pair. This spin polarization mechanism is most likely responsible for the generation of the positive magneto-LC effect [15].

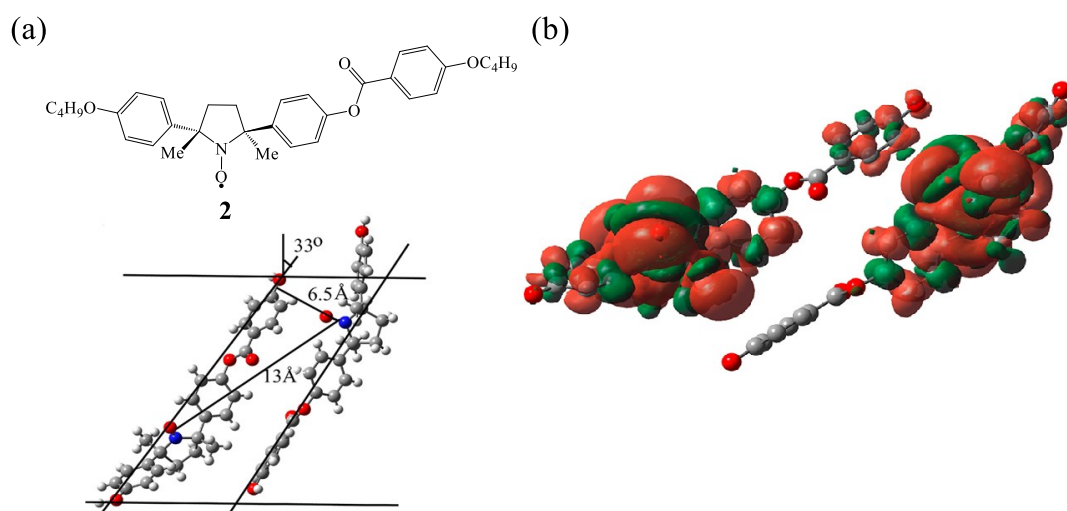


Figure 1-4. (a) Relative position of a pair of molecules in the crystal structure of (*S,S*)-**2** and (b) spin density distribution in the same pair by DFT calculation. Reprinted with permission from ref. 15. Copyright 2019 American chemical Society.

Furthermore, quite recently it has been revealed that the origin of the positive magneto-LC effect, or the superparamagnetic behavior, was interpreted in terms of the formation of organic spin glasses by investigating the magnetic properties of biradical (**3**) [13] and diradical LC (**4**) compounds (Figure 1-5) [14].

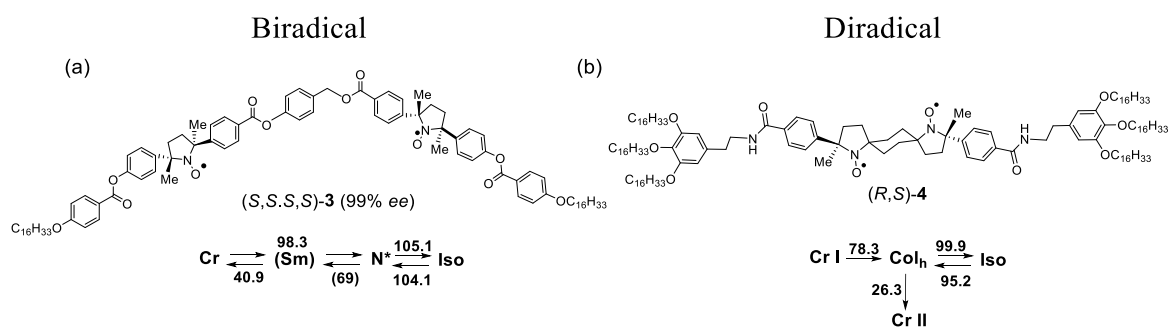


Figure 1-5. Molecular structures of (*S,S,S,S*)-**3** and (*R,S*)-**4**.

We expected that these results described above would provide an important information for the development of metal-free magnetic advanced soft materials, such as magneto-active nanoparticles which are expected to be used for biomedical applications including magnetically transportable oxidation and reduction resistant magnetic microcarriers, magnetic resonance imaging (MRI) contrast agents and magnetic nanocarriers for a magnetically targeted drug delivery system (DDS), in place of metal-based magnetic nanoparticles. Indeed, Uchida et al. tackled on the extension of this unique magnetic phenomenon and successfully prepared microcapsules (diameter: 300 μm) comprised of

monodispersed core-shell water-in-oil-in-water (W/O/W) double-emulsion droplets of liquid nitroxide radical **5** [16]. These droplets were magnetically transportable and served as flexible antioxidative magnetic carriers for ondemand cargo-transport systems and droplet-based sensors.

On the basis of this experimental result and the spin density of **5** by DFT calculations, it was anticipated that similar superparamagnetic magnetic interactions might occur through intermolecular CH/ π and/or CH/O interactions between molecules of **5** or analogous nitroxide compounds bearing a long alkyl chain inside a nanocapsule composed of a surfactant to give stable magnetic nanoparticles (Figure1-6).

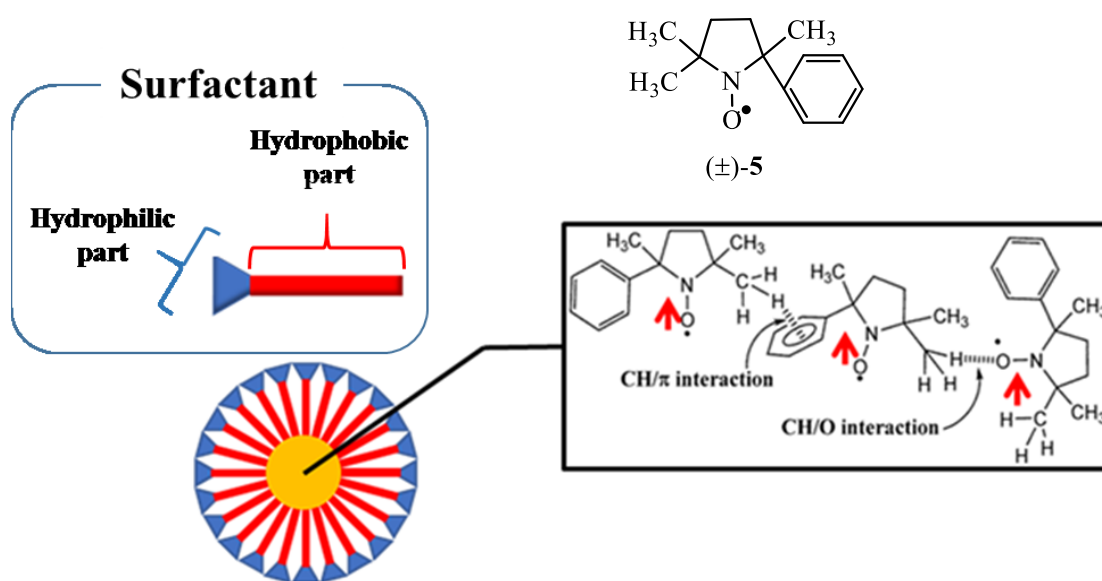


Figure 1-6. Possible CH/ π and CH/O interactions between the neighboring molecules of (\pm)-**5** in a nanocapsule.

1-3. Magnetic nanoparticles

Magnetic nanoparticles have attracted tremendous interest, particularly in biomedical applications such as drug-delivery systems (DDS) and contrast enhancement for magnetic resonance imaging (MRI) [17,18,19]. The majority of nanoparticles used in these applications are superparamagnetic iron oxides (magnetite Fe_3O_4 or maghemite $\gamma\text{Fe}_2\text{O}_3$) or iron-iron oxide core-shell complexes, which are coated with a variety of polymeric or monomeric materials to prevent aggregation and sedimentation of the nanoparticles [20,21,22,23,24,25,26,27,28,29] (Figure 1-7). In practice, these iron-containing nanoparticles, which are utilized as ferrofluids comprised of magnetic colloidal particles (particle size <100 nm) dispersed in a carrier fluid, can act as proton transverse relaxation time (T_2)-enhancing MRI contrast or hyperthermia therapy agents. To employ these magnetic nanoparticles in DDS, various drug molecules were attached to the biocompatible polymer, silica layer, or phospholipid bilayer coating on the magnetic core. The use of such magnetic nanoparticles enables the simultaneous

delivery and detection of therapeutic agents *in vivo*. However, there are some drawbacks associated with iron oxide based contrast agents because they demonstrate unusual magnetic susceptibility artifacts, which produce dark signals that may not only be misleading but also result in incorrect interpretation of the T_2 -weighted MRI.

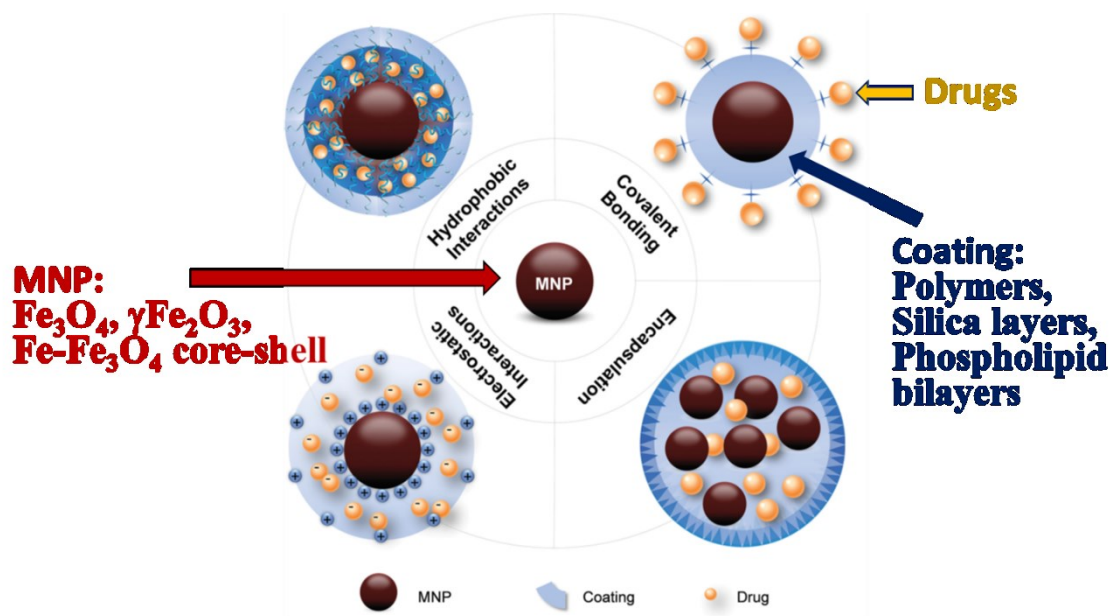


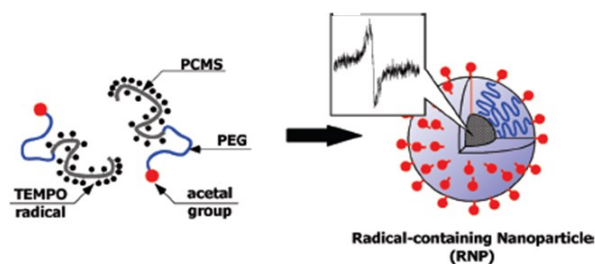
Figure 1-7. Typical examples of iron-loaded magnetic nanoparticles ($< 100 \text{ nm } \phi$). Reprinted with permission from ref. 20. Copyright 2019 Wiley VCH.

Meanwhile, core-shell organic radical nanoparticles have been fabricated as biocompatible high-performance metal-free magnetic nanoparticles to be used as MRI and EPR imaging probes *in vivo* [30,31,32]. They comprise a self-assembled amphiphilic copolymer with stable nitroxide radical groups covalently bonded to the hydrophobic segment and show high resistance to bioreduction. These polymeric nanoparticles have specific requirements, such as degradability and accurate molecular weight as well as nontoxicity and biocompatibility, that must be satisfied [32] (Figure 1-8a). Another example of metal-free magnetic nanoparticles employed as MRI contrast agents is low-toxicity lyotropic mesophase (hexagonal phase) nanoparticles (hexosomes) composed of amphiphilic glycerol monooleate and nitroxide lipids [33,34]. However, the mean particle sizes are much larger than those (10–100 nm) of MRI contrast agents that have been optimized for intravenous injection and have the most-prolonged blood circulation time [22]. In this context, branched-bottlebrush copolymer nanoparticles with hydrodynamic diameters of 13–24 nm and large polypropylenimine scaffolded dendrimer molecules, both of which contain spirocyclohexyl nitroxide polyradicals, were reported to show excellent stability towards biological reducing agents and substantial *in vivo* MRI contrast [35,36] (Figure 1-8b, c). However, to date these metal-free nanoparticles have not been used as DDS carriers. With these particles in mind, we envisaged that if stable and biocompatible oil-in-water (O/W)

mixed micelles with appropriate particle sizes of 10–100 nm are available, can encapsulate large amounts of low molecular weight nitroxide radical molecules, and show high resistance to bioreduction, then these radical nanoparticles could be used as proton longitudinal relaxation time (T_1) enhancing MRI contrast agents and EPR imaging probes *in vivo*. Furthermore, if hydrophobic drugs are incorporated into the same magnetic mixed micelles, they are likely to be employed as drug carriers for MRI-visible targeted DDS *in vivo*.

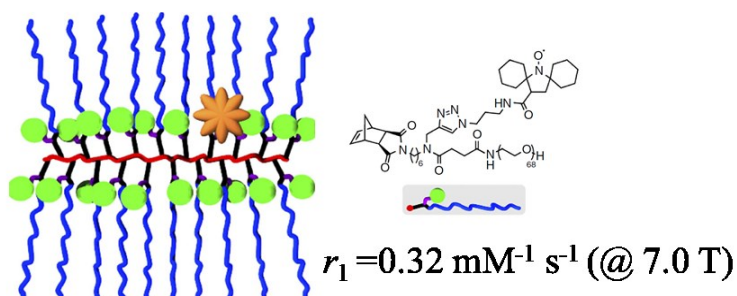
(a)

Core-shell type nanoparticle as EPR probes



(b)

Branched-bottlebrush polymeric MRI contrast agents



(c)

Dendrimeric MRI contrast agents

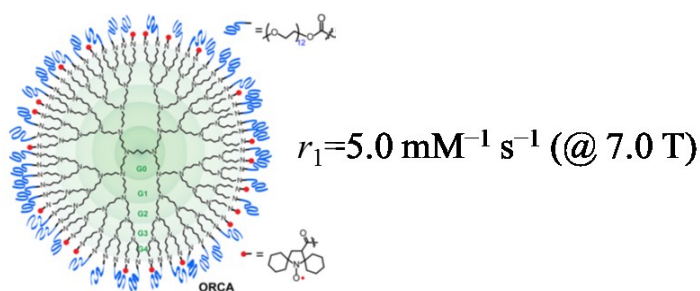


Figure 1-8. Structures of nitroxide-based (a) core-shell type nanoparticle, (b) branched-bottle brush polymeric nanoparticle and (c) dendrimeric nanoparticle. Reprinted with permission from ref. 32, 35 and 36.

1-4. Aim of this study

In this thesis, the present author (Kota Nagura) describes the preparation, characterization and theranostic application of a series of paramagnetic all-organic mixed micelles comprised of non-ionic surfactant and nitroxide radicals prepared according to a facile experimental protocol which the same author found. The stability of the magnetic mixed micelles was found to depend on the length of the alkyl chains in both of the nitroxide radicals and surfactants. Aiming at application, the stability, cytotoxicity and MRI contrast ability of these magnetic mixed micelles were investigated; the magnetic mixed micelles exhibited no cytotoxicity, high resistance towards reduction by ascorbic acid, and sufficient MRI enhancement. In addition, hydrophobic fluorophores and an anticancer drug could be stably encapsulated in the mixed micelles. The magnetic mixed micelles presented here are promising theranostic agents in nanomedicine due to their high biocompatibility, high resistivity towards reduction, and excellent functions such as a drug carrier in therapy and an MR or FL imaging probe in diagnosis.

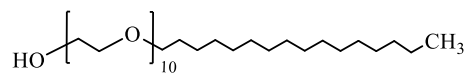
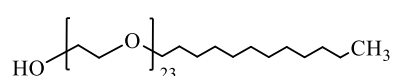
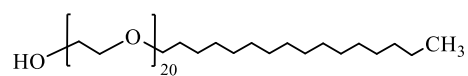
2-1. Introduction

Recently, nano-systems such as nanoparticles has attracted a tremendous interest from scientists; the proper drug for proper person should be administered at the proper time using theranostics [37]. Li et al. stated that ‘the term theranostic was used to describe a fusion of diagnostic and therapeutic strategies with the rationale of increased safety and efficacy in a more personalized form’ [38]. After the injection of nanoparticles into blood circulation, they are immediately subjected to the opsonization. After this process, phagocytosis occurs to remove foreign materials from the bloodstream. To solve these problems, scientists developed PEG-coated nanoparticles with neutral charge which enables to prolong the blood circulation of the nanoparticles due to the protective effect of the hydrophilic PEG chains against opsonins [39,40]. This prolonged circulation time makes PEG-coated micelles a nanomaterial that can serve as an effective theranostic agent.

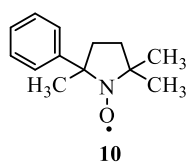
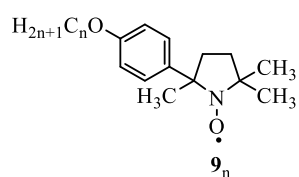
In this work, with a view to developing a theranostic nanomedicine for magnetic resonance (MR) imaging-visible targeted drug delivery system, the author here reports the preparation and characterization of metal-free magnetic mixed micelles (the term ‘nanoemulsions’ was used in our paper [41]) consisting of PEGylated non-ionic surfactants Brij 58 (**6**), Brij 35 (**7**) or Brij 10 (**8**) [42,43,44] and the hydrophobic low-molecular-weight pyrrolidin-*N*-oxyl radicals **9** or **10** have been prepared in pH 7.4 phosphate-buffered saline (PBS) (Figure 2-1).

The structure of the mixed micelles has been characterized by electron paramagnetic resonance (EPR) spectroscopy, and dynamic light scattering (DLS) and small angle neutron scattering (SANS) measurements. The mixed micelles showed high colloidal stability, low cytotoxicity, enough reduction resistance to excess ascorbic acid, and sufficient contrast enhancement in the proton longitudinal relaxation time (T_1)-weighted MR images in PBS *in vitro* and preliminarily *in vivo*. Furthermore, additional hydrophobic fluorescent (FL) dyes **11** or **12** and drugs **13**, **14** or **15**, were simultaneously encapsulated inside the mixed micelles.

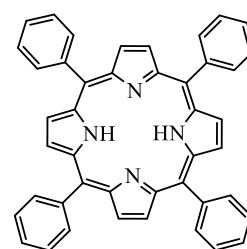
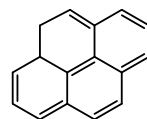
Non-ionic surfactants



Nitroxide radicals



Fluorophores



Drugs

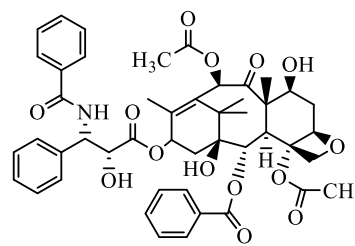
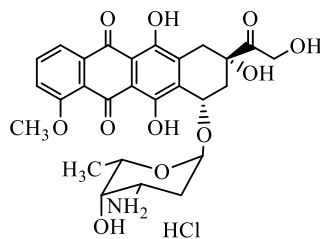
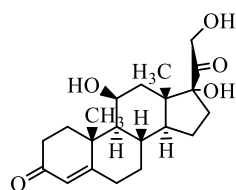


Figure 2-1. (a) Molecular structures used in this chapter: non-ionic surfactant (**6**, **7** and **8**), nitroxide radicals (**9_n** and **10**), fluorophores (**11** and **12**), drugs (**13**, **14** and **15**).

2-2. Results and discussion

2-2-1. Preparation and colloidal stability of magnetic mixed micelles

Referring to the smectic liquid crystalline (LC) layer structure stabilized by interdigitated long alkyl chains (Figure 2-2), together with intermolecular CH/ π and/or CH/O interactions (Figure 1-6), the best combination of a non-ionic surfactant **6**, **7** or **8** bearing a terminal C12 or C16 alkyl chain and nitroxide **9_n** ($n = 14, 16, 18$ and 20) or **10** (no alkyl chain) was searched to obtain most stable mixed micelles with a mean particle size of less than 100 nm.

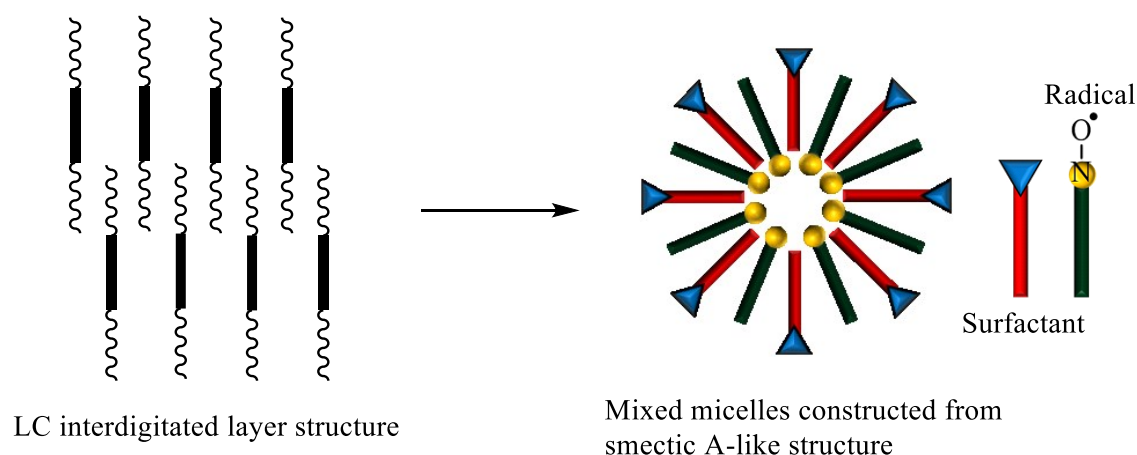


Figure 2-2. Expected interdigitated layer structure in the mixed micelle consisting of equimolar amounts of a non-ionic surfactant and the nitroxide radicals.

The mixed micelles composed of **6** and **9_n**, **7** and **9_n**, **8** and **9_n**, and **6** and **10**, designated as **6/9_n**, **7/9_n**, **8/9_n** and **6/10**, respectively, were prepared at concentration of 10 mM for the surfactant (**6** – **10**) in PBS according to a simple procedure as described in the experimental section. The resulting mixed micelle **6/9₁₈**, as an example, showed a beautiful Tyndall scattering upon irradiation of a visible laser light (Figure 2-3a).

The mean diameter of **6/9_n** or **6/10** in PBS were evaluated by DLS measurement (Figure 2-3c, Table 2-1 and Figure 2-4). The **6/9₁₈** and **6/9₂₀** showed outstanding stability; these mean particle sizes of 17 nm (in the range of 9–36 nm) and 18 nm (in the range of 8–30 nm) in PBS, respectively, were constant for more than one month at 12 °C. In contrast, the pure micelle (10 mM) of **6** in PBS, designated as **P2**, was unstable to give a white precipitate within 2 days at 12 °C. The mean diameter (17 nm) of **6/9₁₈** was supported by small angle neutron scattering (SANS) measurement in D₂O; the SANS profile observed at iMATERIA (BL20, J-PARC) was in good agreement with the scattering function for spherical particles and the particle radius was estimated to be 6.0 ± 2.0 nm (Figure 2-5). In contrast, **6/9₁₄** and **6/9₁₆** became a white suspension after 6 or 10 days, respectively.

Considering the mean diameter (9 nm) of **P6** and the molecular length (3.3 nm) of **9₁₈** estimated

by the Molecular Mechanics using MM2 force field, the mean diameter (17 nm) for **6/9**₁₈ indicates that both the flexible interdigitated layer structure of long alkyl chains and the CH/ π and/or CH/O interactions between neighboring cyclic nitroxide radical moieties should greatly contribute to the remarkable stability of the mixed micelles (Figure 2-2). Furthermore, **6/9**₁₈ and **6/9**₂₀ were also stable after the 1000 times dilution (to 0.01 mM) with PBS. Thus, **6/9**₁₈ and **6/9**₂₀ turned out to be the best choice for biomedical application. For further experiment, the mixed micelle **6/9**₁₈ in PBS was used.

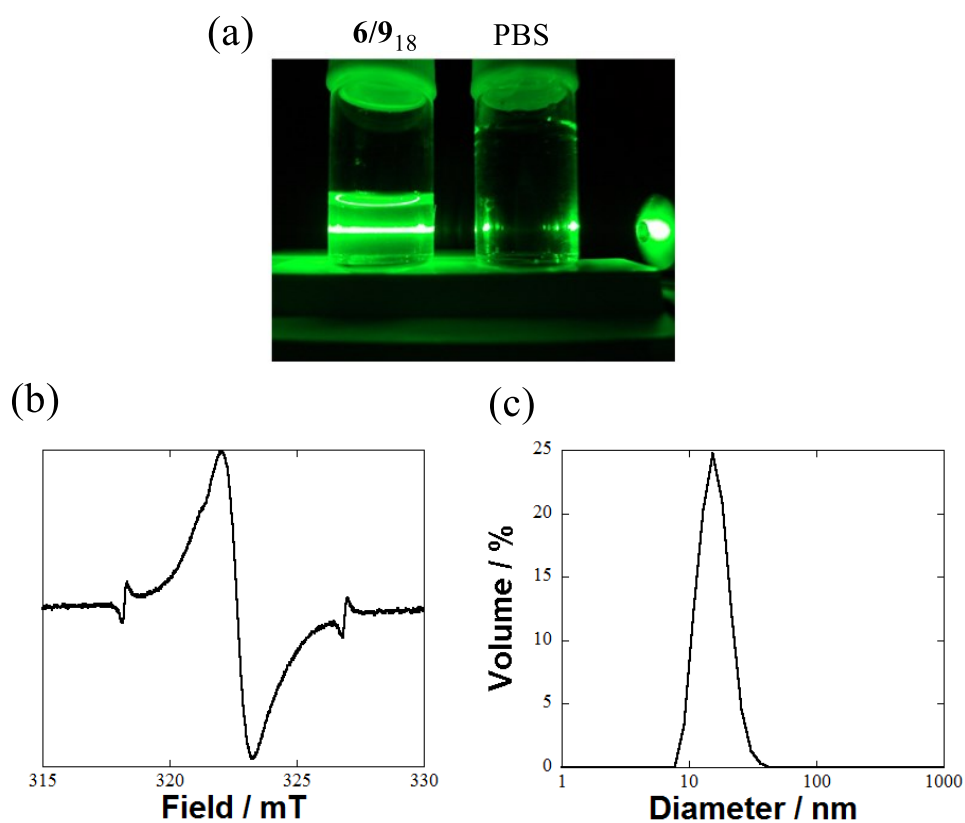


Figure 2-3. Characterization of **6/9**₁₈ in PBS. (a) Tyndall scattering upon irradiation of a green laser light, (b) EPR spectrum of the sample filled in a capillary with the internal standard Mn²⁺ and (c) mean particle size (17 nm) determined by DLS measurement. See the experimental section for details.

Table 2-1. The mean diameters of **6/9**_n in PBS after 2 days from preparation at 25 °C.

Mixed micelle	6/9 ₁₄	6/9 ₁₆	6/9 ₁₈	6/9 ₂₀
Diameter (nm) by DLS	55	26	17	18

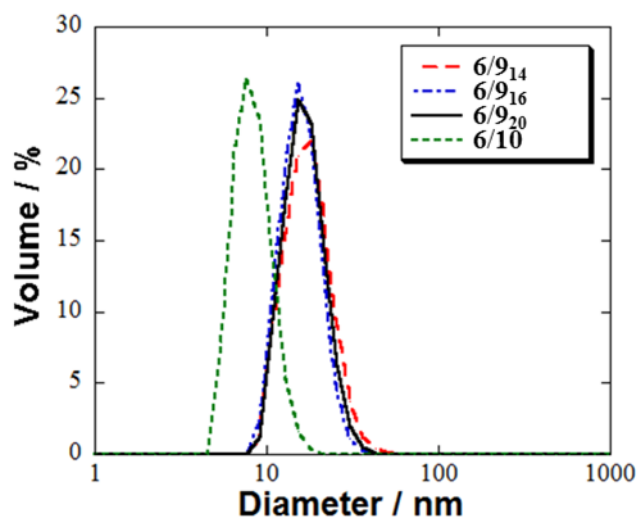


Figure 2-4. Mean diameters of mixed micelles $6/9_n$ ($n = 14, 16$ and 20) and $6/10$ determined by DLS measurement just after preparation (red dashed line: $6/9_{14}$, blue dashed and dotted line: $6/9_{16}$, black solid line: $6/9_{20}$, green dotted line: $6/10$) at $25\text{ }^\circ\text{C}$ in PBS.

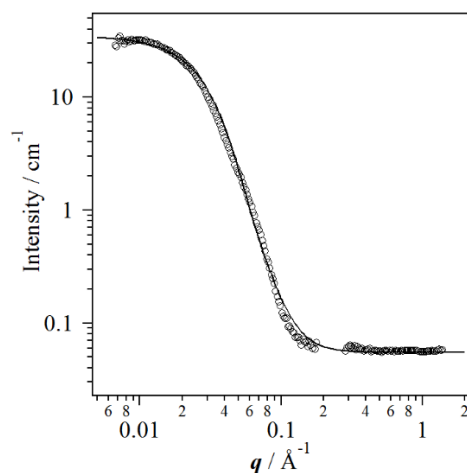
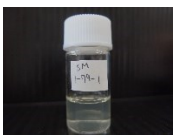
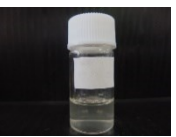
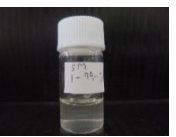
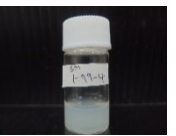
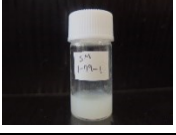
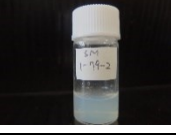

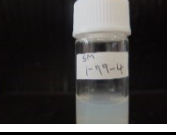


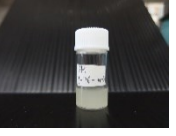
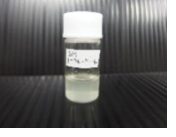

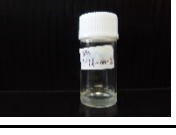
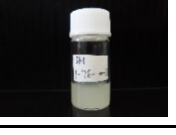
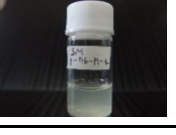


Figure 2-5. SANS profile of $6/9_{18}$ in D_2O . The open circles were experimentally obtained. The solid line indicates the calculated profile assuming spherical particles with radius $R = 6.0 \pm 2.0$ nm. See experimental section for details.

Meanwhile, the micelles $7/9_n$ or $8/9_n$ with a molar ratio of 1 : 1 in MilliQ water was unstable to give a white dispersion after 24 h from preparation, due most likely to the too short polyethylene glycol or alkyl chain length of the surfactants, respectively (Table 2-2). Although $8/9_{14}$ was clear dispersion after 1 day, it became a white suspension within 2 days from preparation.

Table 2-2. Mean diameters and colloidal stability of the mixed micelles $7/9_n$ or $8/9_n$ ($n = 12, 14, 16$ and 18) in MilliQ at 30°C .

		9_{12}	9_{14}	9_{16}	9_{18}
7	Diameter by DLS	33 nm ^a	25 nm ^a	47 nm ^a	152 nm ^a
	Colloidal stability	dispersion ^a 	dispersion ^a 	dispersion ^a 	dispersion ^a 
		→ precipitates ^b 	→ precipitates ^b 	→ precipitates ^b 	→ precipitates ^b 
8	Diameter by DLS	25 nm ^a	26 nm ^a	21 nm ^a	17 nm ^a
	Colloidal stability	dispersion ^a 	dispersion ^a 	dispersion ^a 	dispersion ^a 
		→ precipitates ^c 	→ dispersion ^b 	→ precipitates ^b 	→ precipitates ^b 

^aImmediately after preparation. ^bAfter 24 h from preparation.

From these results, the order of the stability in the mixed micelles $6/9_n$, $7/9_n$ and $8/9_n$ is concluded to be $6/9_{18} \approx 6/9_{20} > 6/9_{16} > 6/9_{14} > 8/9_{14} > 7/9_n$ ($n = 12$ to 18) $\approx 8/9_n$ ($n = 12, 16$ and 18).

In addition, EPR spectroscopy was used to study the dynamics and structural topology of the colloidal systems. EPR technique, a powerful tool for investigating dynamic phenomena of colloidal systems [45], was allowed to give directly magnetic interactions between nitroxide radicals. In general, if a three-line spectrum is observed, there are monomeric nitroxide molecules in PBS (Figure 2-6a). On the other hand, if a broad singlet EPR signal is observed in the studied system, nitroxides are most likely to form a self-assembling structure through magnetic interactions, called Heisenberg spin exchange interaction, between nitroxide radicals (Figure 2-6b) [46,47].

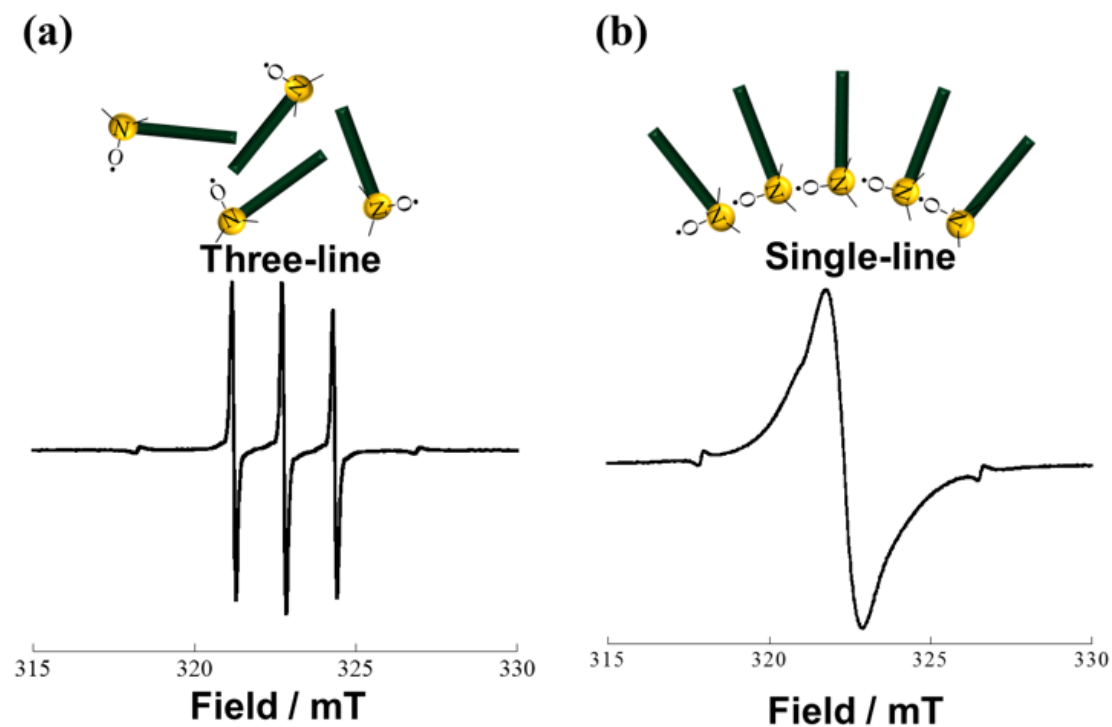


Figure 2-6. Representative EPR spectra of (a) monomeric or (b) self-assembled nitroxide radicals.

The EPR signals of **6/9_n**, **7/9_n** and **8/9_n** consist mainly of broad singlet due to the self-assembly of nitroxide radical molecules within the mixed micelles (Figure 2-3b and 2-7a-c). In contrast, the mixed spectrum of a major three-line shape due to the free nitroxide radical molecules and the minor broad singlet signal arising from molecular aggregation was observed for **6/10** because fairly water-soluble **10** leaked from the mixed micelles (Figure 2-7d).

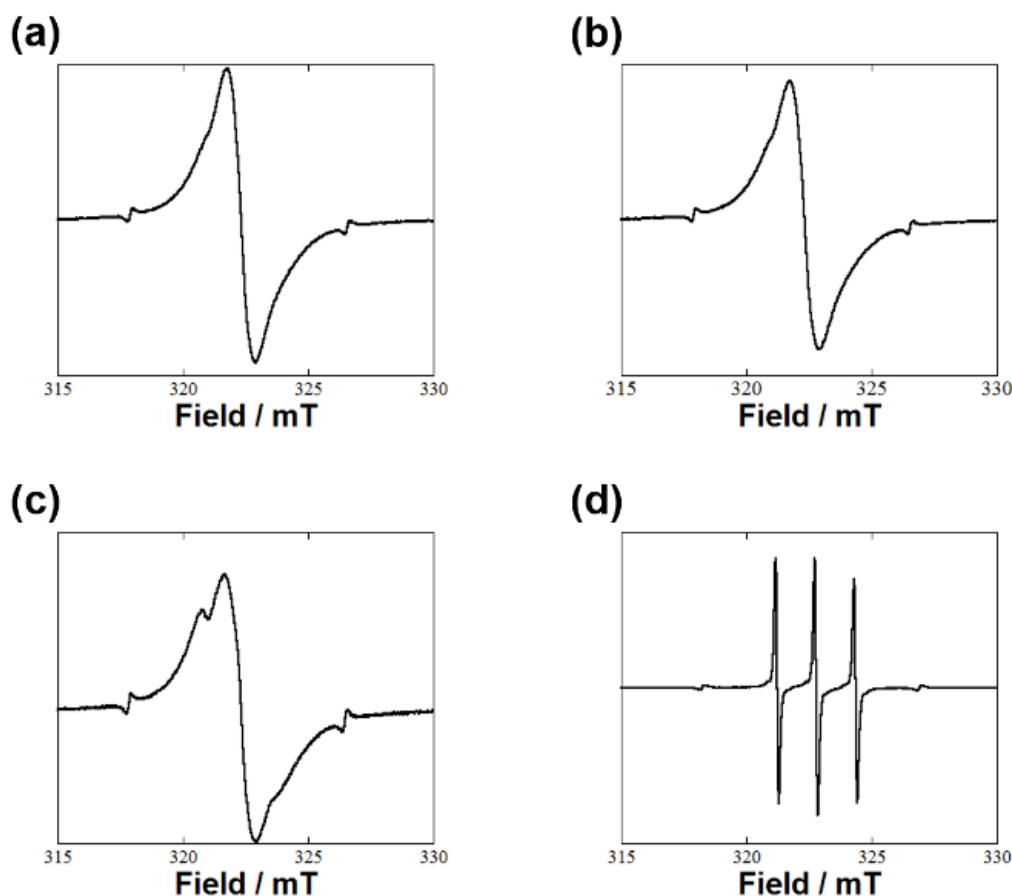


Figure 2-7. EPR spectra of the mixed micelles just after preparation in PBS at 25 °C with the internal standard Mn^{2+} . (a) **6/9**₁₄, (b) **6/9**₁₆, (c) **6/9**₂₀, and (d) **6/10**.

2-2-2. Reduction resistance to ascorbic acid

It is well known that water-soluble nitroxide radicals are readily reduced by antioxidants such as ascorbic acid (VC) and glutathione (GSH) *in vivo* to give the corresponding hydroxylamines [30,31,32]. Therefore, the reduction resistance of **6/9**₁₈ (each final concentration: 10 mM) was evaluated in the presence of excess VC (final concentration: 17.5 mM) in PBS at 25 °C and compared with the experimental results using the same concentration of water-soluble 4-hydroxy-2,2,6,6-tetramethylpiperidine-*N*-oxyl (TEMPOL) [30,31,32]. The decay of the spectral intensity for **9**₁₈ in response to VC was monitored by EPR spectroscopy (Figure 2-8). **6/9**₁₈ showed increased reduction resistance (half-life: 40 min) compared with TEMPOL (half-life: < 1 min); in fact we could not track the decay of EPR spectral intensity for TEMPOL due to the too fast reduction with VC. These results indicate that the nitroxyl groups are shielded by surfactant **6**, but slow water exchange occurs between the inner and outer spheres of **6/9**₁₈ most likely because of the polar circumstances in the central pore surrounded by nitroxyl groups.

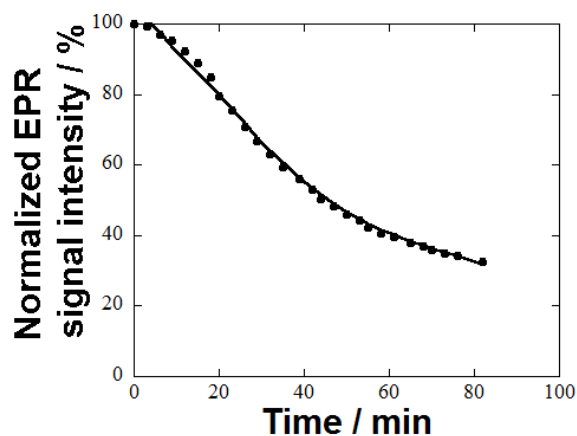


Figure 2-8. Resistance of 9_{18} in $6/9_{18}$ to VC reduction. The reduction in the spectral intensity in PBS was monitored by EPR spectroscopy at 25 °C by using a double integration method. See the experimental section for details.

2-2-3. DDS carrier ability

To evaluate the ability as a DDS carrier, the micelles of $6/9_{18}$ including a fluorophore (**11** or **12**) or a drug (**13**, **14** or **15**), designated as $6/9_{18}/X$ ($X = 11 - 15$), were prepared by adding **11** (10 mol%), **12** (1.0 mol%), **13** (1.0 mol%), **14** (10 mol%) or **15** (10 mol%) upon the preparation of $6/9_{18}$. The mean diameters of $6/9_{18}/11$ was 17 nm, while that of non-magnetic mixed micelle $6/11$ was 9.4 nm (Figure 2-9); these mean diameters were comparable to those of $6/9_{18}$ (17 nm) and **P6** (9 nm) in the absence of **11**. The incorporation of **11** into $6/9_{18}/11$ was confirmed by EPR, UV, and fluorescence spectroscopies; the fluorescence emission from **11** within $6/9_{18}/11$ was considerably quenched by the surrounding nitroxyl groups [35] and revived by adding a large excess (20 equiv based on the nitroxide molecules) of VC (Figure 2-10). These results support the interdigitated layer structure between alkyl chains of **6** and 9_{18} (Figure 2-2) in which molecules of **11** were intercalated.

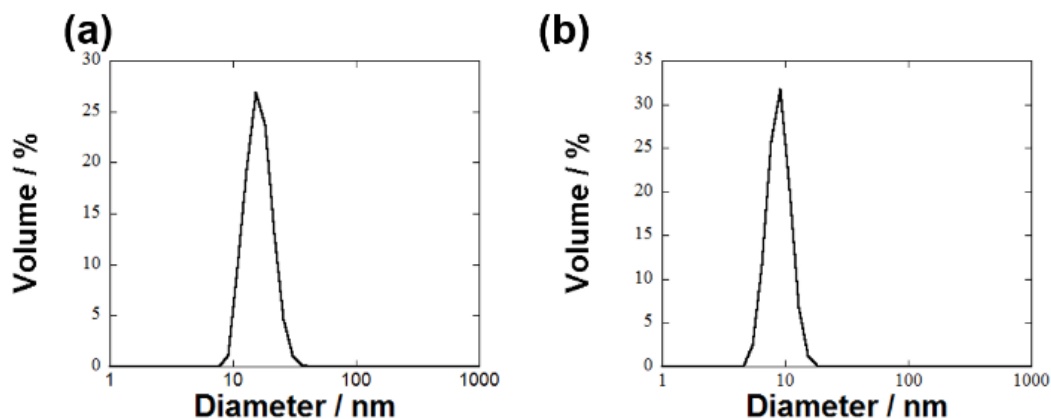


Figure 2-9. Determination of mean diameters of (a) **6/9₁₈/11** (17 nm) and (b) **6/11** (9.4 nm) by DLS measurement in PBS just after preparation.

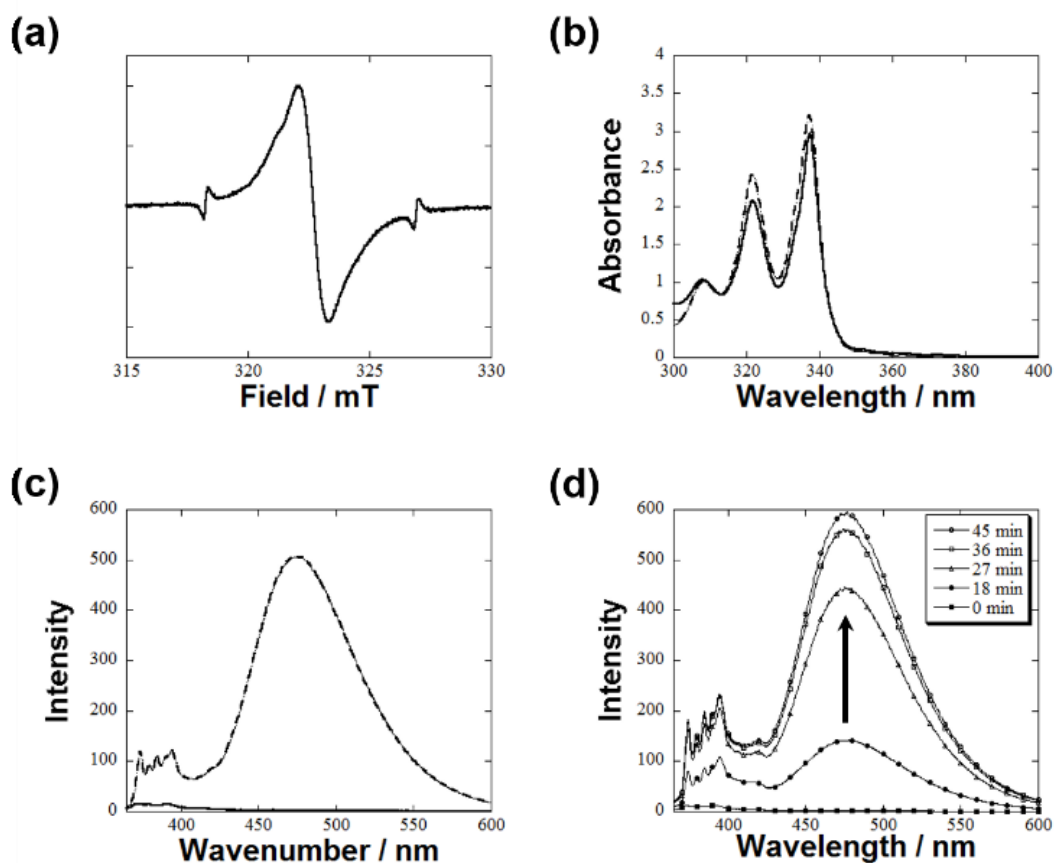


Figure 2-10. EPR, UV, and fluorescence spectra of **6/9₁₈/11** in PBS. (a) EPR spectrum of **6/9₁₈/11** with the internal standard Mn^{2+} , (b) UV spectra of **6/9₁₈/11** (solid line) and **6/11** (broken line), (c) fluorescent spectra of **6/9₁₈/11** and **6/11** (broken line), and (d) fluorescence spectral change from **11** in **6/9₁₈/11** after addition of 20 equiv of VC. See the experimental section for details.

Although **14** leaked from the mixed micelle **6/9₁₈/14** due to the hydrophilicity **14**, compounds **12**, **13** and **15** were successfully incorporated into the corresponding mixed micelles (**6/9₁₈/12**, **6/9₁₈/13** and **6/9₁₈/15**). The mean diameter of **6/9₁₈/15** was 12 nm by DLS measurement, while that of **6/9₁₈/12** or **6/9₁₈/13** was 16 nm (Figure 2-11d-f). Furthermore, the EPR spectrum of **6/9₁₈/15** was a broad three-line shape, whereas **6/9₁₈/12** or **6/9₁₈/13** showed a broad singlet signal (Figure 2-11a-c). It was noticeable that the former exhibited the spectrum of a dispersed nitroxide radical in solution in contrast to the latter ones of self-assembled radicals. These results suggest that the bulky **15** bearing hydrogen-bond donating NH and OH groups should interact with neighboring nitroxyl groups by hydrogen bond to form a quasi-solution, resulting in a considerably slow rotation of the nitroxyl groups, both of which are advantageous to enlarge the MRI contrast ability. In contrast, the mixed micelle incorporating **12** or **13** with a fairly planar molecular structure would take an intercalated molecular assembly in the interdigitated layer, similar to the case of **6/9₁₈/11**.

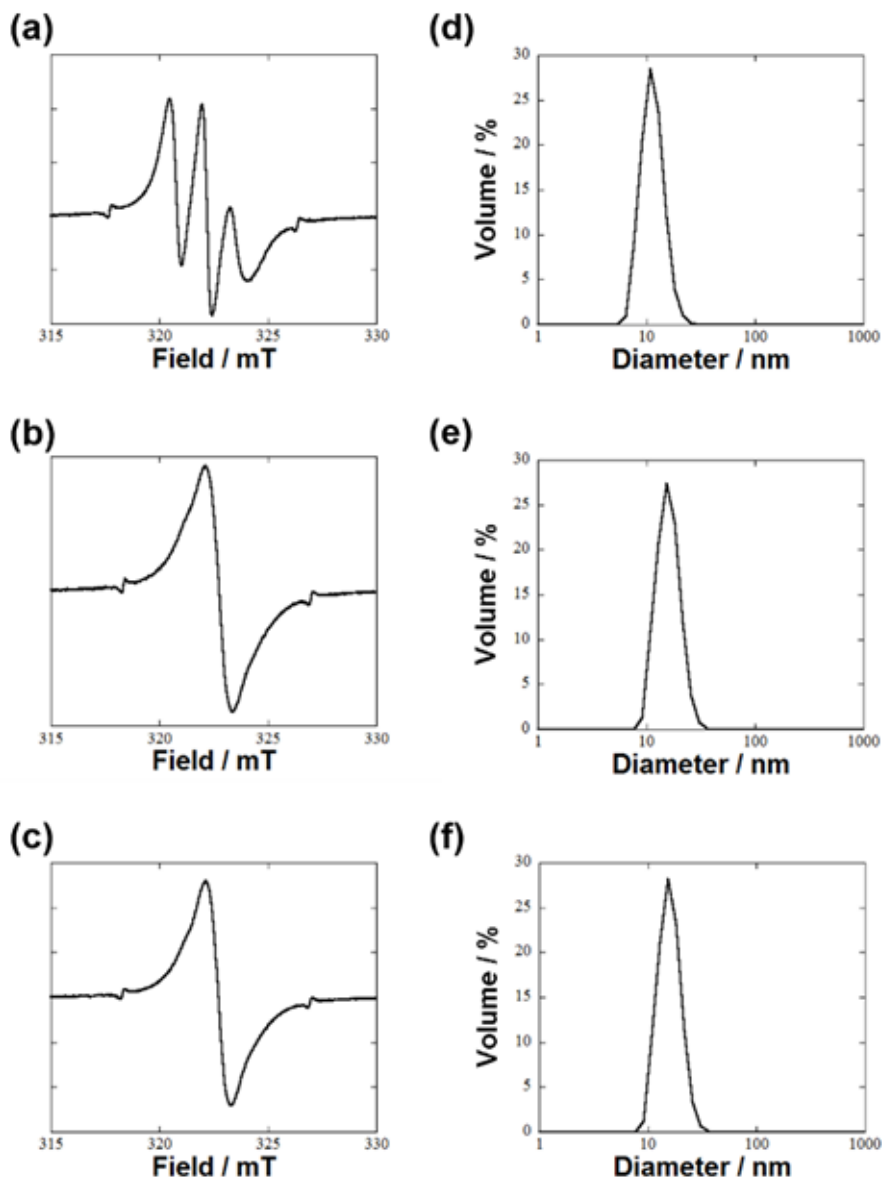


Figure 2-11. (a-c) EPR spectra with the internal standard Mn^{2+} and (d-f) mean particle sizes determined by DLS measurement immediately after preparation of (a, d) **6/9₁₈/15**, (b, e) **6/9₁₈/12**, and (c, f) **6/9₁₈/13** in PBS.

2-2-4. *In vitro* cytotoxicity

To verify the uptake of the magnetic mixed micelles into cancer cells, the cancer cell viability of **6/9₁₈** was assessed and compared with that of **P6** by the CCK-8 assay at the initial concentrations of 2.5 mM for **6** and **9₁₈** (Figure 2-12a). Consequently, both **P6** and **6/9₁₈** showed high toxicity at the concentrations of 0.625 mM or higher, while they exhibited much lower or little toxicity at the concentration of 0.313 mM or lower. In contrast, both **6/9₁₈/15** and free **15** displayed significant

toxicity against HeLa cells at the concentration of 0.16 μM or higher of **15**. Thus, the fact that the drug **15** released from the mixed micelles is pharmaceutically active suggests that **6/9₁₈/15** were incorporated into the cancer cells and are useful as a DDS drug carrier.

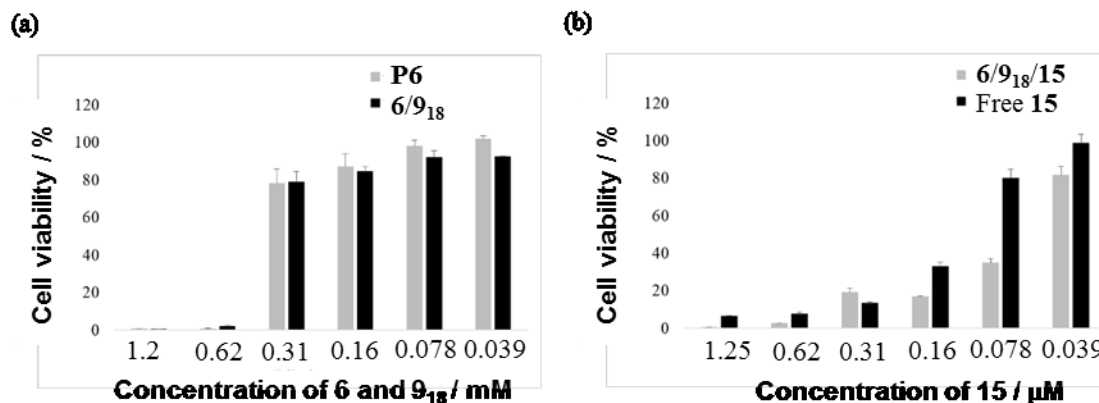


Figure 2-12. Comparison of the *in vitro* cytotoxicity between (a) P6 and 6/9₁₈, and (b) 6/9₁₈/15 and free 15 by using HeLa cells. The cell viability was assayed by using the CCK-8 kit after incubation for 24 h at 37 °C under 5% CO₂. See the experimental section for details.

2-2-5. MRI measurement

The water proton relaxivity of 6/9₁₈ (1.2 – 10 mM) was determined from relaxation time (T_1) as a function of concentration at 25 °C at 4.7 T (Figure 2-13a, A – D). 6/9₁₈ at a concentration of 10 mM significantly brightened the T_1 -weighted MR phantom images compared with PBS alone (Figure 2-13a, L). Furthermore, we observed the bright MR phantom images of 6/9₁₈/11, 6/9₁₈/12, 6/9₁₈/13 and 6/9₁₈/15 (Figure 2-13a, I, J, E and K). Particularly, 6/9₁₈/15 exhibited the brightest contrast among them including 6/9₁₈ (Figure 2-13a, E). This is likely associated with the decrease in the mean particle size (12 nm) and the unique EPR spectrum as described in the previous section, which allows relatively fast water exchange between the inner and outer spheres of the mixed micelles and the increase in rotational correlation constant of nitroxyl groups [33,34].

To evaluate the relaxation rate enhancement by the nitroxide-based magnetic mixed micelles, the longitudinal relaxation rate (r_1) was determined from the relaxation times as a function of concentration by using spin-echo method at 4.7 T with respect to 6/9₁₈ and 6/9₁₈/15; linear regression analysis yielded the r_1 of 0.12 and 0.16 $\text{mM}^{-1}\text{s}^{-1}$, respectively (Figure 2-13b, c). These r_1 values were less than that (4.0 $\text{mM}^{-1}\text{s}^{-1}$ at 4.7 T) of Magnevist [one of Gd(III) complex agents] in deionized water, but comparable or larger than those (in the order of 0.1 $\text{mM}^{-1}\text{s}^{-1}$ at 4.7 T) for ordinary water-soluble small mononitroxide molecules [48]. However, the fact that there is a good linear relation between the T_1 contrast enhancement and the concentration of nitroxyl groups would increase the significance of our mixed micelles for biomedical application [49]. Furthermore, it is a big advantage that nitroxide radicals can act as T_1 -enhancing MRI contrast agents with much lower toxicity in comparison with the

commonly used molecular Gd(III) complex agents [50,51,52,53].

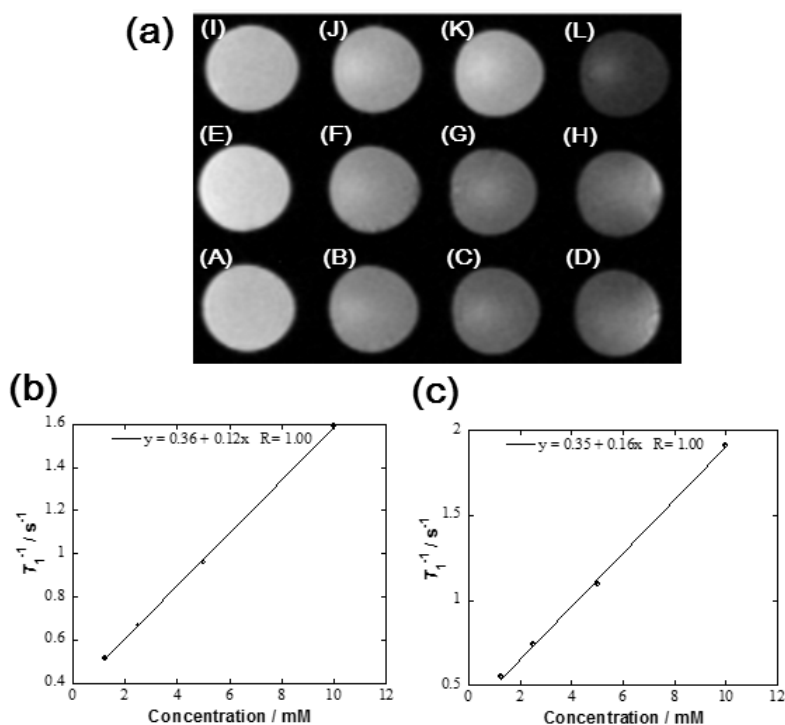


Figure 2-13. T_1 -weighted MR phantom images (4.7 T, 25 °C) of (a) (A–D) $6/9_{18}$ and (E–H) $6/9_{18}/15$, at 10, 5.0, 2.5 and 1.2 mM in PBS, and (I) $6/9_{18}/11$, (J) $6/9_{18}/12$ and (K) $6/9_{18}/13$ (10 mM each). The control image of PBS alone is shown in panel (L). Plots of T_1^{-1} vs the concentration of 9_{18} in (b) $6/9_{18}$ and (c) $6/9_{18}/15$; the r_1 values were determined to be 0.12 and 0.16 $\text{mM}^{-1}\text{s}^{-1}$, respectively. See the experimental section for details.

Finally, to examine whether $6/9_{18}$ can actually serve as an *in vivo* MRI contrast agent, a preliminary MRI experiment was performed using living mouse brain tissues. Three hundred microliter (μL) of $6/9_{18}$ (10 mM each) in PBS were intravenously injected into an anesthetized mouse (weight around 30 g) lying supinely in an animal holder. Subsequently, the cradle was inserted into the MRI machine (7.0 T) to acquire T_1 -weighted MR images by the spin-echo method. Since it was anticipated that the injected mixed micelles would be transported by the blood stream and accumulated to the pituitary gland in the brain, T_1 weighted MR images of the pituitary gland were taken after the injection of $6/9_{18}$. As a result, a distinct MRI contrast enhancement was observed in the pituitary gland after injection with high reproducibility (Figure 2-14). This result demonstrates that $6/9_{18}$ serves as an *in vivo* T_1 -weighted MRI contrast agent.

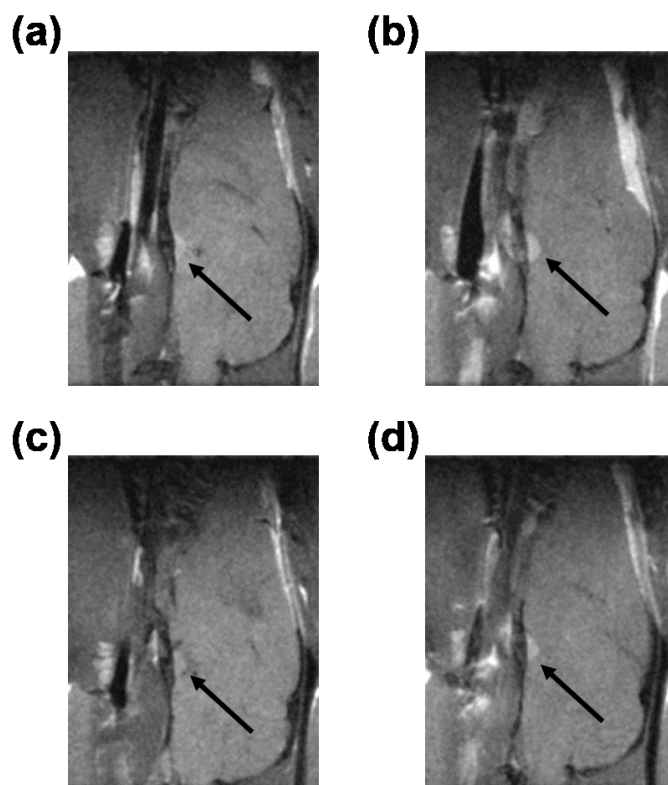


Figure 2-14. T_1 -weighted MR images of brain tissues of two mice: (a, c) before and (b, d) 13 min after the intravenous injection of 300 μL of $\mathbf{6/9}_{18}$ (10 mM each) in PBS. The images in (a) and (b) correspond to one mouse, and those in (c) and (d) refer to the other mouse. Distinct contrast enhancement was observed in the pituitary glands of both mice (indicated by black arrows). See the experimental section for details.

2-3. Conclusions

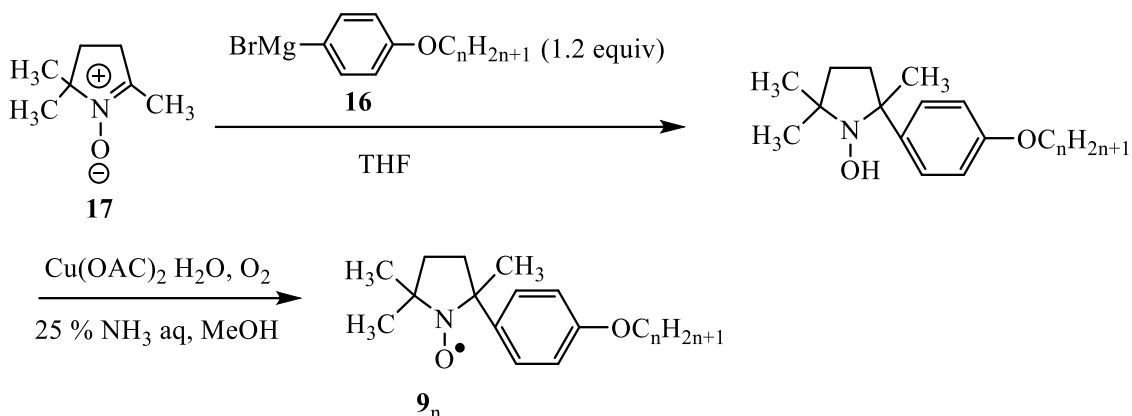
We have successfully prepared the ideal and robust, metal-free magnetic mixed micelles with a desired mean diameter (< 100 nm). The colloidal stability was found to depend on the alkyl chain length in both of surfactant and nitroxide radical. The mixed micelle **6/9**₁₈ exhibited high reduction resistance to ascorbic acid and sufficiently bright contrast in the proton T_1 -weighted MR images *in vitro* and preliminarily *in vivo*, and incorporated as much as 10 mol % of hydrophobic drugs or quasi-drugs into the nanoparticles. From the cell viability assay, it has been concluded that the magnetic mixed micelles show low toxicity at the concentrations (0.31 mM or lower) of **6/9**₁₈ and that **6/9**₁₈/**15** effectively suppress the HeLa cell growth at the concentrations of 0.078 μ M or higher of **15**. Thus, it is highly expected that our magnetic mixed micelles will serve as a theranostic nanomedicine for MRI-visible targeted drug delivery system *in vivo*, if they have an additional function to be selectively incorporated and accumulated into the targeted cancer cells.

2-4. Experimental section

2-4-1. Materials

The surfactants **6** (Brij 58, Sigma-Aldrich), **7** (Brij 35, Sigma-Aldrich) and **8** (Brij C10, Sigma-Aldrich), pyrene (**11**, Sigma-Aldrich), tetraphenylporphyrin (**12**, kindly gifted by Mr. Yamanaka, Kyoto University), hydrocortisone (**13**, TCI), doxorubicin (**14**, TCI) and paclitaxel (**15**, Sawai Pharmaceutical), were used as received.

2-4-2. Synthesis of nitroxide radical compounds 9_n



Scheme 2-1. Synthesis of 9_n ($n = 14, 16, 18$ and 20)

Synthesis of 4-alkoxy-1-bromobenzene

A mixture of 4-bromophenol (31.69 g, 0.183 mol) and potassium carbonate (0.134 mol) in DMF (168 mL) was stirred at 70 °C for more than 0.5 h. To the suspension was added alkyl bromide (0.184 mol) and the mixture was stirred overnight at 70 °C. Water (300 mL) was added and the mixture was extracted with hexane (3×150 mL). The organic extracts were washed with brine (300 mL), 2N NaOH solution (300 mL) and water (300 mL), dried over MgSO_4 , and evaporated to give 4-alkoxy-1-bromobenzene (more than 60 % yield).

Preparation of Aryl magnesium bromides 16

To magnesium turnings (0.585 g, 24.1 mmol) dried by heating under vacuum were added THF (50 mL), arylbromide (25.9 mmol), and small amount of 1,2-dibromoethane under argon. The reaction mixture was stirred for 3 h to afford a solution of aryl magnesium bromide **16**.

General synthetic procedure for compounds 9_n ($n = 14, 16, 18$, and 20)

To a solution of the nitronium **17** (2.55 g, 20.0 mmol) [54] in THF (15 mL) was slowly added a solution of the freshly prepared Grignard reagent **16** (ca. 24 mmol) in THF under argon at -78 °C. The temperature was raised slowly to 25 °C and stirring was continued overnight. The reaction mixture

was poured into a saturated aqueous NH_4Cl solution (100 mL), and then extracted with dichloromethane (DCM) (2×100 mL). The combined DCM extract was dried over MgSO_4 and the solvent was evaporated. The residual oil ($n = 14$ and 16) was dissolved in methanol (30 mL). For the compounds which possess longer alkyl chain ($n = 18$ and 20), the resulting solid was dissolved in a mixture of DCM (30 mL) and methanol (30 mL). To this solution were added aqueous NH_3 solution (25 wt%, 2.0 mL) and copper (II) acetate monohydrate (0.809 g, 4.05 mmol). Oxygen was bubbled through the solution until a persistent deep blue color was observed. The solvent was then removed under reduced pressure and saturated aqueous NaHCO_3 (100 mL) was added to the solution. The solution was extracted with DCM (2×100 mL) and dried over MgSO_4 , and the solvent removed under reduced pressure. The resulting mixture was purified by column chromatography (hexane/ether = 90/10) on silica gel to afford the compounds $\mathbf{9}_n$ in around 20% yield.

$\mathbf{9}_{14}$: M.p. (DSC) 52.7 °C. EPR (0.10 mM in THF, 25 °C): $g = 2.0067$, $a_N = 1.41$ mT. Anal. Calcd (%): C, 77.83; H, 11.13; N, 3.36. Found (%): C, 77.61; H, 11.01; N, 3.34.

$\mathbf{9}_{16}$: M.p. (DSC) 60.9 °C. EPR (0.10 mM in THF, 25 °C): $g = 2.0066$, $a_N = 1.39$ mT. Anal. Calcd (%): C, 78.32; H, 11.33; N, 3.15. Found (%): C, 78.40; H, 11.34; N, 3.14.

$\mathbf{9}_{18}$: M.p. (DSC) 65.1 °C. EPR (0.10 mM in THF, 25 °C): $g = 2.0066$, $a_N = 1.40$ mT. Anal. Calcd (%): C, 78.76; H, 11.51; N, 2.96. Found (%): C, 78.68; H, 11.79; N, 2.87.

$\mathbf{9}_{20}$: M.p. (DSC) 70.0 °C. EPR (0.10 mM in THF, 25 °C): $g = 2.0066$, $a_N = 1.40$ mT. Anal. Calcd (%): C, 79.14; H, 11.67; N, 2.80. Found (%): C, 78.99; H, 11.67; N, 2.80.

2-4-3. Preparation of magnetic mixed micelles in PBS

2-4-3-1. $\mathbf{6/9}_n$, $\mathbf{6/10}$, $\mathbf{7/9}_n$ and $\mathbf{8/9}_n$

As a typical example, $\mathbf{6/9}_{18}$ (final concentration 10 mM each) were prepared in PBS as follows. In a 4 mL glass vial, 22.48 mg (20 μmol) of **6** was dissolved in PBS (2mL). Then 9.46 mg (20 μmol) of $\mathbf{9}_{18}$ dissolved in very small amount of ether was added to the vial. The mixture was subjected to sonication (Branson Model 2510, power 125 W, frequency 42 kHz) for 3 min at 25 °C to give a white suspension. Finally, the suspension was heated for more than 10 min at 90 °C using a water bath to form ether-free transparent $\mathbf{6/9}_{18}$ (10 mM each), which were passed through a 0.45 μm membrane filter.

2-4-3-2. $\mathbf{6/9}_{18/11}$, $\mathbf{6/9}_{18/12}$, $\mathbf{6/9}_{18/13}$ and $\mathbf{6/9}_{18/14}$

As a typical example, $\mathbf{6/9}_{18/11}$ were prepared in PBS as follows. To 22.48 mg (20 μmol) of **6** dissolved in PBS (2 mL) in a 4 mL glass vial, was added 9.46 mg (20 μmol) of $\mathbf{9}_{18}$ and 0.40 mg of **11** (2.0 μmol)

dissolved in very small amount of an appropriate organic solvent (ether for **11**, or DCM for **12** and **13**). The mixture was subjected to sonication to give a white suspension. Finally, the suspension was heated for more than 10 min at 90 °C using a water bath to form the solvent-free transparent **6/9**₁₈/**11**, **6/9**₁₈/**12**, **6/9**₁₈/**13** and **6/9**₁₈/**14**, which were passed through a 0.45 μm membrane filter.

2-4-3-3. 6/9₁₈/**15**

To a 4 mL glass vial was added 283 μL (1.7 mg, 2.0 μmol) or 2.8 μL (16.8 μg, 19.7 nmol), for MRI measurement or *in vitro* cytotoxicity experiment, respectively, of paclitaxel (**15**) formulation including polyoxyethylene castor oil and ethanol, and the ethanol was removed under vacuum. Then, 9.46 mg (20 μmol) of **9**₁₈ dissolved in very small amount of ether were added to the vial. To this vial was added 22.48 mg (20 μmol) of **6** dissolved in PBS (2 mL) and the mixture was subjected to sonication to give a white suspension. Finally, the suspension was heated for more than 10 min at 90 °C using a water bath to form the ether-free transparent **6/9**₁₈/**15**, which were passed through a 0.45 μm membrane filter.

2-4-4. DLS measurement (Table 2-1, and Figures 2-3c, 2-4, 2-9 and 2-11d-f)

The mean particle size of the mixed micelles was measured at 25 °C using a UPA-UT151 instrument (MicrotrackBEL). After the samples were passed through a 0.45 μm φ disposable membrane filter, the particle size was measured in PBS using an attached cuvette. The mean diameter was calculated on volume and number weighted averages from five measurements for each sample. Only volume average size distributions are shown in the Figures of this chapter.

2-4-5. EPR spectroscopy

2-4-5-1. EPR measurement (Figures 2-3b, 2-7, 2-10a and 2-11a-c)

The EPR spectra were recorded in a capillary tube (~1 mm φ) at 25 °C and 0.34 T (X-band, at a fixed frequency with sweeping field centered at 0.34 T) on a JES-PX105 spectrometer (JEOL) with the following parameters: 9.2 GHz of frequency, 25 mT of sweep width, 1.00 mW of microwave power, 0.1 mT of modulation, 0.03 s of time constant, and 6.0 ms of sweep time.

2-4-5-2. Reduction resistance of the mixed micelles to excess ascorbic acid (VC) (Figure 2-8)

To **6/9**₁₈ (10 mM each) in PBS (1.5 mL) was added 4.64 mg (26.3 μmol) of VC. The mixture was transferred to a capillary tube (1 mm φ) immediately, followed by measurement of the EPR spectrum of the solution over time recorded at 25 °C and 0.32 T (X-band, at a fixed frequency with sweeping field centered at 0.32 T) on a JES-RE2X spectrometer (JEOL). The final concentrations of **9**₁₈ in **6/9**₁₈ and VC were 10 mM and 17.5 mM, respectively. The spectra were collected with the following parameters: 9.1 GHz of frequency, 7.5 mT of sweep width, 1.00 mW of microwave power, 0.25 mT of modulation, 0.1 s of time constant, and 2.0 ms of sweep time.

2-4-6. SANS measurement (Figure 2-5)

6/9₁₈ (10 mM each) was prepared in D₂O to induce a strong contrast for SANS experiment. SANS measurements were conducted by use of iMATERIA (BL20) [55] at the Materials and Life Science Experimental Facility (MLF) of the Japan Proton Accelerator Research Complex (J-PARC).

The open circles in Figure 4 indicate the SANS profile obtained after circular-averaging the scattered neutron distribution on the large area detector. The horizontal axis (q) is the magnitude of scattering vector $[(4\pi/\lambda) \sin(\theta/2)$; λ is neutron wavelength and θ is scattering angle]. The SANS profile was converted to the absolute unit (cm^{-1}) by use of the glassy carbon standard provided by Jan Ilavsky [56].

The solid line in Figure 4 indicates the numerically calculated profile, $I(q)$.

$$I(q) = \int W(R) I_{\text{sph}}(q; R) dR + I_{\text{inc}} \dots \dots \dots \text{(Eq. 2-1)}$$

Here, $I_{\text{sph}}(q; R)$ is a scattering function due to spherical particles with radius R , $W(R)$ is radius distribution, and I_{inc} is incoherent scattering term which is q -independent [57].

$$I_{\text{sph}}(q; R) = N\Delta\rho^2(4\pi R^3/3)^2[\sin(qR) - qR \cos(qR)]^2/(qR)^6. \text{ (Eq. 2-2)}$$

N is a number density of spherical particles. $\Delta\rho$ is a neutron scattering length density difference between the mixed micelles and the surrounding solution. As a radius distribution, we used Gaussian distribution.

$$W(R) = (2\pi\Delta R^2)^{-1/2} \exp[-(R-R_{\text{ave}})^2 / (2\Delta R^2)] \dots \dots \dots \text{(Eq. 2-3)}$$

The SANS profile observed for the mixed micelles was in good agreement with the scattering function for spherical particles. As a result, the particle radius was estimated to be 6.0 ± 2.0 nm.

2-4-7. UV and fluorescence spectroscopy (Figures 2-10b– d)

The fluorescent spectra of **11** in **6/9**₁₈/**11** and **6/11** were measured at 25 °C in PBS (2 mL) with the RF-5300PC spectrofluorometer (Shimadzu) using excitations at $\lambda_{\text{ex}}=355$ nm. Band widths of 5 nm for excitation and 1.5 nm for emission were used. After addition of 20 equiv of VC to the cuvette, the emission spectra appeared and increased.

2-4-8. Evaluation method of in vitro cytotoxicity (Figure 2-12)

HeLa cells (9.0×10^3 cells in 100 μL per well) were seeded at in a 96-well tissue culture plate with Dulbecco's modified Eagle's medium (DMEM) containing 10% fetal bovine serum and 1% penicillin/streptomycin and grown for 24 h at 37 °C with 5% CO₂. Then, each well was treated with a PBS solution (10 μL) of **P6**, **6/9**₁₈, **6/9**₁₈/**15**, or free **15**. **6/9**₁₈ at the initial concentration of 1.2 mM and as low as 10 μM of **15** was diluted with PBS up to 0.039 mM before incubation. After incubation for 24 h at 37 °C under 5% CO₂, these compounds shown above were removed and then cell toxicity was assayed using CCK-8 kit according to the manual provided by the kit manufacture (Dojindo Molecular Technologies).

2-4-9. *In vitro* MRI measurement (Figure 2-13)

In vitro T_1 -weighted MRI measurement was conducted by using a 4.7 T machine (Bruker BioSpec 47 USR). **6/9**₁₈ with a molar ratio of 1 : 1 and **6/9**₁₈/**15** with a molar ratio of 1 : 1 : 0.1 at the initial concentration of 10 mM were diluted with PBS up to 1.2 mM before measurement. After these mixed mielles were transferred to plastic tubes, they were fixed in a sample holder. The magnetometric measurements were conducted at 25 °C. MR phantom images were obtained by a RAREVTR sequence [echo time (TE) = 10 ms, repetition time (TR) = 5,000, 3,000, 1,500, 800, 400, and 200 ms, slice thickness = 5.0 mm, field of view = 80×50 mm², flip angle = 90 °]. Region-of-interest (ROI) was set on the tubes and the signal intensities were measured for each concentration. T_1 values were extracted from each sample in the image using ROIs by the image sequence analysis tool in ParaVision 6 and calculated by exponential fitting. The longitudinal relaxation rate (r_1) was calculated with Eq. 2-4:

$$1/T_1 = 1/T_0 + r_1 C \dots\dots\dots \text{(Eq. 2-4)}$$

where T_0 and C are the relaxation time in the absence of the paramagnetic species and the concentration of the paramagnetic species, respectively.

2-4-10. *Animal study* (Figures 2-14 and 2-15)

The protocols for the animal experiments were approved by the Shiga University of Medical Science and were carried out in accordance with the National Institutes of Health Animal Care and Use Protocol (NIH, Bethesda, MD, USA). Male c57BL/6N mice (aged 6 to 7 weeks; body weight, about 25 g) were supplied from Japan SLC Inc. (Shizuoka, Japan) and three mice were used for the MRI experiments. They were housed per cage in climate-controlled, circadian-rhythm-adjusted rooms, and were allowed access to food and water ad libitum. Three hundred microliter (μL) of **6/9**₁₈ (10 mM each) or control **P6** (10 mM) in PBS were intravenously injected into mice under anesthesia with 1.5% isoflurane.

2-4-11. *In vivo* MRI measurement of the mouse brain (Figures 2-14 and 2-15)

In vivo MRI experiment using mouse brain tissues was conducted on a 7 T machine (Varian). T_1 -weighted MR images were collected with the spin-echo multiple slices pulse sequence. Typical imaging parameters for T_1 -weighted images were as follows: echo time (TE) = 13.63 ms; repetition time (TR) = 500 ms; field of view (FOV) = 16 mm×12 mm; data matrix = 256×192; slice thickness = 1.00 mm; average = 8; number of slices = 5.

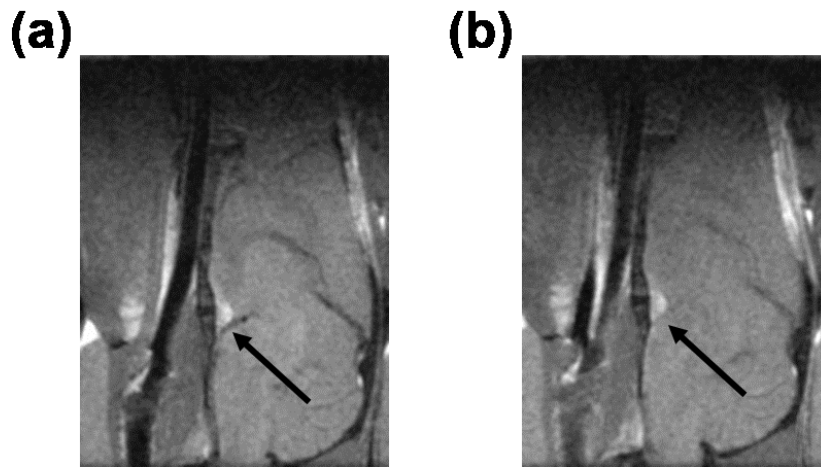


Figure 2-15. T_1 -weighted MR images of brain tissues of the same mouse: (a) before and (b) 13 min after the intravenous injection of 300 μL of **P6** (10 mM) in PBS. Contrast enhancement was not observed in the pituitary gland (indicated by black arrows).

3-1. Introduction

Magnetic resonance imaging (MRI) is one of the most frequently used imaging techniques for clinical medicine, and MRI contrast agents are sometimes required for more accurate diagnosis. Gadolinium (III) (Gd^{3+}) complexes such as Magnevist are widely used as paramagnetic metal ion-based contrast agents in clinic [58,59,60]. However, the patients with impaired kidney function face a risk of a serious adverse reaction termed nephrogenic systemic fibrosis (NSF) by using Gd^{3+} contrast agents [61,62]. Since the first report of this adverse effect on renal dialysis patients, guidelines for the administration of Gd^{3+} contrast agents have been issued and implemented worldwide to minimize the risk of NSF [63, 64]. Since then, metal-free materials including nitroxide radical compounds have been investigated as proton longitudinal relaxation time (T_1) enhancing agents. [65,66,67].

Nitroxide radicals have attracted great interest as a relatively safe spin source for several decades despite the lower contrast ability than Gd^{3+} complex, because the sterically protected N-O group is thermally stable in the air. A polymer-based nanoparticle composed of nitroxide lipids and glycerol monooleate was recently reported by Muir and co-workers as an MRI contrast agent [33]. However, the mean diameters (> 180 nm) were too large to have passive targeting property based on enhanced permeation and retentive effect. Although the spirocyclohexyl nitroxide polyradicals based on branched-bottlebrush copolymers and the polypropylenimine-scaffolded dendrimers were also reported, the functions of these materials were limited to MRI contrast [35,36]; no other functions such as drug carrier nor fluorescence (FL) imaging were endowed.

In this context, we prepared the metal-free magnetic mixed micelles comprised of equimolar amounts of polyoxyethylene (20) cetyl ether (Brij 58, **6**) and (\pm)-2,2,5-trimethyl-5-(4-alkoxyphenyl) pyrrolidine-*N*-oxyl radical (**9_n**) according to a simple experimental protocol [41]. These micelles showed high colloidal stability, high resistance to a reducing agent, and enough contrast enhancement in the T_1 -weighted MRI in PBS *in vitro*. In addition, fluorophores or drugs were stably encapsulated inside the mixed micelles. However, the surfactant **6** exhibited cytotoxicity in $0.16 \mu M$ or higher, while nitroxide radicals such as **9_n** were generally known to show very low toxicity to cells and animals [68,69,70,71]. Therefore, we focused on the surfactant 'Tween series' (**18** and **19**), because they have been employed in clinical medicine owing to their biocompatibility [72,73,74]. Here we report the preparation, stability, structure and theranostic application of the magnetic mixed micelles composed of surfactant Tween 80 (**18**) and nitroxide radical (**9₁₈**) as well as the micelles including fluorophores and a drug.

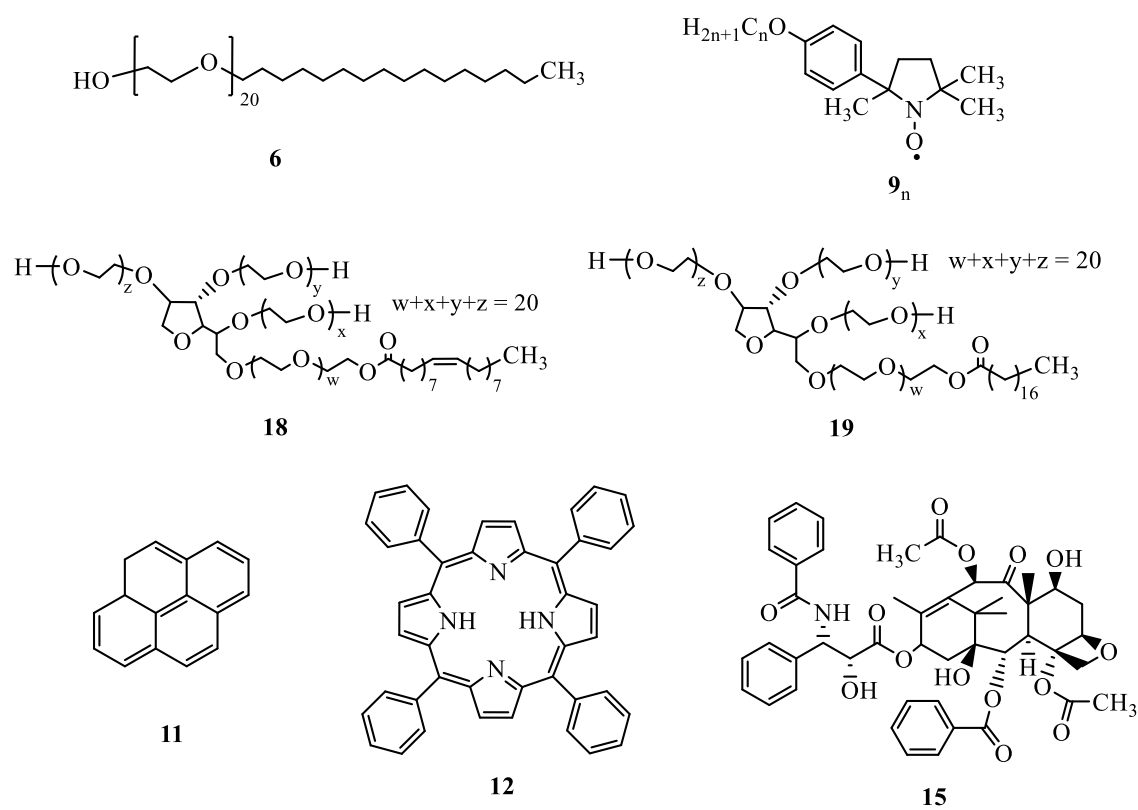


Figure 3-1. Molecular structures of non-ionic surfactant Brij 58 (**6**), nitroxide radicals [**9_n** ($n = 12, 14, 16, 18$ and 20)], Tween 80 (**18**), Tween 60 (**19**), pyrene (**11**), tetraphenylporphyrin (**12**) and paclitaxel (**15**).

3-2. Results and Discussion

3-2-1. Preparation and stability

3-2-1-1. Preparation and stability of magnetic mixed micelles of $18/9_n$ and $19/9_n$

The mixed micelles composed of **18** and 9_n , and **19** and 9_n , designated as $18/9_n$ and $19/9_n$ respectively, were prepared at concentration of 10 mM in phosphate buffer saline (PBS) according to the experimental procedure described in experimental section.

The stability of the micelles was found to depend on the length of the alkyl chain ($n = 12, 14, 16, 18$ and 20) in the radical 9_n and degree of unsaturation in the hydrophobic chain in the surfactant **18** and **19** (Figure 3-1 and Table 3-1). $18/9_{18}$ was clear yellow dispersion immediately after preparation and the appearance did not change for one month (Table 3-1). Although the micelles of **18** with 9_n ($18/9_{16}$ and $18/9_{20}$) having shorter and longer alkyl chains than 9_{18} also gave clear yellow solution immediately after preparation, they collapsed within one month to give white precipitates. The radicals **9** (9_{12} and 9_{14}) with alkyl chains shorter than 9_{16} precipitated within 24 h after mixing with **18**. These observations for $3/9_n$ clearly indicate that the most appropriate chain length (n) in 9_n is **18**, probably because of a similar length to that of the hydrophobic part of **18** ($n = 17$). This strongly supports the interdigitated structure of $18/9_{18}$ similar to that of $6/9_{18}$ proposed in the chapter 2. However, the stability of the mixed micelles decreased significantly, when the alkenyl chain with the *cis*-configuration in **18** was replaced by saturated C_{17} alkyl chain in **19**. That is, $19/9_{16}$, $19/9_{18}$ and $19/9_{20}$ are less stable, and $19/9_{12}$ and $19/9_{14}$ are much less stable than $19/9_{18}$. This significant stability difference between $18/9_{18}$ and $19/9_{18}$ is likely to be caused by the difference in the chain length and/or rigidity due to the $C = C$ with *cis*-configuration. The CH/π interaction is also conceivable to increase the intermolecular interaction other than the hydrophobic one. From these observations shown in Table 3-1, the order of the stability in the micelle $18/9_n$ and $19/9_n$ is concluded to be $18/9_{18} > 18/9_{16}, 19/9_{16}, 19/9_{18}, 18/9_{20}$ and $19/9_{20} > 18/9_{14}, 19/9_{14}, 18/9_{12}$ and $19/9_{12}$.

After preparation of the mixed micelles, mean diameters of the resulting magnetic mixed micelles ($18/9_n$ and $19/9_n$, $n = 16, 18$ and 20) in PBS were measured by dynamic light scattering (DLS) and small angle neutron scattering (SANS) analyses. The mean diameter of $18/9_{18}$ was 16 nm as shown in Figure 3-2a even after the 1000-fold dilution (to 0.01 mM) with PBS, supporting the above conclusion of the high stability in $18/9_{18}$. In addition, the size of $18/9_{18}$ is the smallest among the micelles ($18/9_n$ and $19/9_n$, $n = 16, 18$ and 20), indicating that $18/9_{18}$ is likely to be packed more tightly in the interdigitated hydrophobic layer than the other micelles (Figure 3-3). The mean diameter (16 nm) of $18/9_{18}$ by DLS in PBS was also supported by SANS measurement in D_2O ; the SANS profile observed at iMATERIA (BL20, J-PARC) was in good agreement with the scattering function for spherical particles. The mean diameter was estimated to be 14 nm which is slightly smaller than that determined by DLS (16 nm) (see Figure 17 and 18 in the experimental section for details). This deviation is explained as follows. Because DLS is based on hydrodynamics of micelle diffusion, the

determined diameter of the $18/9_{18}$ reflects the whole micelle size including water. In contrast, SANS observes scattering length density difference (contrast) between the micelle and surrounding medium. The diameter of $18/9_{18}$ by SANS was estimated to be smaller than that by DLS, most likely due to the weak SANS contrast in the hydrophilic corona region which includes D_2O [75].

Table 3-1. Mean diameters and colloidal stability of the mixed micelles $18/9_n$ and $19/9_n$ ($n = 12 - 20$) in PBS at $30^\circ C$.

		9_{12} and 9_{14}	9_{16}	9_{18}	9_{20}
18	Diameter by DLS	—	18 nm ^a	16 nm ^a	22 nm ^a
	Observation	precipitates ^a	solution ^a → precipitates ^b	solution ^a → solution ^b	solution ^a → precipitate ^b
19	Diameter by DLS	—	21 nm ^a	17 nm ^a	58 nm ^a
	Observation	precipitates ^c	solution ^a → precipitates ^c	solution ^a → precipitates ^c	solution ^a → precipitates ^c

^aImmediately after preparation (Figure 3-2 and 3-3). ^bOne month after preparation. ^cOne day after preparation.

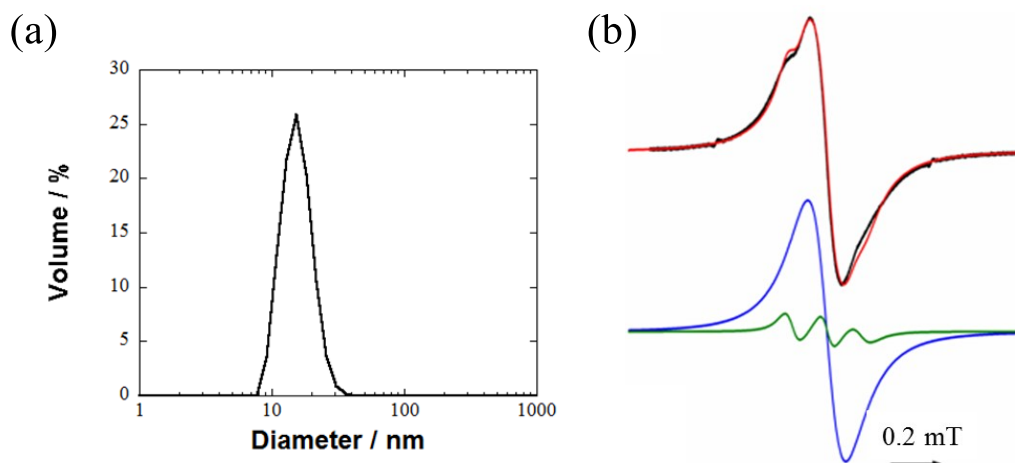


Figure 3-2. (a) Mean diameter (16 nm) of $18/9_{18}$ determined by DLS measurement in PBS. (b) EPR spectra of $18/9_{18}$ in PBS; experimental (black line) and simulated (red line) based on two components (blue line for singlet and green line for triplet component).

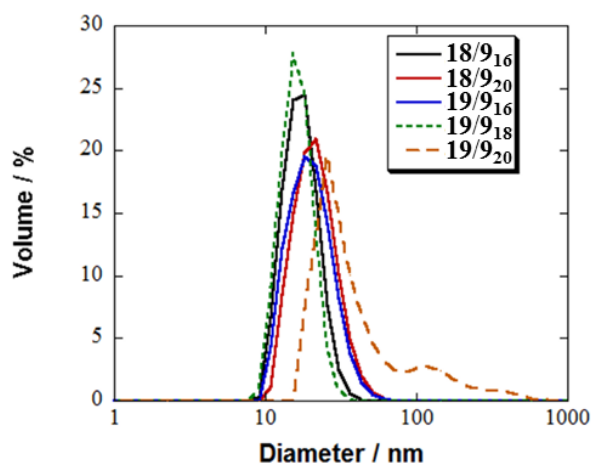


Figure 3-3. Mean diameters determined by DLS analysis at 25 °C of $18/9_{16}$ (black solid line), $18/9_{20}$ (red solid line), $19/9_{16}$ (blue solid line), $19/9_{18}$ (green dotted line) and $19/9_{20}$ (orange broken line) in PBS.

The EPR signal of $18/9_{18}$ consists mainly of broad singlet due to the Heisenberg spin exchange interaction among the nitroxide radicals [46,47]. By using the EPR spectral simulation by procedure of stochastic Liouville equation described by Freed *et al.*, the deconvolution of the signal shown in Figure 3-2b indicates contamination of the minor component (7%) along with the major fraction (93%). 9_{18} is considered to form self-assembling structure in the mixed micelle $18/9_{18}$, giving a broaden singlet signal (blue trace in Figure 3-2b) at the spin exchange frequency of $6 \times 10^8 \text{ s}^{-1}$. In contrast, the 7% fraction of 9_{18} well disperses and gives the triplet signal (green trace in Figure 3-2b) with smaller exchange frequency of $7 \times 10^7 \text{ s}^{-1}$. Since the spin exchange frequency is defined by the local concentration of 9_{18} , these two spectral components obviously reflect the two different locations of the radicals in the micelle structure. Most of the radicals are considered to be concentrated in the central region of the magnetic mixed micelle and the resulting spin exchange interaction is likely to stabilize the micelle significantly. The detail for the micelle structure of $18/9_{18}$ will be discussed below. The other less stable micelles ($18/9_{16}$, $18/9_{20}$, $19/9_{16}$, $19/9_{18}$ and $19/9_{20}$) gave similar EPR spectra consisting of a broad singlet signal as the major component and a triplet signal as the minor one (Figure 3-4), suggesting their similar structures to that of $18/9_{18}$.

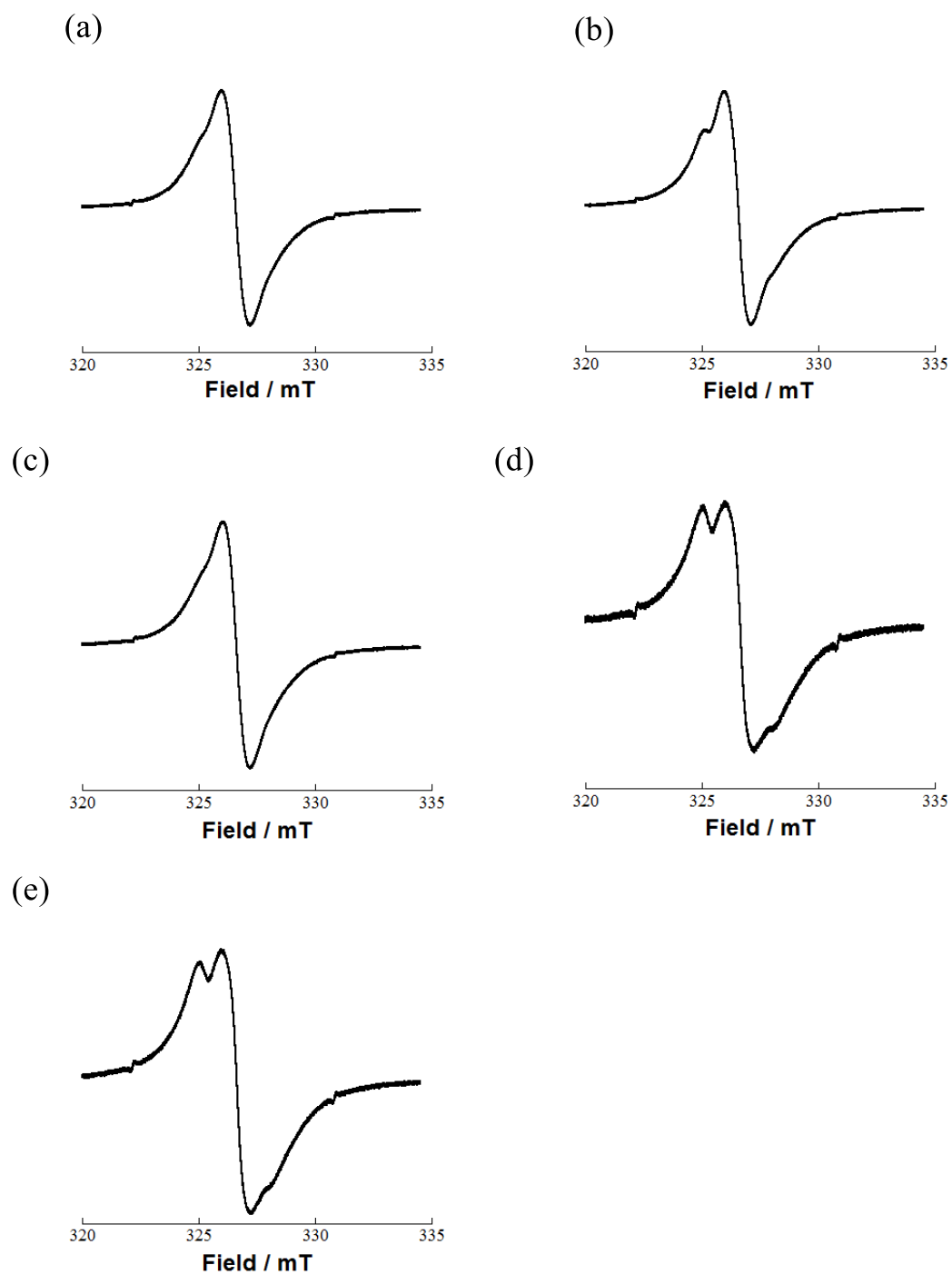


Figure 3-4. EPR spectra of (a) $18/9_{16}$, (b) $18/9_{20}$, (c) $19/9_{16}$, (d) $19/9_{18}$ and (e) $19/9_{20}$ in PBS with the internal standard Mn^{2+} .

When the molar ratio was changed on the preparation of the mixed micelles **18/9₁₈** containing 0 – 100 mol% of **9₁₈** in PBS, the diameter of the resulting micelle was found to be proportional to the molar content of **9₁₈** as shown in Figure 3-5. $R^2 = 0.991$

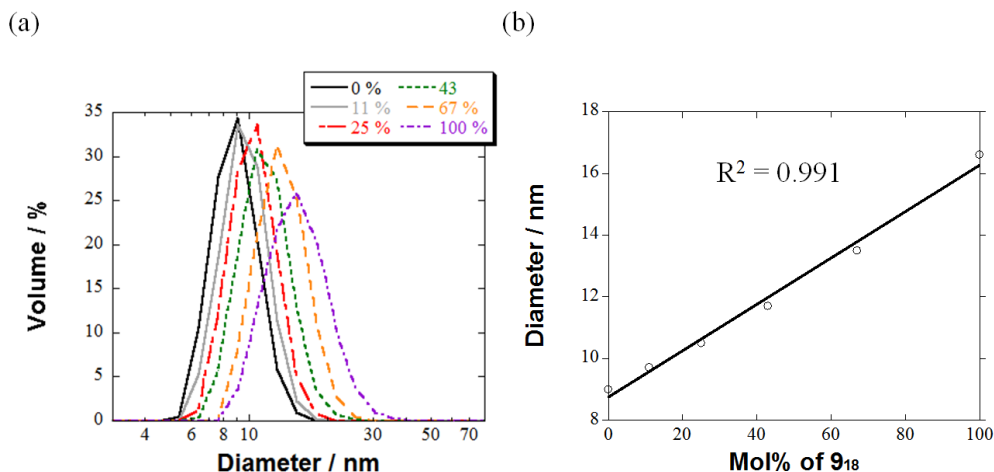


Figure 3-5. (a) The dependence of the mol% of **9₁₈** in **18/9₁₈** on the mean diameters by DLS at 25 °C in PBS (mol% of **9₁₈** = 0 (black solid line), 11 (gray solid line), 25 (red long-broken line), 43 (green dotted line), 67 (orange dashed line), and 100 (purple dashed and dotted line)). (b) Proportional relationship between the mol% of **9₁₈** in **18/9₁₈** and the mean diameter of **18/9₁₈**.

Simultaneously, the EPR spectra changed from the resolved triplet signal to the singlet one with increasing concentration of **9₁₈**, most likely due to the increase in the frequency of Heisenberg spin exchange interaction among the nitroxide radicals in the micelle (Figure 3-6).

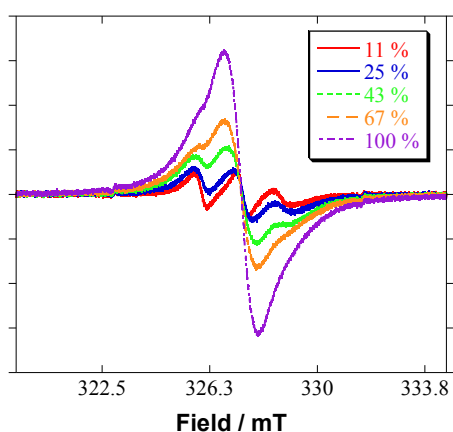


Figure 3-6. The dependence of the mol% of **9₁₈** in **18/9₁₈** on EPR spectra at 25 °C in PBS. Mol% of **9₁₈** = 11 (red solid line), 25 (blue solid line), 43 (green dotted line), 67 (orange broken line), and 100 mol (purple dashed and dotted line).

3-2-1-2. Preparation and stability of magnetic mixed micelles of 18/9₁₈/X (X = 11, 12 or 15)

The micelles of 18/9₁₈ including fluorophore (**11** and **12**) or drug (**15**), designated as 18/9₁₈/X (X = **11**, **12** or **15**), were prepared by adding **11** (10 mol%), **12** (1.0 mol%), or **15** (10 mol%) upon the preparation of 18/9₁₈. The experimental detail is described in the experimental section. The incorporation of **11** and **12** into the mixed micelles was confirmed by FL quenching (Figure 3-7a,b), which is known to be caused by surrounding nitroxide radicals [76,77,78]. However, the FL was revived by adding a large excess [20 equiv based on 9₁₈] of ascorbic acid as a reducing agent in both 18/9₁₈/X (X = **11** and **12**). As shown in Figure 3-7a and 3-7b, the intensity of FL started to increase, when the amount of radical monitored by EPR spectroscopy became less than half at around 30 min. These phenomena can be interpreted by reduction of the nitroxide radicals to *N*-hydroxy groups which cannot quench the fluorophores.

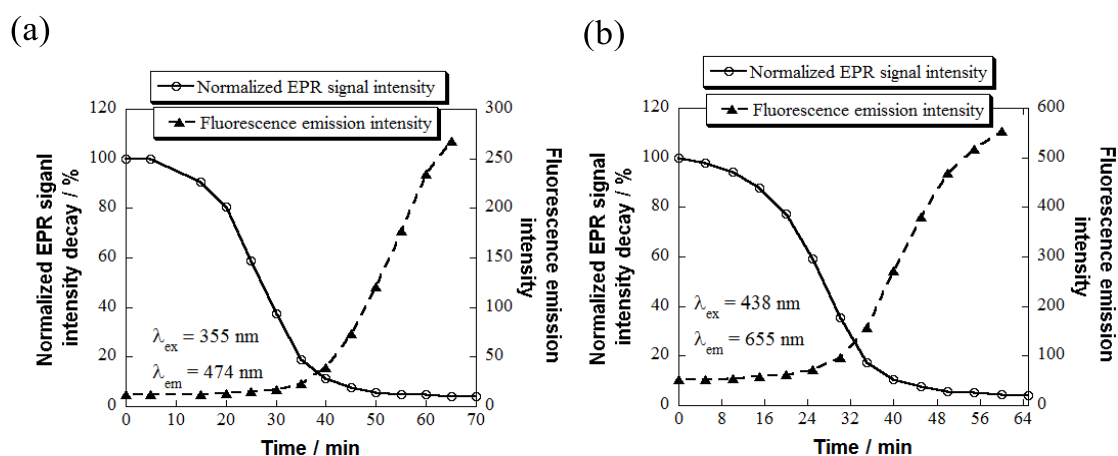


Figure 3-7. FL intensity change after addition of 20 equiv of ascorbic acid to (a) 18/9₁₈/11 and (b) 18/9₁₈/12 at 25 °C in PBS. The decrease and increase in the spectral intensity were monitored by EPR spectroscopy using a double-integration method and FL spectroscopy, respectively. See the experimental section for details.

The mean diameter (11 nm) of 18/9₁₈/15 was smaller than those of 18/9₁₈, 18/9₁₈/11 and 18/9₁₈/12 (16, 15 and 14 nm, respectively) (Figure 3-8a). 18/9₁₈/15 was found to be more stable than 18/9₁₈/11 and 18/9₁₈/12, based on the observation that 18/9₁₈/15 was dispersed stably more than one month, while the micelles of 18/9₁₈/11 and 18/9₁₈/12 disintegrated within one month giving white precipitates. In the EPR spectra, a broad singlet with a small portion of triplet was observed in 18/9₁₈/11 and 18/9₁₈/12 (Figure 3-8b and 3-8c, respectively), indicating a similar structure to 18/9₁₈ mentioned above (Figure 3-2b). That is, nitroxide radicals reside close to each other in the micelles 18/9₁₈/11 and 18/9₁₈/12, even if the fluorophore is encapsulated. In contrast, a triplet signal became the major component in the EPR spectrum of 18/9₁₈/15 due to lower frequency ($4.8 \times 10^7 \text{ s}^{-1}$) of

Heisenberg spin exchange interaction arising from slower translation diffusion of nitroxyl groups (Figure 3-8d), meaning much less radical proximity in $18/9_{18}/15$ than $18/9_{18}$ in spite of similar stability.

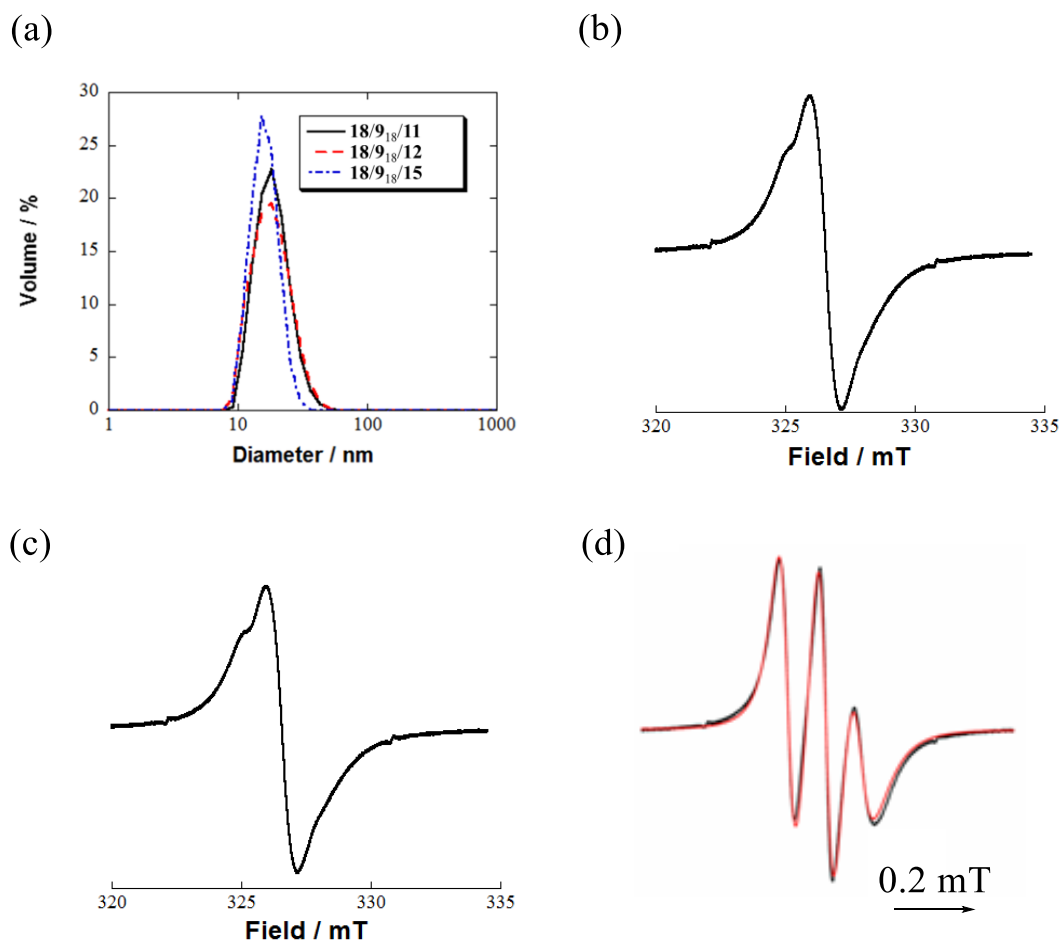


Figure 3-8. Characterization of $18/9_{18}/11$, $18/9_{18}/12$ and $18/9_{18}/15$. (a) Mean diameters determined by DLS analysis at 25 °C of $18/9_{18}/11$ (black line), $18/9_{18}/11$ (red dashed line) and $18/9_{18}/15$ (blue dashed and dotted line) in PBS. EPR spectra at 25 °C for (b) $18/9_{18}/11$, (c) $18/9_{18}/12$ and (d) $18/9_{18}/15$ experimental (black line) and simulated (red line) in PBS with the internal standard Mn^{2+} .

3-2-1-3. Stability of magnetic mixed micelles in the presence of a reducing agent

Ascorbic acid exists *in vivo* in the concentration ranging from μM to mM depending on the type of tissue [79]. When nitroxide radicals are applied to *in vivo* MRI, they are known to be reduced to the diamagnetic hydroxylamines by ascorbic acid, resulting in significantly weakening the MRI contrast [80,81,82]. For example, TEMPOL, one of the most typical water-soluble nitroxide radicals, is reduced quickly to the corresponding hydroxylamine in the presence of ascorbic acid [83,84,85,86,87,88]. In our molecular design, four long hydrophilic tails in **18** and four neighboring substituents in 9_{18} are expected to enhance resistance to ascorbic acid sterically. The decay of 9_{18} in $18/9_{18}$ in the presence of a large excess (20 equiv based on 9_{18}) of ascorbic acid in PBS was monitored

by EPR spectroscopy (Figure 3-9). The result was compared with that of **6/9**₁₈. As expected, **18/9**₁₈ showed much higher resistance ($t_{1/2} = 33$ min) than those of **6/9**₁₈ ($t_{1/2} = 7$ min) and TEMPOL ($t_{1/2} < 1$ min). This is because ascorbic acid was likely to be trapped by three hydrophilic polyethylene glycol (PEG) chains in **18** more tightly than single PEG chain in **6**; ascorbic acid was prevented from invading into **18/9**₁₈ more efficiently than **6/9**₁₈. Similarly, the resistivity of the nitroxide radical in **6/9**_{18/15} and **18/9**_{18/15} was evaluated (Figure 3-9). As a result, **6/9**_{18/15} and **18/9**_{18/15} showed much higher resistance ($t_{1/2} = 64$ min each) than the **6/9**₁₈ ($t_{1/2} = 7$ min) and **18/9**₁₈ ($t_{1/2} = 33$ min) did. These results suggest that the structure of **18/9**_{18/15} are quite different from those of **18/9**₁₈, **18/9**_{18/11} and **18/9**_{18/12}.

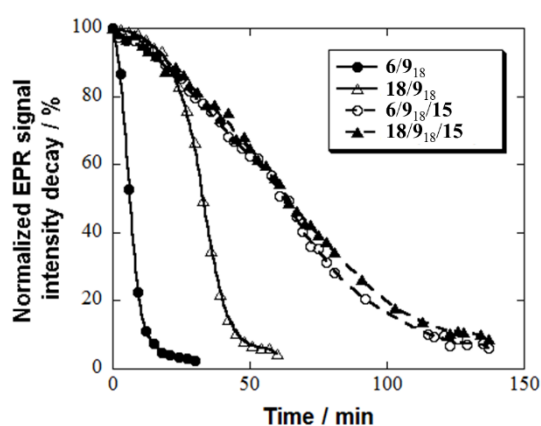


Figure 3-9. Comparison of the reduction resistance to a large excess of ascorbic acid between **6/9**₁₈, **18/9**₁₈, **6/9**_{18/15} and **18/9**_{18/15}. The reduction of the radical was monitored by EPR spectroscopy using a double-integration method. See the experimental section for details.

3-2-2. Theranostic Application

3-2-2-1. *In vitro* cytotoxicity of magnetic mixed micelles against HeLa cell

Since biocompatibility is a prerequisite for the magnetic mixed micelles as MRI contrast agents, the cancer cell viability of **18/9**₁₈ was assessed and compared with those of **6/9**₁₈ by the CCK-8 assay at the initial concentrations of 2.5 mM for **6**, **18** and **9**₁₈ (Figure 3-10a). **18/9**₁₈ exhibited no significant cytotoxicity to HeLa cells at concentrations up to 2.5 mM, whereas **6/9**₁₈ showed cytotoxicity at 0.31 mM or higher, demonstrating that **18/9**₁₈ is more appropriate than **6/9**₁₈ for *in vivo* applications. In contrast, **18/9**_{18/15} with the ratio of 1 : 1 : 0.001 at the initial concentrations of 2.5 mM for **18** and **9**₁₈, and 2.5 μ M for **15** displayed significant toxicity in 0.16 μ M or higher of **15** as with free **15** (Figure 3-10b). Thus, the fact that the drug **15** released from **18/9**_{18/15} is pharmaceutically active suggests that **18/9**_{18/15} was incorporated into the HeLa cells and useful as an MRI-visible DDS drug carrier.

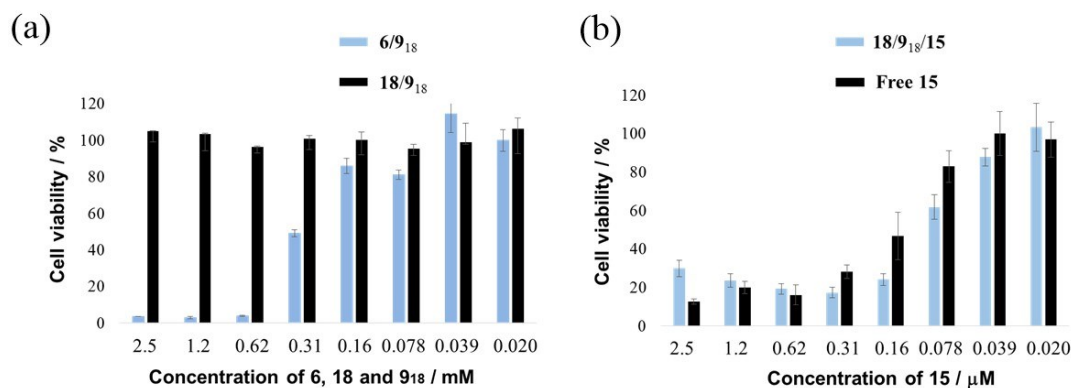


Figure 3-10. Comparison of the *in vitro* cytotoxicity between (a) 6/9₁₈ and 18/9₁₈, and (b) 18/9₁₈/15 and free 15 by using Hela cells. The initial solutions of 6/9₁₈, 18/9₁₈, 18/9₁₈/15 and free 15 were diluted with PBS up to 0.020 mM. The cell viability was assayed by using the CCK-8 kit after incubation for 24 h at 37 °C under 5% CO₂. See the experimental section for details.

3-2-2-2. MRI measurement

The longitudinal relaxation rate (r_1) of 18/9₁₈ was determined from relaxation time (T_1) as a function of concentration by the spin-echo method at 25 °C and compared with 6/9₁₈ (Figure 3-11). The T_1 values for the two magnetic mixed micelles (1.25–10 mM for each component) in PBS were evaluated by using an MRI machine at 7.0 T. Sufficiently bright T_1 -weighted MR phantom images were obtained at a concentration of 10 mM for both magnetic mixed micelles, compared with PBS (Figure 3-11a, Panel A and E), indicating that 18/9₁₈ would also show a distinct MRI contrast enhancement *in vivo* at this concentration or higher (Figure 2-12 in chapter 2). Linear regression analysis yielded $r_1 = 0.07 \text{ mM}^{-1}\text{s}^{-1}$ for 18/9₁₈ and $r_1 = 0.09 \text{ mM}^{-1}\text{s}^{-1}$ for 6/9₁₈ (Figure 3-11b); slower water exchange in 18/9₁₈ than 6/9₁₈ is most likely to be responsible for the difference in the r_1 value between the two magnetic mixed micelles. These r_1 values were less than that ($3.4 \text{ mM}^{-1}\text{s}^{-1}$) of Magnevist (a Gd³⁺ complex agent) in deionized water [59]. However, this result is quite natural because 9₁₈ with only one unpaired electron ($S = 1/2$) should show inferior water proton relaxivity to Gd³⁺ ($S = 7/2$).

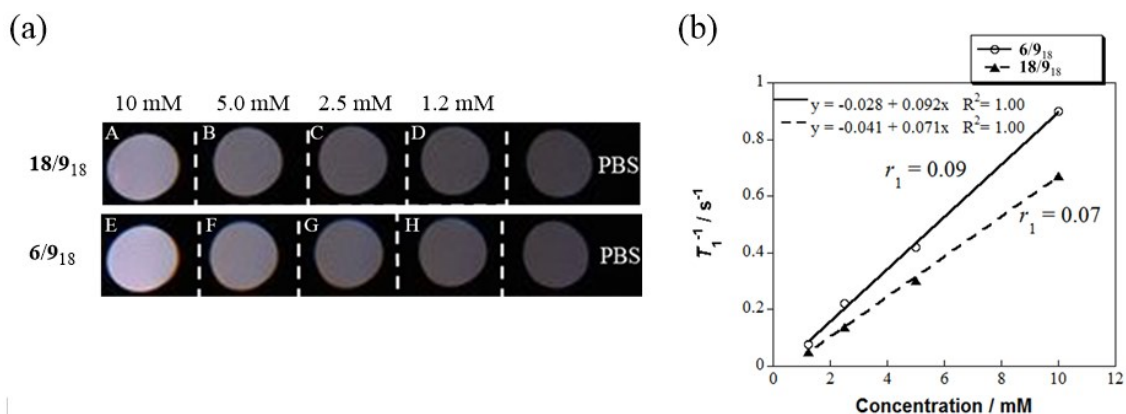


Figure 3-11. (a) T_1 -weighted MR phantom images (7.0 T, 25 °C) of (A) – (D) $18/9_{18}$ and (E) – (H) $6/9_{18}$ at 1.2, 2.5, 5.0, 10 mM in PBS, and PBS as control. (b) Plots of T_1^{-1} vs the concentrations of $18/9_{18}$ (dashed line) and $6/9_{18}$ (solid line) in the magnetic mixed micelles to determine the r_1 values. See the experimental section for details.

Interestingly, the $18/9_{18}/15$ exhibited brighter MRI contrast (Figure 3-12a) and the larger r_1 value ($r_1 = 0.14 \text{ mM}^{-1}\text{s}^{-1}$, Figure 3-12b) than those of $18/9_{18}/11$ and $18/9_{18}/12$ ($r_1 = 0.07$ and $0.06 \text{ mM}^{-1}\text{s}^{-1}$, respectively). These experimental results can be interpreted by the reduced rotation diffusion of 9_{18} inside the mixed micelles [89,90,91].

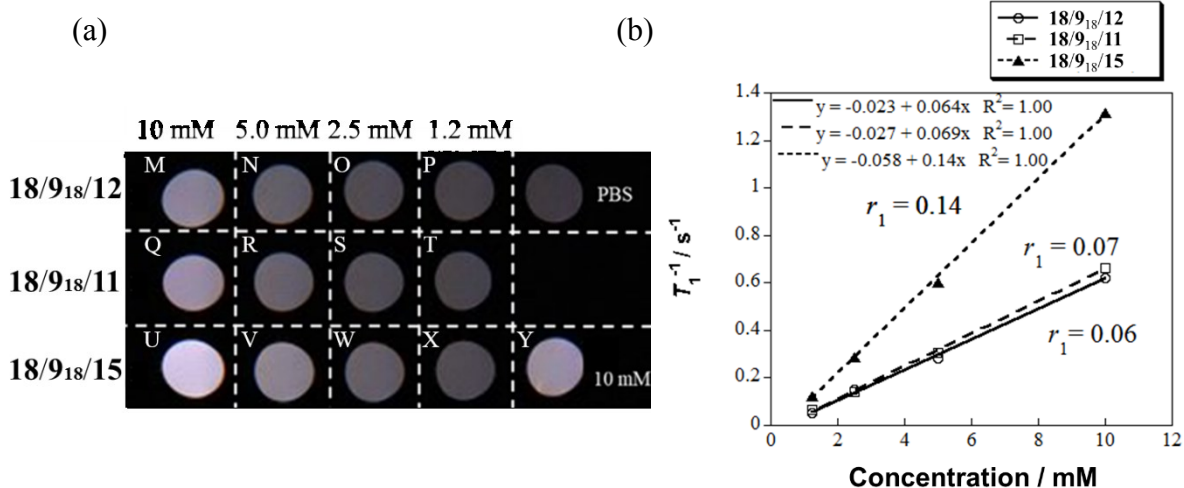


Figure 3-12. (a) T_1 -weighted MR phantom images (7.0 T, 25 °C) of (M – P) $18/9_{18}/12$, (Q – T) $18/9_{18}/11$, and (U – X) $18/9_{18}/15$, at 1.2, 2.5, 5.0, 10 mM in PBS, PBS as control, and $18/9_{18}$ (equimolar mixture) (10 mM each) (Y). (b) Plots of T_1^{-1} vs the concentrations of 9_{18} in the $18/9_{18}/12$, $18/9_{18}/11$ and $18/9_{18}/15$ to determine the r_1 values.

In order to estimate the rotation diffusion mobility of the radicals, the EPR spectra of the mixed micelles of $6/9_{18}$ and $18/9_{18}$ with the ratio of 1 : 0.01 and those including 10 mol% of **15** ($6/9_{18}/15$ and $18/9_{18}/15$ with the ratio of 1 : 0.01 : 0.1) in the temperature range of 263 to 313 K were numerically simulated as described. Representative EPR spectra of $18/9_{18}$ with a molar ratio of 1 : 0.01 and the results of their computer simulation are shown in Figure 3-13.

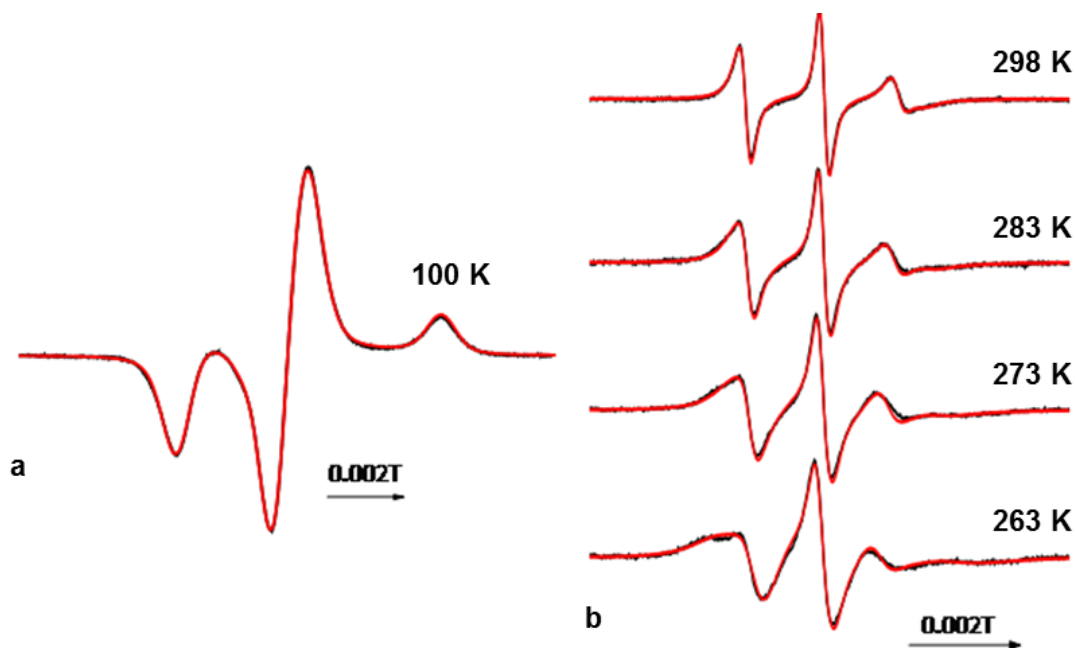


Figure 3-13. Representative EPR spectra of $18/9_{18}$ with a molar ratio of 1 : 0.01 and the results of their computer simulation at (a) 100 K and (b) higher temperatures. Black lines – experimental spectra, red lines – results of simulation. See the experimental section for details.

The rotation diffusion tensor of the radical in 9_{18} in all investigated micelles has axial symmetry. The rotation diffusion coefficient D_z is within the range $(1 \sim 8) \times 10^8 \text{ s}^{-1}$, but the values D_x and D_y are less than $2 \times 10^6 \text{ s}^{-1}$ (Table 3-2). Since the energy barrier of a flip-flop movement of 9_{18} in the mixed micelles is assumed to be much higher than that of a rotation along the long axis of the molecule, the slow-motion EPR spectra were simulated with imposing the constraint ($D_x = D_y$). It was found that the time scale of D_z of 9_{18} in the mixed micelles lied between 10^6 s^{-1} corresponding to the rigid-limit molecular rotation and 10^{10} s^{-1} corresponding to the molecular free rotation. The details for EPR simulation such as the definition of x, y and z axes are described in the experimental section and the appendix of the present chapter. In Table 3-3, one can see the typical dependence of the rotation characteristics of paramagnetic molecules on the temperature. The D_z value of 9_{18} in $6/9_{18}$ was identical with that in $18/9_{18}$. But the rotation mobility of 9_{18} in the $6/9_{18}/15$ and $18/9_{18}/15$ was 1.5 times lower than that in the corresponding micelles without **15** (Figure 3-14).

Table 3-2. Rotation diffusion coefficients and the angles determining the position of the main rotation axis in g-tensor frame for radical $\mathbf{9}_{18}$ in $\mathbf{18/9}_{18}$ (1 : 0.01), $\mathbf{18/9}_{18/15}$ (1 : 0.01 : 0.1), $\mathbf{6/9}_{18}$ (1 : 0.01) and $\mathbf{6/9}_{18/15}$ (1 : 0.01 : 0.1).

Temp., K	$\mathbf{18/9}_{18}$			$\mathbf{18/9}_{18/15}$			
	$D_z, 10^8 \text{ s}^{-1}$	Beta ^a , °	Gamma ^a , °	$D_z, 10^8 \text{ s}^{-1}$	Beta ^a , °	Gamma ^a , °	
313	10.17	53.2	55.8	8.44	53.0	58.2	
308	8.53	52.8	56.8	7.06	52.6	61.4	
303	7.53	52.2	55.9	5.84	52.1	64.1	
298	6.43	51.6	56.0	4.87	51.4	64.2	
293	5.77	51.1	58.9	4.2	50.7	67.1	
288	4.97	50.3	61.7	3.64	49.4	69.4	
283	4.61	49.3	63.7	3.22	47.8	68.2	
278	3.96	48.5	67.5	2.71	47.1	72.3	
273	3.46	47.5	73.2	2.32	45.8	68.8	
268	3.04	46.2	90.0	1.92	44.4	67.8	
263	2.45	45.4	89.9	1.41	43.7	61.9	
Temp., K	$\mathbf{6/9}_{18}$			Temp., K	$\mathbf{6/9}_{18/15}$		
	$D_z, 10^8 \text{ s}^{-1}$	Beta ^a , °	Gamma ^a , °		$D_z, 10^8 \text{ s}^{-1}$	Beta ^a , °	Gamma ^a , °
298	6.71	52.1	57.3	313	9.10	53.1	63.1
293	6.11	51.2	56.9	308	7.39	53.0	63.7
288	5.57	50.3	57.3	303	6.22	52.3	67.7
283	5.10	49.6	58.6	298	5.11	51.9	69.0
281	4.78	49.3	58.5	293	4.41	50.9	71.9
279	4.57	48.9	59.2	288	3.64	50.3	72.7
277	4.43	48.4	58.6	283	3.37	48.4	78.2
275	4.33	48	59.9	278	3.09	46.5	90.0
273	4.14	47.3	62.4	273	2.14	44.5	69.3
271	4.02	47	62.2	268	2.14	44.5	69.3
269	3.83	46.3	62.4	263	1.63	43.9	67.5
267	3.58	45.8	68.3				
265	3.37	45.2	66.4				
263	3.08	44.5	71.8				

^aEuler angles describe the transformation of rotation frame to g-tensor frame.

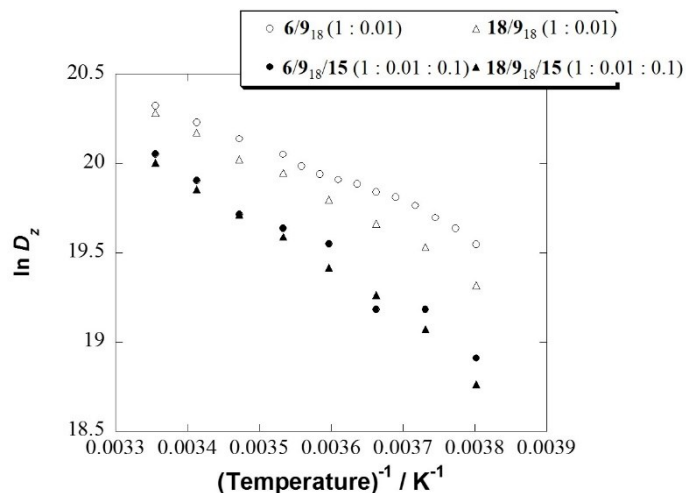


Figure 3-14. Temperature dependence of rotation diffusion coefficient D_z of $\mathbf{9}_{18}$ in $\mathbf{6/9}_{18}$ and $\mathbf{18/9}_{18}$ with the ratio of 1 : 0.01, and $\mathbf{6/9}_{18}/\mathbf{15}$ and $\mathbf{18/9}_{18}/\mathbf{15}$ with the ratio of 1 : 0.01 : 0.1. See the experimental section for details.

The temperature-dependence of the rotation diffusion mobility is successfully described by Arrhenius law with values of activation energy (E_z^a) shown in Table 3-3, indicating that **15** reduces the mobility of $\mathbf{9}_{18}$ and gives enhanced MRI signal.

Table 3-3. The effective activation energy of rotation diffusion of $\mathbf{9}_{18}$ in $\mathbf{6/9}_{18}$ and $\mathbf{18/9}_{18}$ with the ratio of 1 : 0.01, and $\mathbf{6/9}_{18}/\mathbf{15}$ and $\mathbf{18/9}_{18}/\mathbf{15}$ with the ratio of 1 : 0.01 : 0.1.

Mixed micelle	E_z^a / kJ/mol
6/9₁₈	17.8 ± 1.2
18/9₁₈	18.4 ± 0.6
6/9₁₈/15	22.4 ± 0.9
18/9₁₈/15	22.9 ± 0.6

The E_z^a of $\mathbf{9}_{18}$ also approximately evaluated by the quantum chemical calculations. The energy barriers for two intramolecular rotations marked by arrows in Figure 3-15a were estimated by using $\mathbf{9}_7$ and the example of the energy profile obtained is shown in Figure 3-15b. The energy profiles for two possible intramolecular rotations showed that the energy barriers were 10-13 kJ/mol. These values are smaller than the effective activation energies of the rotation diffusion of the nitroxyl fragment obtained in Table 3-3.

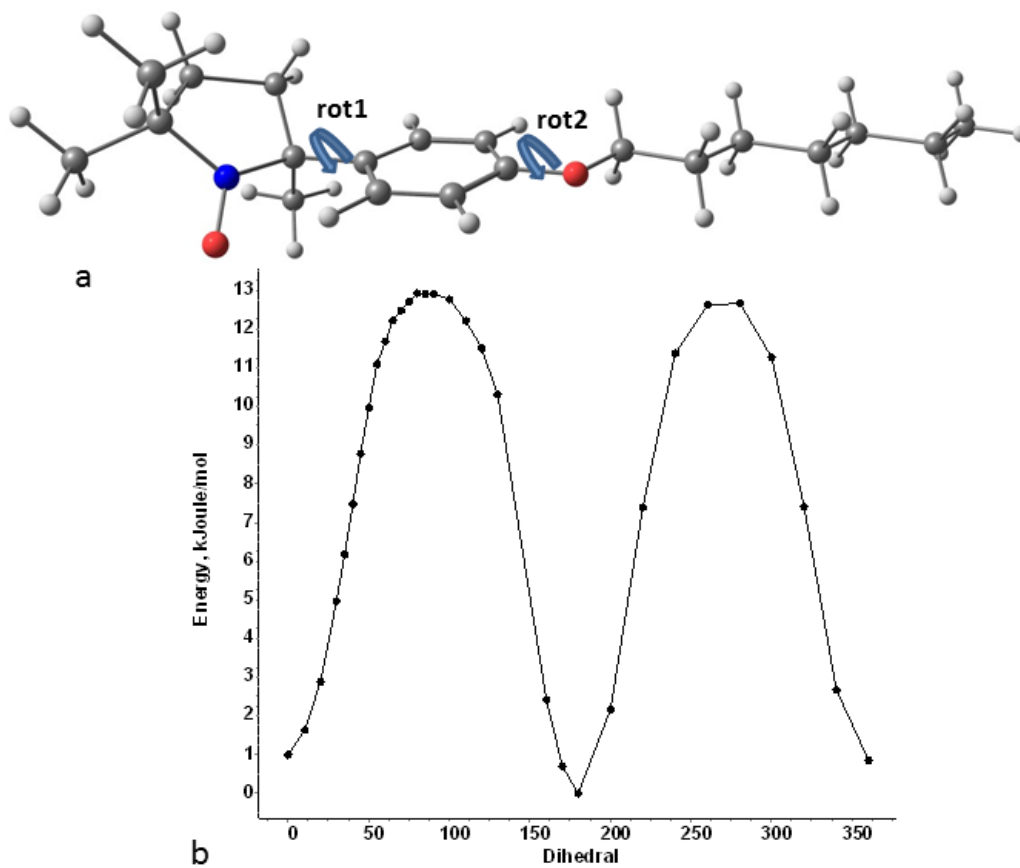


Figure 3-15. (a) The optimal geometry of **9₇** and (b) the energy profile for rotation 1. See the experimental section for details.

Finally, the magnetic mixed micelle **18/9**₁₈ was applied to *in vivo* MRI in mice. As shown in Figure 3-16, distinct MRI contrast enhancement with high reproducibility was observed in the liver after injection. This result demonstrates that the magnetic mixed micelles are effective as an *in vivo* T_1 -weighted MRI contrast agent.

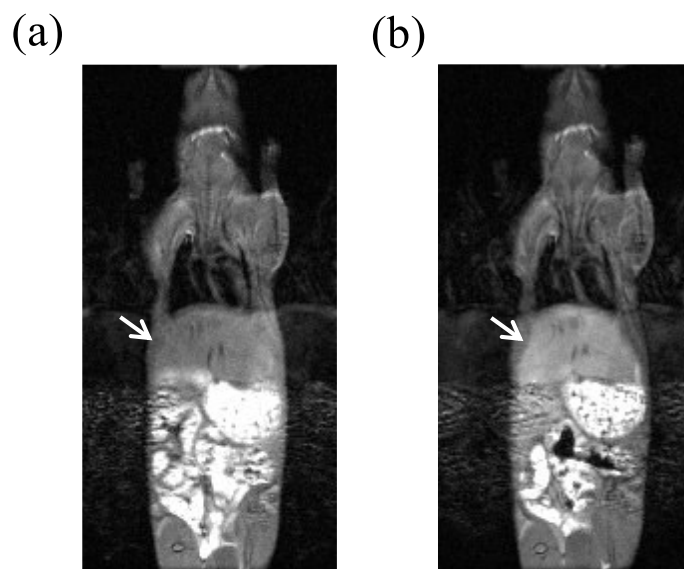


Figure 3-16. Coronal T_1 -weighted MR images of a male ICR mouse: (a) before and (b) 23 min after the intravenous injection of 200 μL of **18/9**₁₈ in PBS. Distinct contrast enhancement was observed in the liver (indicated by white arrows). See the experimental section for details.

3-3. Conclusions

We have prepared highly robust, size-tunable and biocompatible metal-free magnetic mixed micelles **18/9**₁₈. The structure of the magnetic mixed micelles was characterized by DLS analysis and EPR spectral simulation.

The guest-unloaded magnetic mixed micelles **18/9**₁₈ showed lower cytotoxicity, high colloidal stability and higher reduction resistance to a large excess of ascorbic acid, compared with previously reported magnetic mixed micelles **6/9**₁₈ described in chapter 2. In addition, **18/9**₁₈ demonstrated sufficient contrast enhancement in the T_1 weighted MR images *in vitro* and *in vivo*.

Furthermore, the mixed micelle encapsulated a hydrophobic drug paclitaxel (**15**) (10 mol %), or hydrophobic fluorophores such as pyrene (**11**) (10 mol%) and tetraphenylporphyrin (**12**) (1.0 mol%) to give stable micelles with mean particle sizes of less than 20 nm. The **15**-loaded magnetic mixed micelles, **18/9**₁₈/**15**, effectively suppressed HeLa cell growth. Thus, such highly biocompatible magnetic mixed micelles can be utilized in theranostic nanomedicine for targeted drug delivery system visible by MR or FL images.

3-4. Experimental section

3-4-1. Materials

The surfactants **6** [Brij 58 (Sigma-Aldrich)], **18** [Tween 80 (DKS Co. Ltd.)] and **19** [Tween 60 (DKS Co. Ltd.)], pyrene (**11**) (Sigma-Aldrich), tetraphenylporphyrin (**12**) which was kindly gifted by Mr. Kazuaki Yamanaka (Kyoto University) and paclitaxel (**15**) (Sawai Pharmaceutical) were used as received.

3-4-2. Preparation of magnetic mixed micelles in PBS

3-4-2-1. Magnetic mixed micelles

As a typical example, **6/9**₁₈ and **18/9**₁₈ (10 mM each) were prepared in PBS as follows. To a 4 mL glass vial containing **9**₁₈ [7.09 mg (15 μmol)] dissolved in very small amount of ether was added **6** or **18** [10 mM] dissolved in PBS (1.5 mL). The mixture was subjected to sonication (Branson Model 2510, power 125 W, frequency 42 kHz) for 3 min at 25 °C to give a white suspension. Finally, the suspension was heated for 10 min at 90 °C using a water bath to form ether-free transparent **18/9**₁₈, which were passed through a 0.45 μm φ membrane filter.

3-4-2-2. Magnetic mixed micelles containig guest (X)

3-4-2-2-1. X: Fluorophores

18/9_{18/11} and **18/9**_{18/12} (**18** and **9**₁₈: 10 mM each, **11** and **12**: 10 mol% and 1.0 mol% based on **18**, respectively) were prepared in PBS as follows. To a 4 mL glass vial containing 11.83 mg (25 μmol) of **9**₁₈ and 0.51 mg of **11** (2.5 μmol, 10 mol% based on **9**₁₈) or 0.15 mg of **12** (0.25 μmol, 1.0 mol% based on **9**₁₈) dissolved in very small amount of an appropriate organic solvent (ether for **11**, dichloromethane for **12**) was added **18** (10 mM) dissolved in PBS (2.5 mL). The mixture was subjected to sonication to give a white suspension. Finally, the suspension was heated for 10 min at 90 °C using a water bath to form the solvent-free transparent **18/9**_{18/11} and **18/9**_{18/12}, which were passed through a 0.45 μm φ membrane filter.

3-4-2-2-2. X: Anti-cancer drug

As a typical example, **18/9**_{18/15} (**18** and **9**₁₈: 10 mM each, **15**: 10 mol% based on **18**) was prepared in PBS as follows. To a 4 mL glass vial was added 142 μL (0.85 mg, 1.0 μmol) of paclitaxel (**15**) formulation including polyoxyethylene castor oil and ethanol, and the ethanol was removed under vacuum. Then, 4.73 mg (10 μmol) of **9**₁₈ dissolved in very small amount of ether was added to the vial. To this vial was added **18** (10 mM) dissolved in PBS (1.0 mL) and the mixture was subjected to sonication to give a white suspension. Finally, the suspension was heated for more than 10 min at 90 °C using a water bath to form the ether-free transparent **18/9**_{18/15}, which was passed through a 0.45 μm

ϕ membrane filter. **18/9₁₈/15** with the ratio of 1 : 0.01 : 0.1 and 1 : 1 : 0.1 for EPR simulation and cell experiment, respectively, were prepared in the same procedure.

3-4-3. Characterization of magnetic mixed micelles

3-4-3-1. DLS measurement

The mean diameter of the mixed micelles was measured at 25 °C using a UPA-UT151 instrument (MicrotrackBEL). After the samples were passed through a 0.45 μm ϕ disposable membrane filter, the particle size was measured in PBS using an attached cuvette. The mean diameter was calculated on volume and number weighted averages from five measurements for each sample. Only volume average size distributions are shown in the Figures of this study.

3-4-3-2. SANS measurement

18/9₁₈ (10 mM each) was prepared in D₂O to induce a strong contrast for SANS experiment. SANS measurements were conducted by use of iMATERIA (BL20) [55] at the Materials and Life Science Experimental Facility (MLF) of the Japan Proton Accelerator Research Complex (J-PARC).

In Figure 3-17, the open circles indicate the SANS profile obtained after circular-averaging the scattered neutron distribution on the large area detector. The horizontal axis, q is the magnitude of scattering vector [= $(4\pi/\lambda)\sin(\theta/2)$, λ is neutron wavelength, and θ is scattering angle]. The SANS profile was converted to the absolute unit [cm^{-1}] by use of the glassy carbon standard provided by Dr. Jan Ilavsky [56].

In Figure 3-17, the dotted line indicates the numerically calculated profile, $I(q)$.

$$I(q) = \left\{ \int W(R) I_{\text{sph}}(q; R) dR \right\} \left\{ \exp[-(L_{\text{dif}}^2 q^2 / 2)] \right\}^2 + I_{\text{inc}} \dots\dots\dots \text{(Eq. 3-1)}$$

Here, $I_{\text{sph}}(q; R)$ is a scattering function due to spherical particles with radius R , $W(R)$ is radius distribution, L_{dif} is the thickness of diffusion layer between the mixed micelle and the surrounding solvent phase, and I_{inc} is q -independent incoherent scattering term [57].

$$I_{\text{sph}}(q; R) = N \Delta\rho^2 (4\pi R^3 / 3)^2 [\sin(qR) - qR \cos(qR)]^2 / (qR)^6 \dots\dots\dots \text{(Eq. 3-2)}$$

N is a number density of spherical particles. $\Delta\rho$ is a neutron scattering length density difference between the mixed micelle and the surrounding solvent phase. As a radius distribution, we employed log-normal distribution.

$$W(R) = \exp[-(\ln(R) - \ln(R_{\text{Median}}))^2 / \sigma^2] / (\sigma R) \dots\dots\dots \text{(Eq. 3-3)}$$

R_{Median} is a median value of R distribution. σ is a standard deviation of $\ln(R)$. The SANS profile observed for the mixed micelle solution was in good agreement with the numerical calculation by use of $R_{\text{Median}} = 55 \text{ \AA}$, $\sigma = 0.66$, and $L_{\text{dif}} = 9.5 \text{ \AA}$. The corresponding particle radius distribution function was shown in Figure 3-18. From the obtained parameters, the mean radius (R_{mean}) is calculated to be 68.4 \AA by use of the following equation.

$$R_{\text{mean}} = R_{\text{Median}} \exp(\sigma^2 / 2) \dots\dots\dots (\text{Eq. 3-8})$$

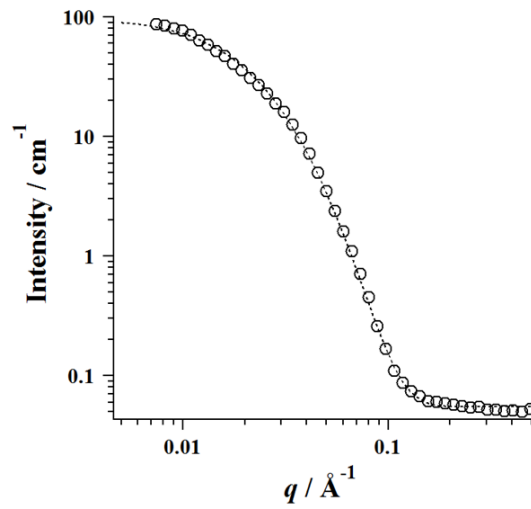


Figure 3-17. SANS profile of $18/9_{18}$ in D_2O , as indicated by open circles. The dotted line indicates the numerically calculated profile. In the calculation, we assumed the particle radius distribution obeys log-normal function ($R_{\text{Median}} = 55 \text{ \AA}$ and $\sigma = 0.66$), and considered a diffusion layer between mixed micelle and surrounding solvent phase, whose thickness, L_{dif} to be 9.5 \AA .

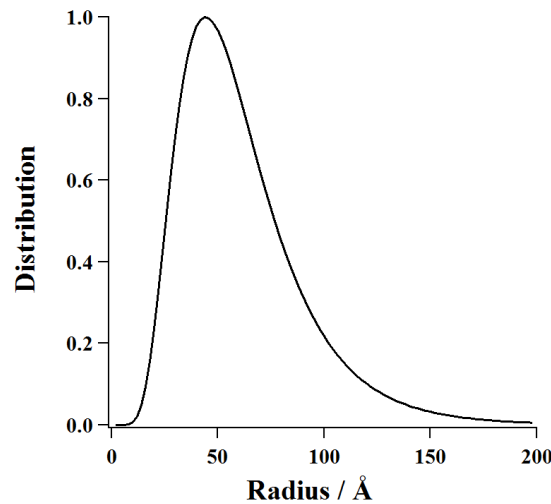


Figure 3-18. Radius distribution of $18/9_{18}$ evaluated by SANS profile investigation.

3-4-3-3. Fluorescence spectroscopy (Figure 3-7)

The fluorescent spectra of **11** in **18/9**₁₈/**11** or **12** in **18/9**₁₈/**12** were measured at 25 °C with the RF-5300PC spectrofluorometer (Shimadzu) using excitations at 355 nm for **11** or $\lambda_{\text{ex}} = 438$ nm for **12**. Band widths of 3 nm for excitation and 3 nm for emission were used. After addition of 20 equiv of ascorbic acid to the cuvette, the emission intensity at 474 nm for **11** and 655 nm for **12** appeared and increased.

3-4-3-4. EPR spectroscopy

3-4-3-4-1. EPR measurement (Figures 3-2b, 3-4, 3-6, 3-7 and 3-8b-d)

The EPR spectra of **18/9**₁₈ and **18/9**₁₈/**15** were recorded at the temperature 298K on JES-RE2X spectrometer (JEOL) (X-band). The samples were placed into capillary tubes (~1 mm ϕ) to avoid the decrease in the Q value. The experiments were performed at the microwave power which did not lead to the signal saturation (1.00 mW). Modulation amplitude was 0.25 mT.

The EPR spectra of **18/9**₁₈ with a molar ratio of 1: 0.01, and **18/9**₁₈/**15** with a molar ratio of 1 : 0.01 : 0.1 were recorded at 100 K and in temperature range (263 ~ 313) K on Bruker EMX Plus spectrometer (X-band). The variable temperature unit of Bruker was used to control temperature. Microwave powers were chosen carefully, especially in the low-temperature measurements, to prevent the signal saturation which was derived from prolonged spin-lattice relaxation time of a radical's magnetization vector. Modulation amplitudes were kept below 1/2 to 1/3 times of peak-to-peak line widths. For experiments at 298K the samples were placed into glass capillary tubes (~1 mm ϕ). For 100 K experiments, the samples in the plastic tubes (~ 4 mm ϕ) were dipped quickly in liq. N₂ to be frozen.

3-4-3-4-2. Determination of the magnetic micelles reduction resistance to excess ascorbic acid (Figure 3-9)

To **6/9**₁₈, **18/9**₁₈, **6/9**₁₈/**15** and **18/9**₁₈/**15** [concentration of **15** was 10 mol% based on **6** or **18** (10 mM each)] in PBS (1.5 mL) was added 20 equiv of ascorbic acid based on **9**₁₈. The mixture was transferred to a capillary tube (1 mm ϕ) immediately, followed by measurement of the EPR spectra during the process of the radical reduction. The concentration of ascorbic acid was 200 mM. The spectra were collected with the following parameters: 1.00 mW of microwave power, 0.25 mT of modulation for **6/9**₁₈ and **18/9**₁₈ (or 0.079 mT for those with **15**), 0.10 s of time constant, and 120 sec of sweep time.

3-4-3-4-3. Fitting procedure for slow- and slow-motion EPR spectra (Figures 3-13 and 3-14, and Tables 3-2 and 3-3)

To obtain information about magnetic parameters and characteristics of rotation mobility of paramagnetic molecules inside the micelles, the nonlinear least-squares fitting of EPR spectra of the

magnetically diluted samples were performed. Microwave powers were chosen carefully, especially in the low-temperature measurements to prevent the microwave saturation which was derived from prolonged spin-lattice relaxation time of a radical's magnetization vector. For analysis of the spectra of frozen samples the original software ODF3 described in ref [92] was used. Fitting of the spectra recorded at (263 ~ 313) K was made by the method described in [93]. A convolution of Gaussian and Lorentzian functions, as the most general representation of individual EPR line shapes, was applied for simulation. The programs used allowed taking into account the dependence of a line shape on the orientation of the species in magnetic field that reflects line broadening as a result of an unresolved anisotropic hyperfine interaction. The example of simulation of the spectrum recorded at 100 K is shown in Figure 3-14a. As a result of such simulation the magnetic parameters (main values of g - and HFS-tensors) were obtained and used further to analyze the spectra recorded at high temperatures. The coefficients of rotation diffusion as well as the directions of the rotation axes were obtained by the simulation. It was established that rotation diffusion tensor of $\mathbf{9}_{18}$ in all investigated micelles has axial symmetry. The rotation diffusion coefficient D_z lies in the interval $(1 - 10) \times 10^8 \text{ s}^{-1}$ but the values D_x and D_y are less than $2 \times 10^6 \text{ s}^{-1}$.

3-4-3-4-4. Calculation of the inertia tensors and the intramolecular rotation energy barriers for nitroxide radical (Figure 3-15)

The main values and the directions of the principal axes of inertia tensor for $\mathbf{9}_7$ were calculated using molecular geometry optimized by DFT calculation. Only seven carbon atoms in saturated substitute were taken into account. The geometry optimization was carried out using program package ORCA in model B3LYP/6-31g(d,p) for continuum medium (COSMO, toluene at temperature 293K). For each rotation the optimization of geometry and determination of full energy of the system was performed with steps of $(5-20)^\circ$. The energy barriers came to 11 kJ/mol and 13 kJ/mol for rotations 1 and 2 correspondently.

3-4-4. Evaluation method of in vitro cytotoxicity (Figure 3-10)

HeLa cells (3,600 to 8,000 cells in 100 μL per well) were seeded at in a 96-well tissue culture plate with Dulbecco's modified Eagle's medium (DMEM) containing 10% fetal bovine serum and 1% penicillin/streptomycin and grown for 24 h at 37 $^\circ\text{C}$ with 5% CO_2 . Then, each well was treated with a PBS solution (10 μL) of $\mathbf{6/9}_{18}$ and $\mathbf{18/9}_{18}$, $\mathbf{18/9}_{18}/\mathbf{15}$ or free $\mathbf{15}$. The initial solution of $\mathbf{6/9}_{18}$ or $\mathbf{18/9}_{18}$ (2.5 mM each) and $\mathbf{18/9}_{18}/\mathbf{15}$ ($\mathbf{18}$ and $\mathbf{9}_{18}$: 2.5 mM, $\mathbf{15}$: 2.5 μM) or free $\mathbf{15}$ (2.5 μM) and diluted solution of 1.2, 0.62, 0.31, 0.16, 0.078, 0.039 and 0.020 mM (or μM) was before incubation. After incubation for 24 h at 37 $^\circ\text{C}$ under 5% CO_2 , these compounds shown above were removed and then cell toxicity was assayed using CCK-8 kit according to the manual provided by the kit manufacture (Dojindo Molecular Technologies).

3-4-5. *In vitro* MRI measurement (Figures 3-11 and 3-12)

In vitro T_1 -weighted MRI measurement was conducted on a 7-Tesla preclinical scanner (BioSpec 70/20 USR; Bruker BioSpin MRI GmbH, Ettlingen, Germany). The initial PBS solution of **6/9**₁₈ and **18/9**₁₈ (10 mM each), or **18/9**_{18/11}, **18/9**_{18/12} and **18/9**_{18/15} [**11**, **12** and **15** were 10 mol%, 1.0 mol% and 10 mol% based on **6** or **18** (10 mM each), respectively] were diluted with PBS up to 1.2 mM before measurement. After these mixed micelles were transferred to plastic tubes, they were fixed in a sample holder. The MR relaxometry was conducted at 25 °C. MR phantom images were obtained by a rapid acquisition with relaxation enhancement (RARE) pulse sequence with variable repetition time (TR) [echo time (TE) = 11 ms, rare factor = 2, repetition time (TR) = 5,000, 3,000, 1,500, 800, 400, 200, 100 and 50 ms, field of view = 80 × 40 mm², acquisition matrix size = 256 × 128, slice thickness = 2.00 mm]. In the acquired images, region-of-interest (ROI) was set on each tube and the mean signal intensities within the ROI were measured for the TR-varied images. T_1 values were calculated by fitting a saturation recovery equation to the plot of signal intensity versus TR by using the image sequence analysis tool in ParaVision 5.1 (Bruker BioSpin). The longitudinal relaxivity (r_1) was calculated with Eq. 3-9:

$$1/T_1 = 1/T_{1(0)} + r_1 C \dots \dots \dots \text{(Eq. 3-9)}$$

where $T_{1(0)}$ and C are the longitudinal relaxation time in the absence of the paramagnetic species and the concentration of the paramagnetic species, respectively.

3-4-6. *In vivo* MRI measurement (Figure 3-16)

3-4-6-1. *Animal preparations*

All animal procedures were conducted in accordance with guidelines of animal experiments of Kyoto University (Approval number: 30–A–9). Male ICR mice (n = 2, aged 7 weeks, body weight 32 - 34 g; JAPAN SLC. Inc., Shizuoka, Japan) were used. After the induction of anesthesia with isoflurane, mice were placed in a cradle in prone position. The anesthesia was kept with an inhalation of 2% isoflurane in air at 1.4 L/min through a face mask. Respiratory rate and rectal temperature were continuously measured using a pressure-sensitive respiration sensor and thermistor temperature probe, respectively, and monitored using a monitoring system (Model 1025, MR-compatible Small Animal Monitoring & Gating System; SA Instruments, Inc., NY, USA) with a dedicated software (PC-SAM V.5.12; SA Instruments). The body temperature was maintained by a flow of warm air using a heater system (MR-compatible Small Animal Heating System, SA Instruments).

3-4-6-2. *In vivo* MRI acquisition

MR measurements were conducted on a 7-Tesla preclinical scanner (BioSpec 70/20 USR; Bruker BioSpin MRI GmbH, Ettlingen, Germany). A quadrature transmit-receive volume coil (inner diameter 72 mm, T9562; Bruker BioSpin) was used for MR signal detection. After two hundred microliter (μL)

of **18/9**₁₈ (40 mM each) in PBS were intravenously injected into an anesthetized male ICR mouse (body weight: 32~34 g) lying pronely in an animal holder, MRI data were acquired with a dedicated operation software (ParaVision 5.1; Bruker BioSpin). Two-dimensional multi-slice spin-echo pulse sequence with a fat suppression was used for acquiring T_1 -weighted images. The acquisition parameters were as follows: repetition time (TR), 200 ms; echo time (TE), 6.2 ms; field of view (FOV), $80 \times 40 \text{ mm}^2$; acquisition matrix size, 256×128 ; spatial resolution of $312 \mu\text{m}$; coronal orientation; slice thickness, 2 mm; number of slices, 8; number of averages, 2; and scan time, 51.2 s.

3-4-7. TEM study

For the observation of morphology of the mixed micelle, TEM images were recorded on a Hitachi H-7650 transmission electron microscope (Hitachi High-Technologies, Tokyo, Japan) at an acceleration voltage of 120 kV.

One drop of the mixed micelle **18/9**₁₈ (40 mM each) or **P18** (40 mM) in PBS was placed onto a 400 mesh a Cu grid covered with a collodion membrane, where hydrophilic treatment was performed. After the grid was tapped with a filter paper to remove surface water, it was negatively stained by using a 1% uranyl acetate solution and air-dried before measurement. Subsequently, it was inserted into the TEM machine to start the measurement. Typical imaging parameters were as follows: Exposure = 960 ms; Frame rate = 8.2 fps; Bin = 1; Gain = 1.0; Integ = 2.00; Pixel (x, y) = (2048, 2048).

3-5. Appendix

3-5-1. Structural characterization of the magnetic mixed micelle 18/9₁₈

In order to consider the structure of the mixed micelle, we begin with the structure of the simple micelle consisting only of **18**, designated as **P18**. The size and structure of a micelle are known to be determined by hydrophilic-hydrophobic balance. The actual determinants per one surfactant molecule are length (l) and volume (v) in the hydrophobic part and area (a) in hydrophilic-hydrophobic interface. The l and v of the saturated alkyl chain (C_nH_{2n+1}) are reported to be determined by the following equations [94].

$$l = 0.154 + 0.1265n \text{ nm}$$

$$v = (27.4 + 26.9n) \times 10^{-3} \text{ nm}^3$$

In the case of **P18** (Figure 3A-1a), l and v of the hydrophobic part of **18** ($n = 17$ in Figure 3-1) are calculated to be 2.3 nm (l_{18}) and 0.48 nm³ (v_{18}), respectively (Table 3A-1), if we assume that the hydrophobic alkenyl group ($C_{17}H_{33}$) of the surfactant **18** is equivalent to the saturated alkyl one ($C_{17}H_{35}$). Since the radius of core hydrophobic part (R_m) in a simple micelle (Figure 3A-1a) is approximately equal to l_{18} , R_m in **P18** is 2.3 nm. The thickness (R_o) of the outer hydrophilic layer of **P18** is calculated to be 2.2 nm by subtracting R_m (2.3 nm) from the hydrodynamic radius R (4.5 nm) determined experimentally by DLS (Figure 3-5). Based on the R_m (2.3 nm), the number of the surfactant **18** (N_{18}) in one micelle **P18** is calculated to be 106 by dividing the volume of the hydrophobic core by volume of the hydrophobic part of **18** (Eq. 3A-1).

$$N_{18} = 4\pi R_m^3 / 3v_{18} \dots\dots\dots(\text{Eq. 3A-1})$$

From the area of the hydrophobic sphere on **P18**, a_{18} is calculated to be 0.62 nm² according to Eq. 3A-2.

$$a_{18} = 4\pi R_m^2 / N_{18} \dots\dots\dots(\text{Eq. 3A-2})$$

Table 3A-1. Dimensions of structural elements for **P18** and **18/9₁₈**.

Micelle	mol % of 9₁₈ ^a	R_i^b / nm	R^c / nm	N_{18}^d	N_9^e	N_9 / N_{18} (%)
P18	0	0	4.5	106	0	0
18/9₁₈	11	0.4	4.86	143	16	11
	25	0.75	5.25	189	50	26
	43	1.35	5.85	270	122	45
	67	2.25	6.75	420	280	67
	100	3.5	8	682	600	88

^aBased on **18**. ^b $R_i = R - R_o - R_m$ (Figure 3-10b); R_o : Thickness of the outer hydrophilic layer of **P18**, R_m : Core hydrophobic part in **P18** or hydrophobic part in **18/9₁₈** and R_i : Inner hydrophilic part. ^c R is the experimental data determined by DLS. ^d N_{18} is the number of **18** per one mixed micelle. ^e N_9 is the number of **9₁₈** per one mixed micelle.

In the case of mixed micelles **18/9₁₈** containing 0 ~ 100 mol% of **9₁₈** shown in Table 3A-1, the thickness of the hydrophilic layer of the mixed micelle **18/9₁₈** is the same as that (R_o) in **P18** as shown in Figure 3A-1a and b. The thickness (R_o) of outer hydrophilic layer and the area (a_{18}) of outer hydrophilic-hydrophobic interface in **18/9₁₈** are assumed to be 2.2 nm and 0.62 nm², respectively. Therefore, the number (N_3) of surfactant **18** in **18/9₁₈** is calculated from the area a_{18} of the hydrophobic sphere determined by Eq. 3A-2, as shown in Eq. 3A-3.

$$N_{18} = 4\pi(R_m + R_i)^2 / a_{18} \dots\dots\dots(\text{Eq. 3A-3})$$

The total volume occupied by surfactant **18** in the hydrophobic layer (v_{18}) in one micelle of **18/9₁₈** is calculated to be $N_{18} \times v_{18}$. If the rest of the volume in the hydrophobic layer is fully occupied by hydrophobic part of **9₁₈** ($n = 18$, $v_9 = 0.51$ nm³), the number (N_9) of **9₁₈** can be determined by Eq. 3A-4.

$$N_9 = (4/3 \times \pi(R_m + R_i)^3 - 4/3 \times \pi R_i^3 - N_{18} \times v_{18}) / v_9 \dots\dots\dots(\text{Eq. 3A-4})$$

The results are summarized in Table 3A-1. The mol% of **9₁₈** calculated as N_9 / N_{18} (%) is matched with that used for the preparation of the mixed micelles **18/9₁₈**. In addition, Joshua et al. reported that a water penetration occurs between the hydrophobic alkyl chains in micelles [95]. These secure the validity of the structure of **18/9₁₈** with water molecules in the central core (Figure 3A-1b).

Another possible structure of **18/9₁₈** is shown in Figure 3A-1c. Based on our calculations described above, the mixed micelle **18/9₁₈** possesses a low density core, which is occupied by alkyl

chains of **9**₁₈. In addition, the fact that the time scale of D_x and D_y of **9**₁₈ in the mixed micelles were evaluated to be less than $2 \times 10^{-6} \text{ s}^{-1}$ indicates that **9**₁₈ can change its position and reach the outer hydrophilic part of the mixed micelles many times during 1 sec. Because of this phenomenon, the nitroxyl groups in **9**₁₈ are able to interact with surrounding water molecules, giving a significant enhancement of proton relaxation. By considering the results discussed above, the structure of **18/9**₁₈ with a low density core may be possible, too. The accurate structure of the mixed micelle **18/9**₁₈ will be determined by transmission electron microscopic (TEM) or SANS analyses. The detailed discussion will be described in forthcoming paper.

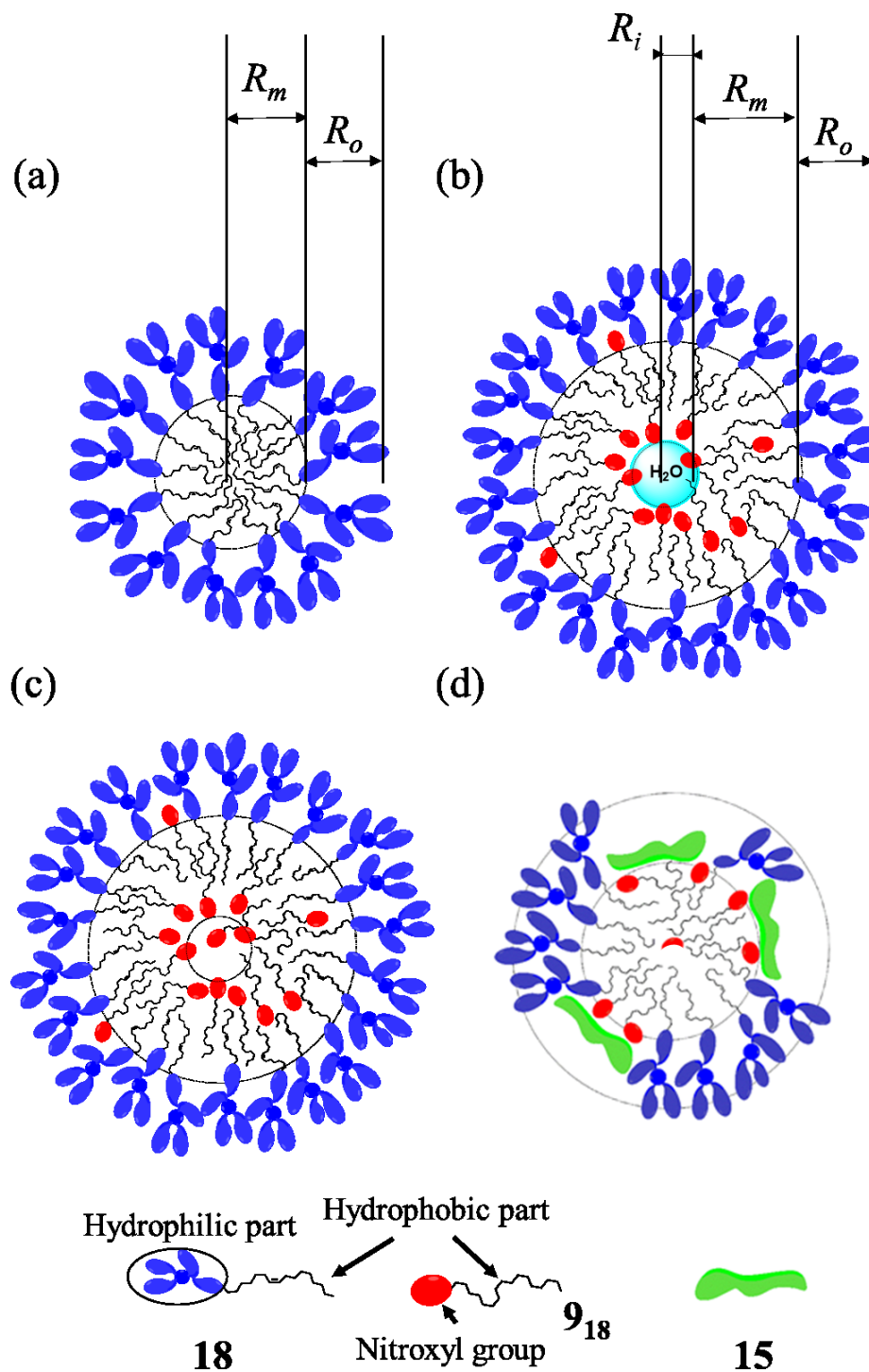


Figure 3A-1. Micelle structure of (a) P18 (pure micelle of 18). Newly proposed mixed micelle structures of 18/9₁₈ (b) without or (c) with water molecules in the core, and (d) 18/9₁₈/15.

The mean diameters of $18/9_{18}/15$ was smaller than that of $18/9_{18}$ due to the existence of **15** which has both hydrophilic functional groups, such as R-OH, R-C(O)-OR' and R-C(O)-NH-R', and hydrophobic phenyl moieties. Obviously, **15** can localize in the interface between hydrophobic and hydrophilic regions as shown in Figure 3A-1d. In addition, as shown in Figure 3-5b, the particle diameter should depend on the number of molecule. Thus, the cross-section area (a) diminishes as with decreasing number of the constituents in the presence of **15**, so that the size of the equilibrium micelles diminishes according to Eq. 3A-3.

3-5-2. Results of EPR spectral simulation

Spectral simulations for the extraction of the quantitative data on molecular mobility were performed using the handmade program developed by Prof. Vorobiev (see the experimental section for details). A convolution of Gaussian and Lorentzian functions, as the most general representation of individual EPR line shapes, was used for simulation. The program allows to take into account the dependence of a line shape on the orientation of the species in a magnetic field that reflects line broadening as a result of an unresolved anisotropic hyperfine interaction. Additionally, the EPR line shape is given by a tensor, principal axes of which generally do not coincide with principal axes of the g -tensor.

The g factor and hyperfine coupling constant A of the paramagnetic species are described as tensors. In this work, the three principal g -tensor axes were chosen as axes of coordinates; their directions in molecules of nitroxide radicals are shown in Figure 3A-2 [96].

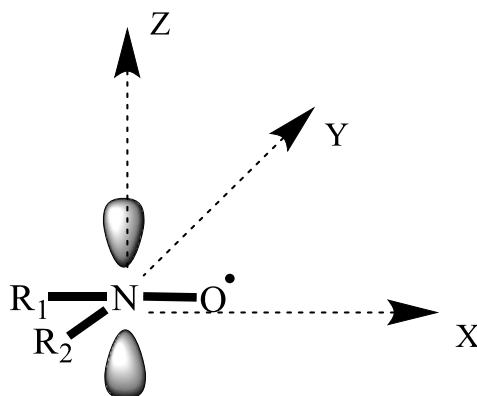


Figure 3A-2. The directions of the three principal g -tensor axes in molecules of nitroxide radicals.

Generally, nine components of the g tensor in the laboratory frame are represented by a square matrix of 3 rows \times 3 columns. Therefore, the diagonal matrix with only the principal values (g_{xx} , g_{yy} , g_{zz}) can be obtained by performing the transformation to diagonalize the matrix in the laboratory.

$$\tilde{g} = \begin{pmatrix} g_{xx} & g_{xy} & g_{xz} \\ g_{yx} & g_{yy} & g_{yz} \\ g_{zx} & g_{zy} & g_{zz} \end{pmatrix} \xrightarrow{\text{Transformation}} \begin{pmatrix} g_{XX} & 0 & 0 \\ 0 & g_{YY} & 0 \\ 0 & 0 & g_{ZZ} \end{pmatrix}$$

Laboratory frame Principal frame

However, the principal axes of g - and A -tensors do not generally coincide with each other and their relative orientation is given by the diffusion tilt angles (alpha, beta, gamma), called Euler angles, connecting the molecular orientation frame with the g -tensor frame [97]. The angles can connect the magnetic axes with those of the rotational diffusion tensor. The rotation is achieved by the following series of mathematical operations (Figure 3A-3) : (i) a rotation about X through the angle alpha which is described in equation 3A-5 (shown in Figure 3A-3a); (ii) a rotation about Y through the angle beta after the rotation about X, which is described in equation 3A-6 (shown in Figure 3A-3b when alpha = 0); (iii) a rotation about Z through the angle gamma after the rotation about X and Y, which is described in equation 3A-7 (shown in Figure 3A-3c when alpha and beta = 0) [93]. Note that a positive angle gives a counterclockwise rotation when viewed along the axis of rotation looking from the positive side [93].

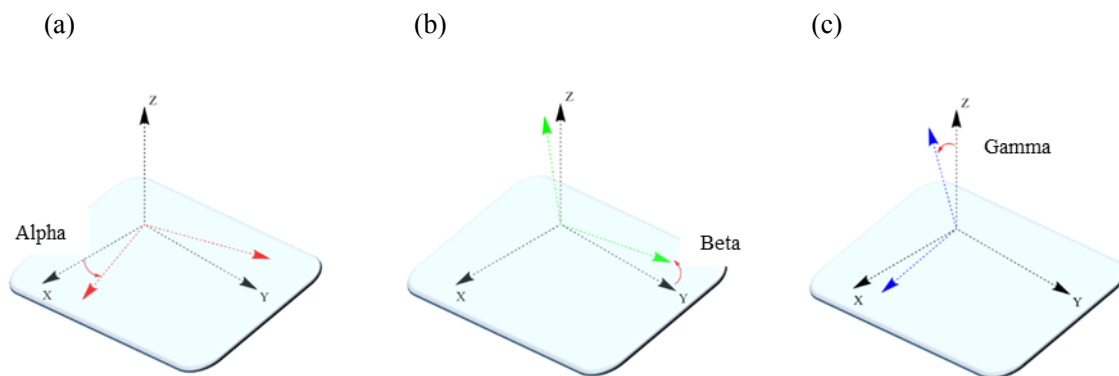


Figure 3A-3. Rotating operation about principal axes through the Euler angles. (a) rotation about X through the angle alpha, (b) rotation about Y through the angle beta when alpha = 0 and (c) rotation about Z through the angle gamma when alpha = 0 and beta = 0

$$C = \begin{pmatrix} \cos(\alpha) & \sin(\alpha) & 0 \\ -\sin(\alpha) & \cos(\alpha) & 0 \\ 0 & 0 & 1 \end{pmatrix} \dots\dots\dots \text{Eq. 3A-5}$$

$$B = \begin{pmatrix} 1 & 0 & 0 \\ 0 & \cos(\beta) & \sin(\beta) \\ 0 & -\sin(\beta) & \cos(\beta) \end{pmatrix} \dots\dots\dots \text{Eq. 3A-6}$$

$$A = \begin{pmatrix} \cos(\gamma) & \sin(\gamma) & 0 \\ -\sin(\gamma) & \cos(\gamma) & 0 \\ 0 & 0 & 1 \end{pmatrix} \dots\dots\dots \text{Eq. 3A-7}$$

The operations described above can be summarized as follows;

$$\begin{pmatrix} \vec{e}_X \\ \vec{e}_Y \\ \vec{e}_Z \end{pmatrix} = ABC \begin{pmatrix} \vec{e}_{X'} \\ \vec{e}_{Y'} \\ \vec{e}_{Z'} \end{pmatrix}, \text{ where } \begin{pmatrix} \vec{e}_{X'} \\ \vec{e}_{Y'} \\ \vec{e}_{Z'} \end{pmatrix} \text{ shows the standard basis after the translation.}$$

In Table 3A-2, the author shows the preparation conditions of the mixed micelles used for the EPR simulation in the chapter 3. The author prepared the mixed micelles containing 0.10 mM or 0.25 mM of $\mathbf{9}_{18}$ for both $\mathbf{6/9}_{18}$ and $\mathbf{18/9}_{18}$ to investigate the effect of radicals' concentration on their mobility in the mixed micelles.

Table 3A-2. Preparation conditions of $\mathbf{6/9}_{18}$ or $\mathbf{18/9}_{18}$.

Mixed micelle	$\mathbf{18/9}_{18}$ with a molar ratio of 1 : 0.01 ^a	$\mathbf{18/9}_{18}$ with a molar ratio of 1 : 0.02	$\mathbf{6/9}_{18}$ with a molar ratio of 1 : 0.01 ^a	$\mathbf{6/9}_{18}$ with a molar ratio of 1 : 0.02

^a These results are described above.

The slow-motion EPR spectra including the information about the dynamic parameters such as D_z are fitted by least-squares method using model calculation based on the stochastic Liouville equation for the experimental data. In this work, at first, the separation of magnetic parameters such as g -tensor was conducted to decrease the fitting parameters required for slow-motion EPR spectral simulation. The magnetic parameters were extracted from rigid-limit EPR spectra to obtain the reliable values. The EPR absorption line of the disordered sample was described using the function of Eq. 3A-8 [92]. $F(H) = \frac{1}{4\pi} \int_0^{2\pi} d\varphi \int_0^\pi f(H, g, A, \theta, \varphi) d\varphi$ Eq. 3A-8 where θ and φ are magnetic field directions in the frame of paramagnetic species. $f(H, g, A, \theta, \varphi)$ describes the individual resonance line; magnetic parameters such as g and A values show the position of the absorption line.

All magnetic parameters extracted from rigid-limit EPR spectra were summarized in Table 3A-3. The resulting discrepancy was calculated as follows:

$$\text{discrepancy} = \frac{1}{2} \sum_i \frac{r_i^2}{n},$$

where r_i and n are the minimized residuals and the number of calculated points in the spectrum, respectively.

Table 3A-3. Magnetic parameters obtained from rigid-limit EPR spectrum recorded at 100 K.

Mixed micelles	g_x	g_y	g_z	A_x / G	A_y / G	A_z / G	Discrepancy ($\times 10^{-9}$)
18/9 ₁₈ (1 : 0.01)	2.0089	2.0065	2.0025	3.298	4.438	34.51	0.189
18/9 ₁₈ (1 : 0.02)	2.0092	2.0060	2.0027	3.095	5.401	34.73	0.171
6/9 ₁₈ (1 : 0.01)	2.0088	2.0065	2.0025	3.947	4.371	35.05	0.105
6/9 ₁₈ (1 : 0.02)	2.0092	2.0061	2.0026	2.978	4.238	35.65	0.070

Rigid-limit EPR spectra of **18/9**₁₈ with a molar ratio of 1 : 0.02, **6/9**₁₈ with a molar ratio of 1 : 0.01 and **6/9**₁₈ with a molar ratio of 1 : 0.02, and the results of their computer simulation are shown in Figure 3A-4.

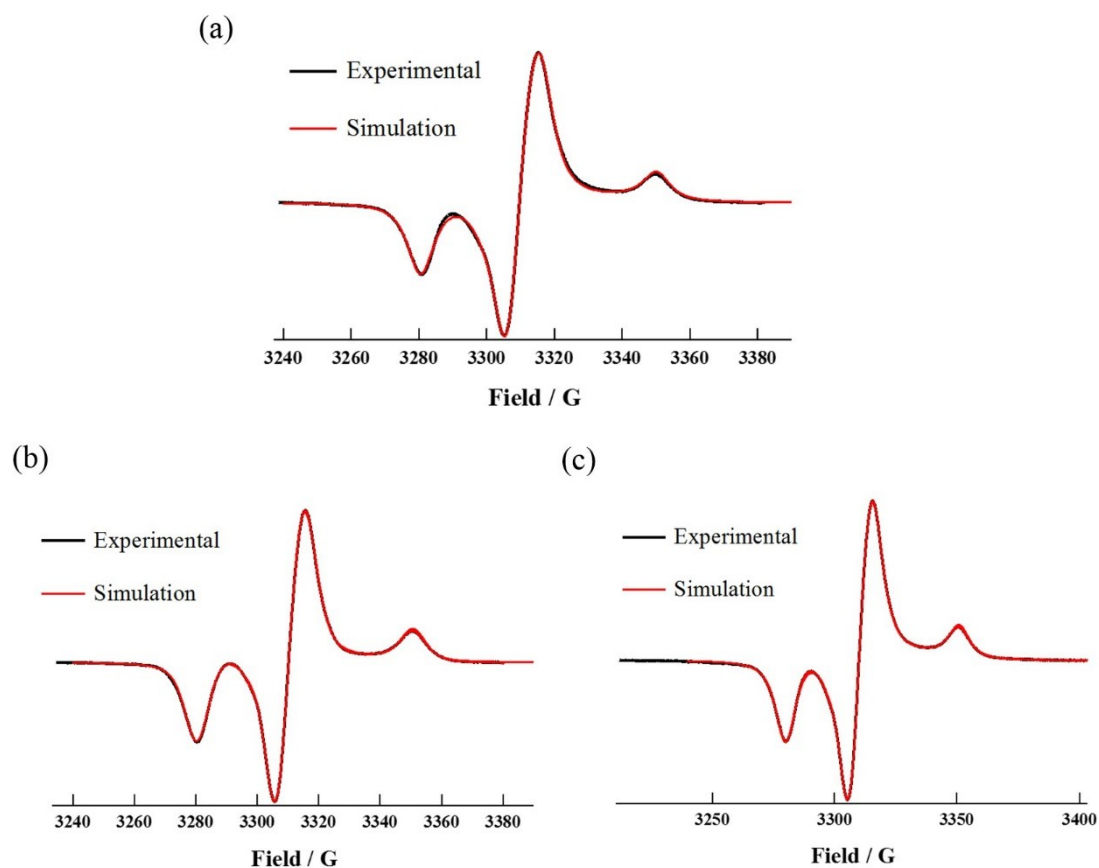


Figure 3A-4. EPR spectra of (a) **18/9**₁₈ with a molar ratio of 1 : 0.02, (b) **6/9**₁₈ with a molar ratio of 1 : 0.01 and (c) **6/9**₁₈ with a molar ratio of 1 : 0.02 and the results of their computer simulation at 100 K. Black lines – experimental spectra, red lines – results of simulation. See the experimental section for details.

In general, sufficient information concerning not only magnetic parameters but also dynamic parameters are required to simulate the slow-motion EPR spectra. To avoid this problem, the author simulated the slow-motion EPR spectra (263 K - 298 K) of each mixed micelles by using the magnetic parameters determined at 100 K (Table 3A-3). These mathematical operation makes it possible to obtain the dynamic parameters such as rotational diffusion tensor by solving the stochastic Liouville equation [93]. In this work, the order of D_x and D_y ($2 \times 10^6 \text{ s}^{-1}$ each) was in the limit of sensitivity for EPR spectra of nitroxide radicals, so that the author simulated the EPR spectra with imposing the constraint ($D_x = D_y$) and without varying these values to extract the reliable results in the range of this order. The simulational results of **18/9**₁₈ (1 : 0.02) and **6/9**₁₈ (1 : 0.02) were summarized in Table 3A-4. D_z ($\times 10^8 \text{ Hz}$) denotes the diffusion coefficient for rotation around Z axis the representative results for simulation of several spectra are presented in Figures 3A-5, 3A-6 and 3A-7.

Table 3A-4. Rotation diffusion coefficients and the angles determining the position of the main rotation axis in g-tensor frame for radical **9**₁₈ in **18/9**₁₈ (1 : 0.02) and **6/9**₁₈ (1 : 0.02).

Temp., K	18/9 ₁₈			6/9 ₁₈		
	$D_z, 10^8 \text{ s}^{-1}$	Beta ^a , °	Gamma ^a , °	$D_z, 10^8 \text{ s}^{-1}$	Beta ^a , °	Gamma ^a , °
298	6.62	53.0	60.4	6.58	52.9	61.3
293	5.70	52.5	60.4	5.85	52.1	59.7
288	5.15	51.7	60.4			
283	4.68	50.8	60.8	4.78	50.4	59.8
281	4.47	50.6	63.4	4.56	50.1	62.9
279	4.19	50.2	62.6	4.55	49.7	61.8
277	4.01	49.6	64.4	4.14	49.3	62.3
275	3.84	49.2	65.5	4.03	48.6	63.4
273	3.51	49.1	64.6	3.82	48.3	62.2
271	3.17	48.9	67.6	3.56	47.8	64.9
269	3.05	48.6	68.4	3.39	47.2	58.8
267	2.80	48.5	70.1	3.09	46.6	58.3
265	2.56	48.1	76.3	2.74	46.3	58.2
263	2.49	47.3	70.9	2.26	45.5	58.4

^aEuler angles describe the transformation of rotation frame to g-tensor frame.

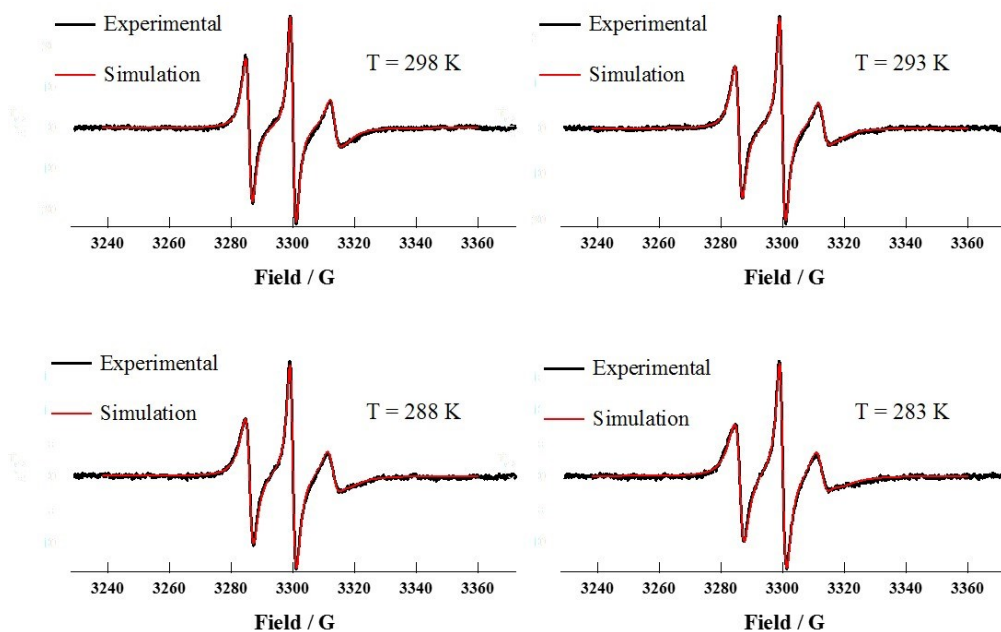


Figure 3A-5. Representative EPR spectra of $18/9_{18}$ (a molar ratio of 1 : 0.02) and the results of their computer simulation at high temperatures. Black lines denote the experimental spectra, red lines represent the results of simulation.

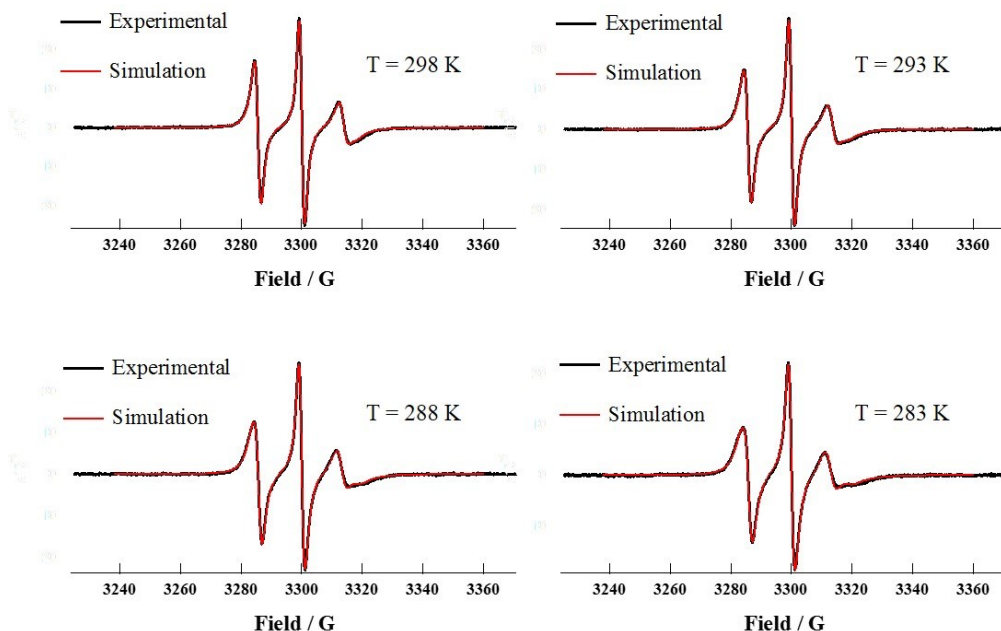


Figure 3A-6. Representative EPR spectra of $6/9_{18}$ (a molar ratio of 1 : 0.01) and the results of their computer simulation at high temperatures. Black lines denote the experimental spectra, red lines represent the results of simulation.

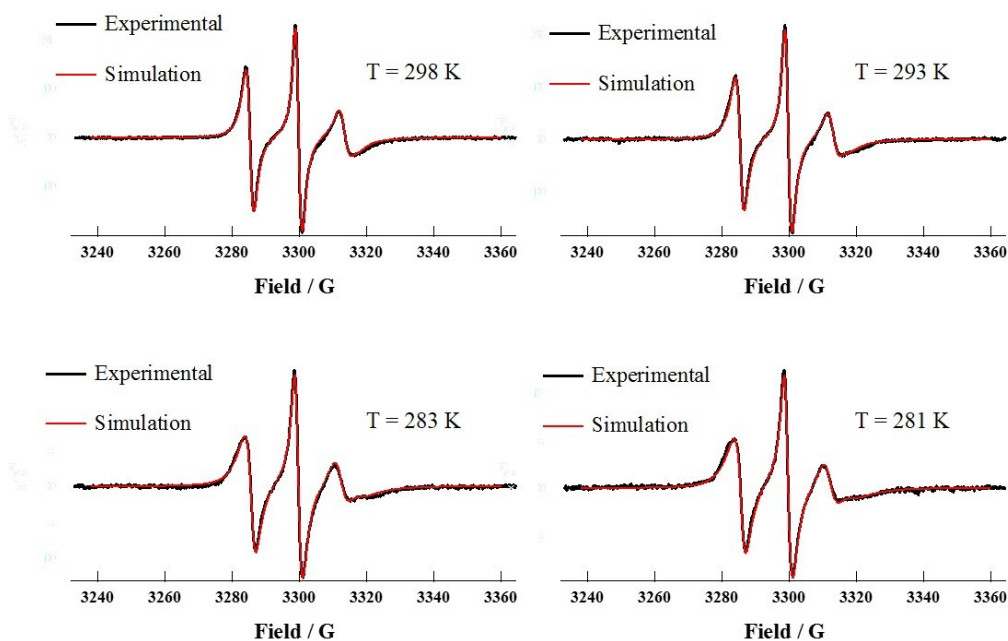


Figure 3A-7. Representative EPR spectra of $6/9_{18}$ (a molar ratio of 1 : 0.02) and the results of their computer simulation at high temperatures. Black lines denote the experimental spectra, red lines represent the results of simulation.

Arrhenius plot for D_z values of the mixed micelles are created by using the simulation results in Tables 3-2 and 3A-4 (Figure 3A-8).

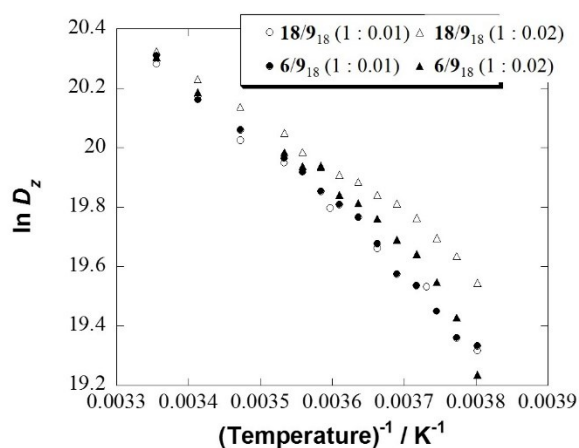


Figure 3A-8. Temperature dependence of rotation diffusion coefficient D_z of 9_{18} in $6/9_{18}$ and $18/9_{18}$ with the ratio of 1 : 0.01, and $6/9_{18}$ and $18/9_{18}$ with the ratio of 1 : 0.02. See the experimental section for details.

The linear regression analysis yielded the E_z values of each mixed micelle. Furthermore, D_z values at 273 K were evaluated from the linear equation (Table 3A-5).

Table 3A-5. D_z at 273 K and E_z^a values of $\mathbf{9}_{18}$ in $\mathbf{6/9}_{18}$ and $\mathbf{18/9}_{18}$ with the ratio of 1 : 0.01, and $\mathbf{6/9}_{18}$ and $\mathbf{18/9}_{18}$ with the ratio of 1 : 0.02.

Mixed micelle	$\mathbf{18/9}_{18}$ with a molar ratio of 1 : 0.01 ^a	$\mathbf{18/9}_{18}$ with a molar ratio of 1 : 0.02	$\mathbf{6/9}_{18}$ with a molar ratio of 1 : 0.01 ^a	$\mathbf{6/9}_{18}$ with a molar ratio of 1 : 0.02
D_z / s^{-1}	3.5 ± 0.9	3.7 ± 1.2	4.2 ± 0.9	4.7 ± 3.1
$E_z^a / \text{kJ/mol}$	18.4 ± 0.4	18.4 ± 0.6	17.8 ± 1.2	13.7 ± 0.4

^a These results are described above.

According to Figure 3A-8, one can see the difference in temperature-dependence of D_z values between two different concentrations of $\mathbf{9}_{18}$ in the $\mathbf{18/9}_{18}$; $\mathbf{9}_{18}$ in $\mathbf{18/9}_{18}$ (1 : 0.01) showed smaller rotational diffusion than that in $\mathbf{18/9}_{18}$ (1 : 0.02). This result indicates the mobility of $\mathbf{9}_{18}$ in $\mathbf{18/9}_{18}$ increased with increasing the concentration of $\mathbf{9}_{18}$ of in the $\mathbf{18/9}_{18}$. In contrast, there is no difference in the rotational diffusion of $\mathbf{9}_{18}$ when comparing the D_z values of $\mathbf{9}_{18}$ in $\mathbf{6/9}_{18}$ (1 : 0.01) and $\mathbf{6/9}_{18}$ (1 : 0.02).

3-5-3. TEM study of $\mathbf{18/9}_{18}$ (40 mM each)

To get an insight into a micellar structure, $\mathbf{18/9}_{18}$ (40 mM) was analyzed with transmission electron microscopy (TEM). Since we could not observe the nanoparticles clearly at a concentration of 10 mM as the author expected, the higher concentration (40 mM) of $\mathbf{18/9}_{18}$ or $\mathbf{P18}$ in PBS was chosen to the TEM analysis. As a result, $\mathbf{18/9}_{18}$ were distinctly observed in the blackish nanoparticles as shown in Figure 3A-9a–e, indicating that $\mathbf{18/9}_{18}$ had highly packed hydrophobic layers due to the van der Waals interactions between alkyl chains in $\mathbf{18}$ and $\mathbf{9}_{18}$. In contrast, it seems that there is a gap in the hydrophobic parts of $\mathbf{P18}$ (Figure 3A-9f–j). Therefore, $\mathbf{9}_{18}$ is considered to make the micelles more rigid possibly by the increased hydrophobic interaction.

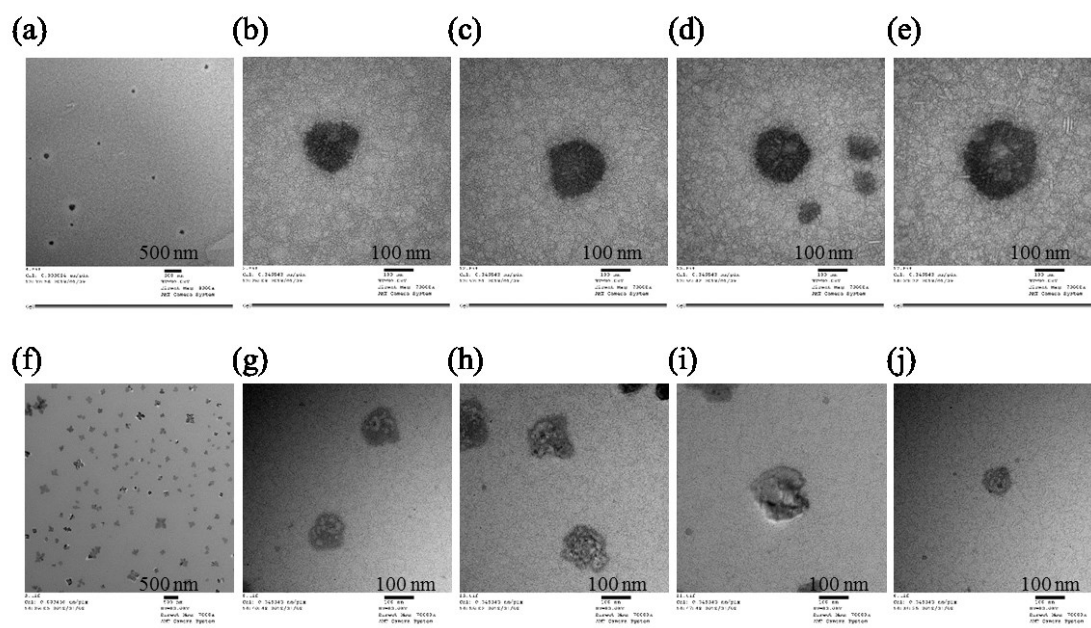


Figure 3A-9. Typical TEM images (120 kV, 25 °C) of (a–e) **18/9₁₈** (40 mM) and (f–j) **P18** (40 mM) in PBS. Panels b–e and g–j are the enlarged images of panels a and f, respectively.

4-1. Introduction

Non-invasive imaging of living tissue is of great importance in the medical field. A magnetic resonance imaging (MRI) method is one of the most frequently used and important imaging techniques in clinical medicine. In fact, the use of MRI contrast agents plays a crucial role in accurately evaluating the physiologic and pathologic changes. The majority of FDA-approved MRI contrast agents are gadolinium-based contrast agents (GBCAs) such as Magnevist (a Gd^{III} complex agent) [98,99,100]. Although they are used on a daily basis, this modality still faces many challenges [101,102,103,104]. For example, people with moderate to advanced kidney failure are in danger of developing nephrogenic systemic fibrosis by use of GBCAs. Thus, it is urgently required to exploit novel agents that exhibit adequate contrast enhancement with a very low risk.

Metal-free magnetic nanoparticles containing nitroxide radicals as a spin source have attracted great interest since 1980s [105] because of no toxicity, despite the less imaging ability as compared to Gd^{III} complex agents [106] and less reduction resistance to antioxidants such as ascorbic acid and glutathione [107]. However, the reduction resistance should potentially improve through the molecular design and/or the micelle construction of nitroxide radicals [83,84,85,86,87]. In this context, we have recently prepared a metal-free magnetic mixed micelles comprised of a surfactant, Brij 58 (**6**) or Tweens 80 (**18**), and pyrrolidine-*N*-oxyl radical **9**, namely **6/9** or **18/9** (Figure 4-1), according to a simple experimental procedure as described in the chapter 2 and 3. These micelles showed high colloidal stability, reduction resistance to ascorbic acid, and contrast enhancement in the T_1 -weighted MRI in PBS *in vitro* and *in vivo*. The mixed micelle **18/9** was found to be much less toxic than **6/9**. Furthermore, additional hydrophobic fluorophores or drugs were stably encapsulated inside the mixed micelles. Although passive targeting can be expected due to the micelle size (10 - 20 nm), the micelles which we prepared did not possess any active targeting site for tumor.

Herein, we report on the novel metal-free mixed micelles including nitroxide radicals **20_n**, conjugated with a D-glucosamine unit as a tumor targeting site, because D-glucosamine derivatives are well-known to be accumulated in tumor cells [108,109,110,111]. The obtained magnetic mixed micelles showed little toxicity, excellent *in vitro* MRI contrast ability and high stability in the presence of an excess amount of ascorbic acid. When it is applied to *in vivo* imaging for healthy mice, bright MRI contrast enhancement was observed in the liver.

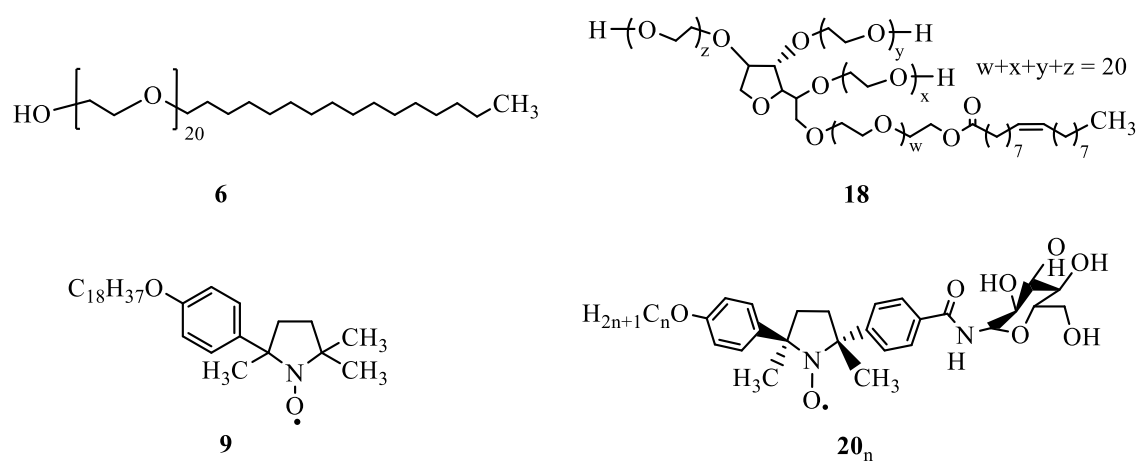


Figure 4-1. Molecular structures of non-ionic surfactants Brij 58 (**6**) and Tween 80 (**18**), and nitroxide radicals **9** and **20_n** ($n = 14, 16$ and 18). Compounds **20_n** are a ca. 1:1 mixture of D-(*R,R*) and D-(*S,S*) diastereomers, see the experimental section for the synthesis and characterization.

4-2. Results and Discussion








4-2-1. Preparation, stability and *in vitro* MRI contrast ability of $18/20_n$

The nitroxide radicals 20_n ($n = 14, 16$ and 18 in Figure 4-1) were synthesized by condensation of the racemic benzoic acid derivatives of the nitroxide radicals [a 1:1 mixture of (*R,R*) and (*S,S*) enantiomers] [112,113] and D-tetraacetylglucosamine [114,115,116] followed by deacetylation (see the experimental section).

The mixed micelles $18/20_n$ (Figure 4-1) were prepared at concentration of 10 mM for each component in PBS according to the procedure described in the experimental section. The stability of the micelles was found to depend on the length of the alkyl chain ($n = 14, 16$ and 18) in the radicals 20_n (Table 4-1 and Figure 4-2). $18/20_{16}$ and $18/20_{18}$ were formed as a clear dispersion immediately after preparation and their mean diameter gradually increased up to 92 and 45 nm after one week, respectively (Table 4-1). The micelle $18/20_{14}$ collapsed within one day to give white precipitates of 20_{14} after 24 h. From these results summarized in Table 4-1, the relative stability of the micelles $18/20_n$ in PBS is in the following order; $18/20_{18} > 18/20_{16} > 18/20_{14}$. Similar dependence of the micellar stability on the alkyl chain length in the nitroxide radicals 20_n was observed in the cases of the mixed micelles $6/9$ and $18/9$, too [chapter 2 and 3]. The mean diameters of the resulting magnetic mixed micelles $18/20_n$ in PBS were determined to be 13 to 16 nm by DLS analysis (Table 4-1 and Figure 4-2a). Their mean diameters fall in a range of 10 to 100 nm which is required for the most prolonged blood circulation time.

Importantly, the once precipitated sample of $18/20_{14}$ revived to the original clear dispersion having the same diameter (16 nm) by just heating it with full reproducibility (Table 4-1); the micelle $18/20_{14}$ turned out to be easily available as a clear dispersion even after long-term preservation of the precipitated sample.

Table 4-1. Mean diameters and colloidal stability of the mixed micelles **18/20_n** ($n = 14, 16$ and 18) in PBS at 30 °C.

Micelle	18/20₁₄	18/20₁₆	18/20₁₈
Diameter by DLS	16 nm ^a	13 nm ^a 92 nm ^c	14 nm ^a 45 nm ^c
Colloidal stability	dispersion ^a  precipitates ^b  dispersion ^d 	dispersion ^a  dispersion ^c 	dispersion ^a  dispersion ^c 

^aImmediately after preparation. ^bAfter 24 h from preparation. ^cAfter 6 days from preparation. ^dAfter heating the precipitates.

In the EPR spectra of **18/20_n** shown in Figure 4-2b, c and d, the broad singlet signals were obtained immediately after preparation due to the Heisenberg spin exchange interactions.

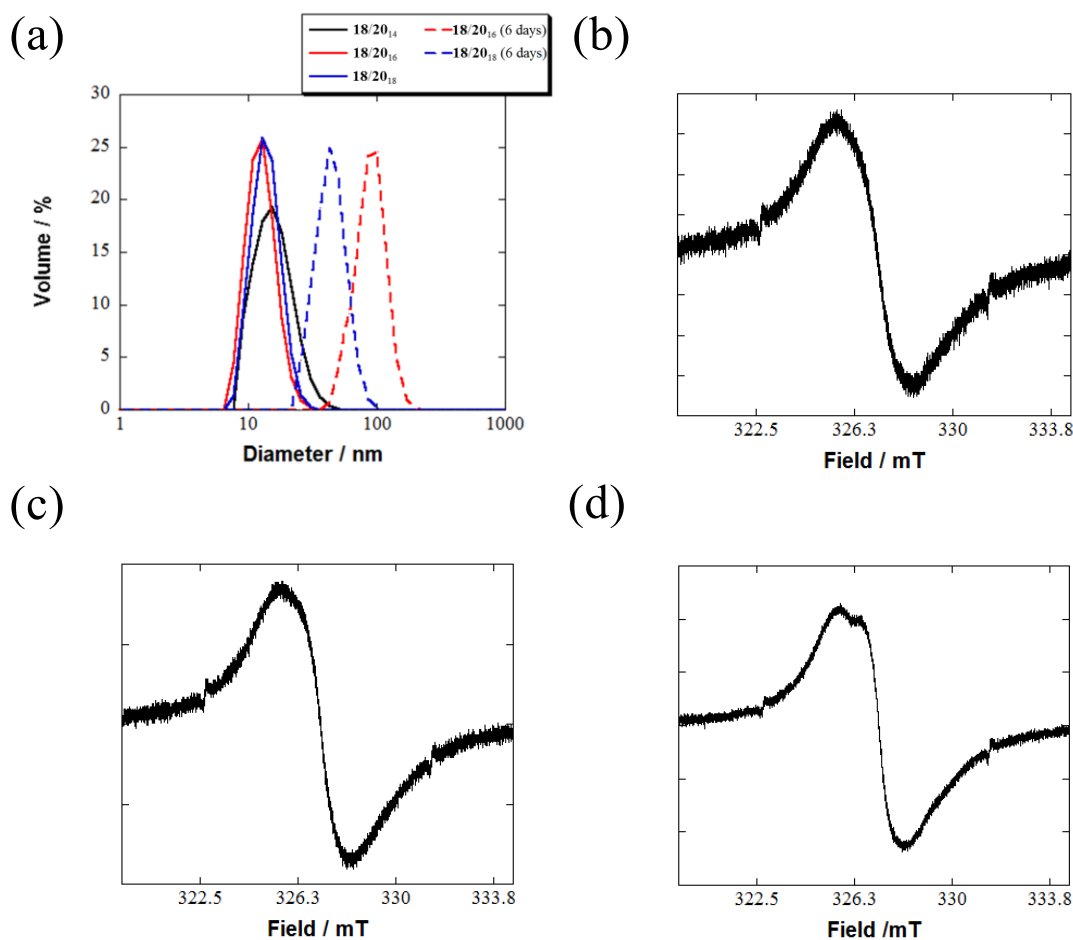


Figure 4-2. (a) Mean diameters of mixed micelles $18/20_n$ ($n = 14, 16$ and 18) determined by DLS (black solid line: $18/20_{14}$ just after preparation, red solid line: $18/20_{16}$ just after preparation, blue solid line: $18/20_{18}$ just after preparation, red dashed line: $18/20_{16}$ after 6 days, blue dashed line: $18/20_{18}$ after 6 days) and EPR spectra of (b) $18/20_{14}$, (c) $18/20_{16}$ and (d) $18/20_{18}$ at 25°C in PBS.

The dependence of the alkyl chain length in 20_n on the longitudinal relaxivity (r_1) of $18/20_n$ was determined from the relaxation time (T_1) as a function of the concentration at 25°C by using an MRI machine at 7.0 T. Sufficiently bright T_1 -weighted MR phantom images were obtained at concentration of 10 mM of the magnetic mixed micelles $18/20_{14}$, $18/20_{16}$ and $18/20_{18}$ as compared with that of control PBS (panel A, E and I in Figure 4-3a). This result implies that $18/20_n$ is likely to show a distinct MRI contrast enhancement *in vivo* in this concentration or higher. Linear regression analysis yielded $r_1 = 0.14, 0.13$ and $0.11 \text{ mM}^{-1}\text{s}^{-1}$ for $18/20_{14}$, $18/20_{16}$ and $18/20_{18}$, respectively (Figure 4-3b). That is, the MRI contrast ability of the micelle $18/20_n$ in PBS is in the following order; $18/20_{14} > 18/20_{16} > 18/20_{18}$. The mixed micelle $18/20_{14}$ was used for further experiments in the following two reasons; (1) $18/20_{14}$ exhibited the superior *in vitro* MRI enhanced ability to those of $18/20_{16}$ and $18/20_{18}$ and (2) the clear dispersion was fully revived reproducibly by simply heating the precipitated sample. Although

stability of $\mathbf{18/20}_{14}$ was less than that of $\mathbf{18/20}_{16}$ and $\mathbf{18/20}_{18}$ as mentioned above (Table 4-1), we gave priority to MRI enhanced ability over the stability.

These r_1 values are much larger than those of micelles $\mathbf{18/9}$ and $\mathbf{6/9}$ ($r_1 = 0.07$, and $0.09 \text{ mM}^{-1}\text{s}^{-1}$, respectively, at 7.0 T) which we reported previously, although they are much lower than those of Gd^{III} complex agents [103].

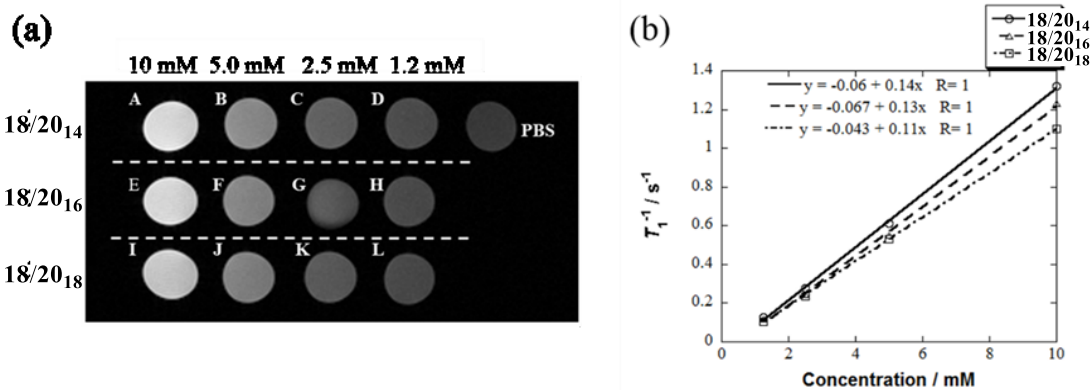


Figure 4-3. (a) (A – D) T_1 -weighted MR phantom images of $\mathbf{18/20}_{14}$ ($\mathbf{20}_{14}$: 1.2 to 10 mM), (E – H) $\mathbf{18/20}_{16}$ ($\mathbf{20}_{16}$: 1.2 to 10 mM) and (I – L) $\mathbf{18/20}_{18}$ ($\mathbf{20}_{18}$: 1.2 to 10 mM) in PBS, and control PBS at 7.0 T and 25 °C. (b) Plots of T_1^{-1} vs concentrations of $\mathbf{18/20}_{14}$ (solid line), $\mathbf{18/20}_{16}$ (dashed line) and $\mathbf{18/20}_{18}$ (dashed and dotted line) at 1.2, 2.5, 5.0, 10 mM for each component. The r_1 was determined from the slope of each line. See the experimental section for details.

These experimental results can be interpreted in terms of the slower rotation diffusion of $\mathbf{20}_{14}$ than that of $\mathbf{9}$ inside the mixed micelles [89,90,91]. In order to compare the rotation diffusion mobility between radicals $\mathbf{20}_{14}$ and $\mathbf{9}$ inside the micelles, the EPR spectra of radical $\mathbf{20}_{14}$ or $\mathbf{9}$ in the micelles consisting of a 1 : 0.01 molar ratio of surfactant $\mathbf{18}$ and $\mathbf{20}_{14}$ or $\mathbf{9}$ were measured in the temperature range from 263 to 298 K and then were numerically simulated (Table 4-2). The representative results for simulation of several spectra are presented in Figure 4-4 and 4-5.

Table 4-2. Rotation diffusion coefficients and the angles determining the position of the main rotation

axis in *g*-tensor frame for radical **20**₁₄ in **18/20**₁₄ (a molar ratio of 1 : 0.01).

Temp., K	$D_z, 10^8 \text{ s}^{-1}$	Beta ^a , ° (±2°) ^b	Gamma ^a , ° (±2°) ^b	Discrepancy (× 10 ⁻⁷)
298	3.6 ± 0.5 ^b	45	75	0.741
293	3.3 ± 0.5	45	73	0.363
288	2.9 ± 0.4	44	90	0.333
283	2.5 ± 0.4	43	90	0.414
281	2.3 ± 0.3	43	90	0.202
279	2.2 ± 0.3	42	90	0.409
277	2.1 ± 0.3	41	90	0.170
275	1.8 ± 0.3	42	90	0.157
273	1.8 ± 0.3	41	90	0.158
271	1.9 ± 0.3	38	90	0.213
269	1.4 ± 0.2	40	90	0.110
267	1.4 ± 0.2	39	90	0.165
265	1.2 ± 0.2	37	90	0.249
263	1.2 ± 0.2	36	90	0.115

^aEuler angles describe the transformation of rotation frame to *g*-tensor frame [96,97]. ^bError values are presented.

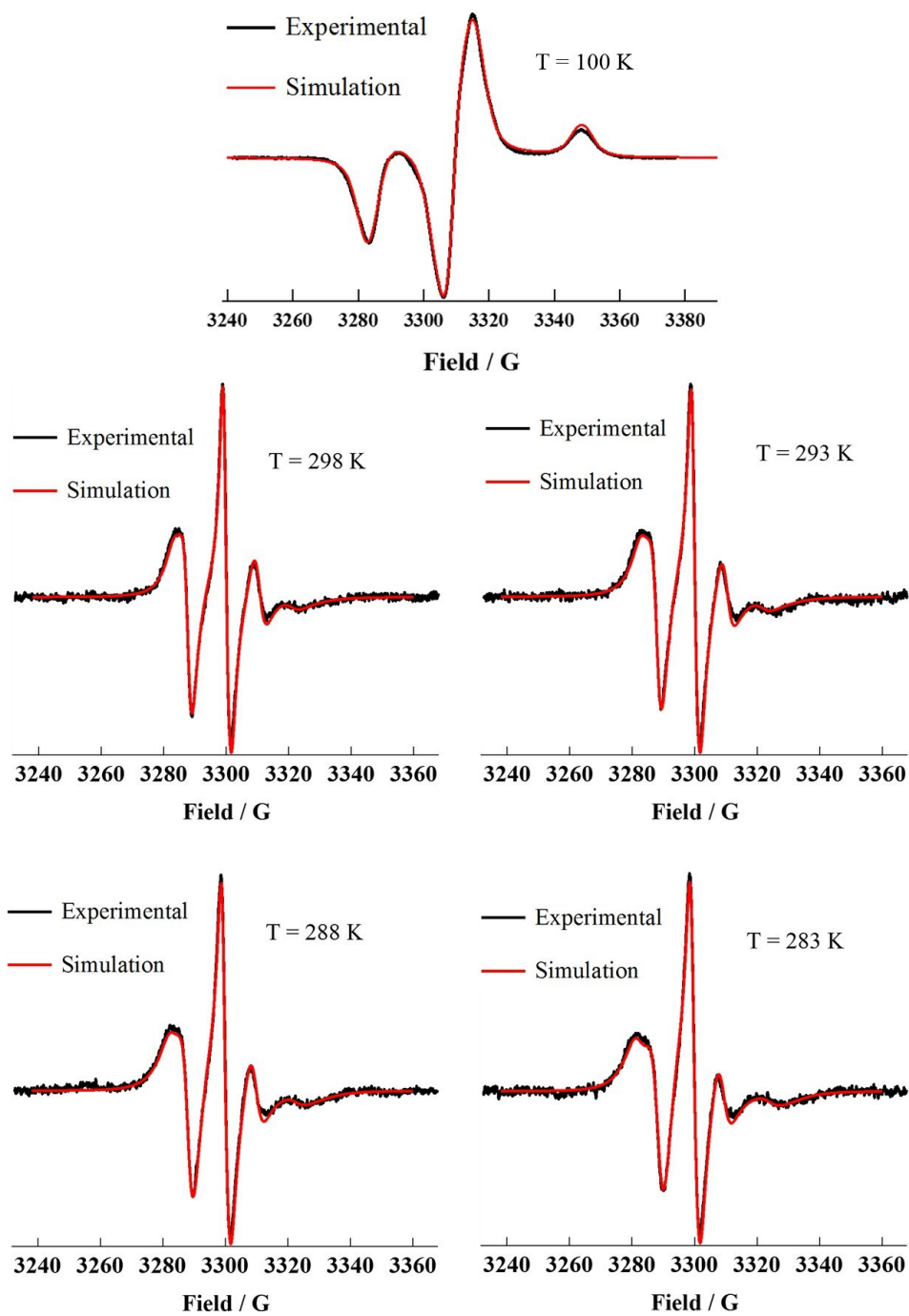


Figure 4-4. Representative EPR spectra of $18/20_{14}$ (a molar ratio of 1 : 0.01) and the results of their computer simulation at high temperatures. Black lines denote the experimental spectra, red lines represent the results of simulation.

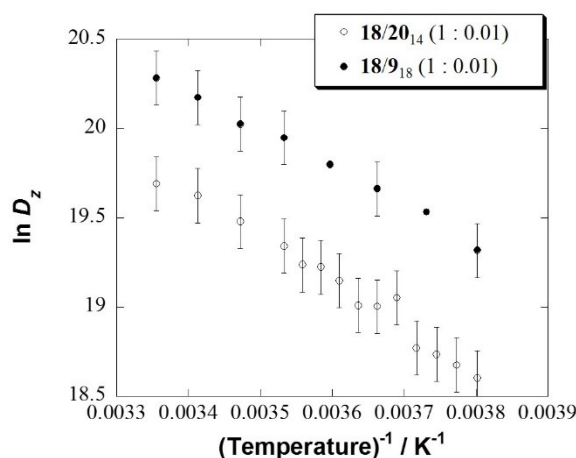


Figure 4-5. Temperature dependence of rotation diffusion coefficient D_z of 20_{14} in $18/20_{14}$ and 9 in $18/9$. The data of $18/9$ was cited from the chapter 3. See the experimental section for details of $18/20_{14}$.

The temperature dependence of the rotation diffusion mobility was successfully described by Arrhenius law with values of activation energy (E_z^a) shown in Table 4-3, indicating that 4_{14} showed slower rotational diffusion inside the micelle to give a highly enhanced MRI as compared with 3 . The better r_1 of $18/20_{14}$ than $18/20_{16}$ and $18/20_{18}$ mentioned above might be interpreted by the slower rotation diffusion mobility of 20_{14} than 20_{16} and 20_{18} .

Table 4-3. The effective activation energy of rotation diffusion of 20_{14} in $18/20_{14}$ and 9 in $18/9$.

Mixed micelle	E_z^a / kJmol^{-1}
18/20₁₄	21.1 ± 1.0
18/9^a	18.4 ± 0.4

^a Reported value in the chapter 3.

4-2-2. Reduction resistivity of $18/20_{14}$ in the presence of ascorbic acid

The concentration of ascorbic acid in the healthy adult serum was reported to be kept in the range of 14.9 to 52.8 μM by a daily intake of ascorbic acid (60 mg) [117]. When nitroxide radicals are applied to the *in vivo* MRI measurement, radical reduction occurs to result in a significant decrease in the MRI contrast [118,119,69]. For example, TEMPO derivatives such as TEMPONE and TEMPOL are reduced rapidly [half-life ($\tau_{1/2}$) < 2 min] to the corresponding hydroxylamines in the presence of ascorbic acid [82]. In our molecular design, we expected that the interplay between four long hydrophilic tails in 18 and four neighboring substituents in 20_{14} should enhance the reduction resistance to ascorbic acid sterically. The decay of 20_{14} in $18/20_{14}$ in response to a large excess of

ascorbic acid (20 equiv based on 20_{14}) in PBS was monitored by EPR spectroscopy (Figure 4-6). As expected, the $\tau_{1/2}$ of $18/20_{14}$ (30 min) was almost comparable to that of $18/9$ (33 min) and much longer than that of $6/9$ (7 min) [chapter 3].

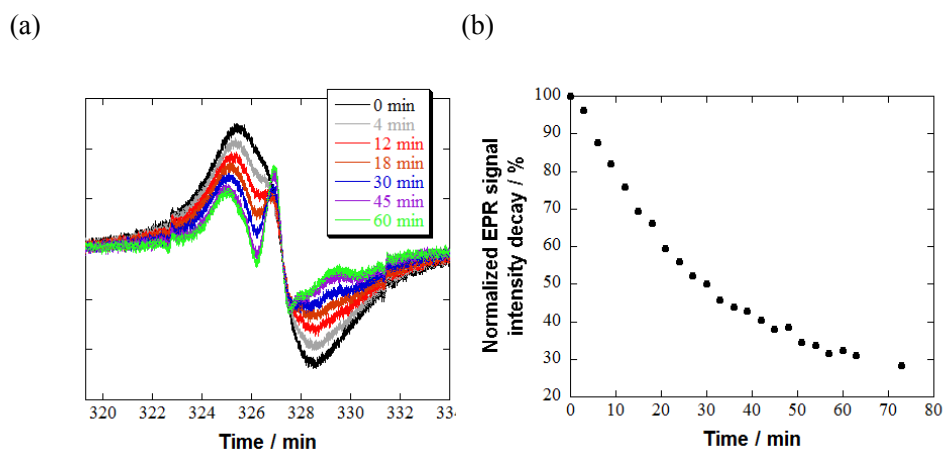


Figure 4-6. (a) Time-course of EPR spectra and (b) the reduction resistance of 20_{14} in $18/20_{14}$ to a large excess of ascorbic acid (20 equiv based on 20_{14}) in PBS at 25 °C. The normalized signal intensity decay was evaluated by a double-integration method. See the experimental section for details.

4-2-3. Biomedical application of $18/20_{14}$

Since biocompatibility is prerequisite to the magnetic mixed micelles as an MRI contrast agent, the cancer cell viability of $18/20_{14}$ was assessed by the CCK-8 assay at the initial concentration of 2.5 mM for 18 and 20_{14} and compared with those of pure micelle of 18 , designated as **P18**, (Figure 4-7a). Both of **P18** and $18/20_{14}$ exhibited little cytotoxicity to HeLa cells at concentrations up to 2.5 mM, demonstrating that $18/20_{14}$ is an appropriate candidate for *in vivo* experiment. In addition, the body weights gradually increased in the healthy ICR (Institute of Cancer Research) mice over one month after injection of $18/20_{14}$, $18/9$ and PBS (Figure 4-7b). It is concluded that mixed micelles $18/20_{14}$ can serve as a bio-compatible MRI contrast agent similar to $18/9$.

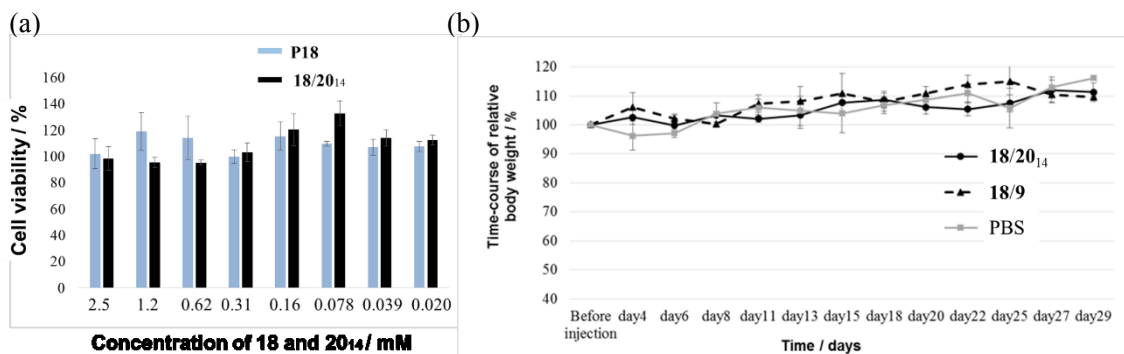


Figure 4-7. (a) *In vitro* cell viability of **18/20**₁₄ and **P18** by using the CCK-8 kit after incubation for 24 h at 37 °C under 5% CO₂ and (b) *in vivo* toxicity of **18/20**₁₄ for healthy ICR mice weight (three mice for each of **18/20**₁₄, **18/9** and control PBS) as a function of time after injection of 200 μL of mixed micelles (40 mM for each component) in PBS or PBS. See the experimental section for details.

Finally, the *in vivo* MRI experiment using **18/20**₁₄ was performed for healthy ICR mice. Bright MRI contrast enhancement was observed in the liver in both coronal and sagittal planes over 1 h with high reproducibility (Figure 4-8). This result reveals that the magnetic mixed micelle **18/20**₁₄ is effective as an *in vivo* T₁-weighted MRI contrast agent. The prolonged MRI enhancement observed for **18/20**₁₄ is attributed to the high resistance to reducing agents as described above.

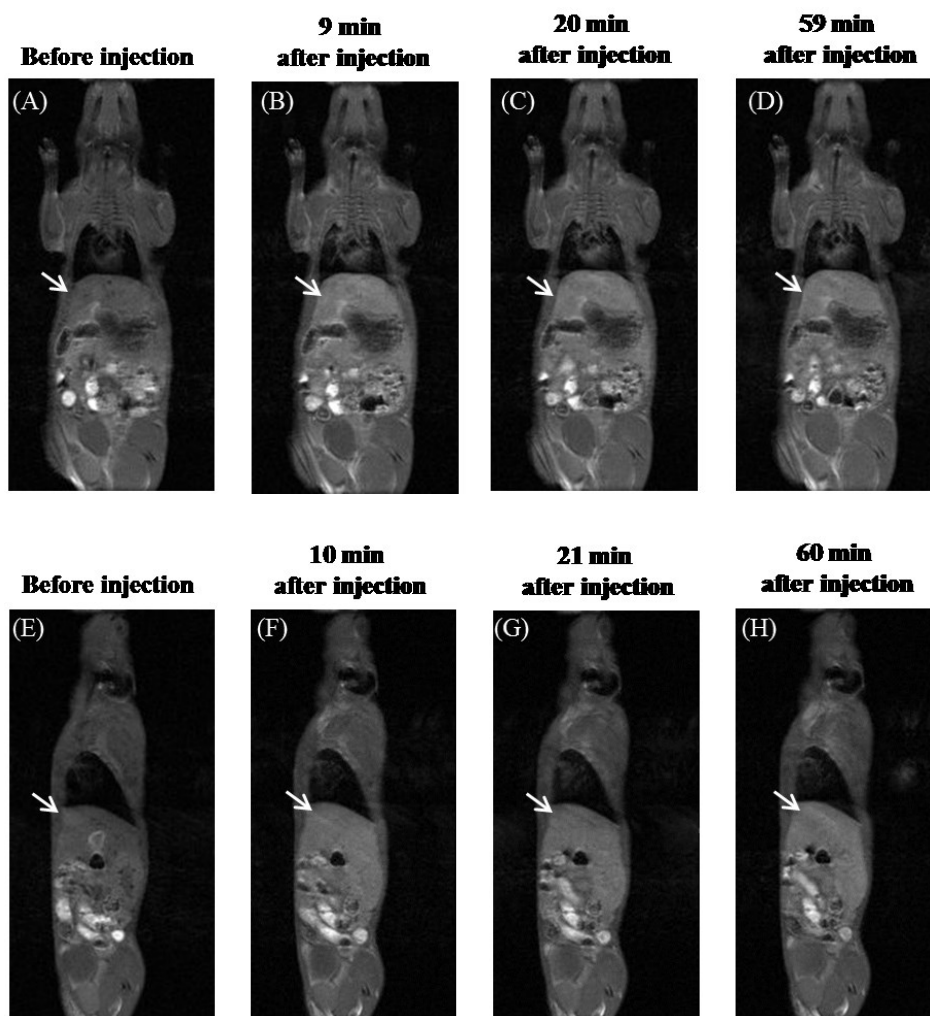


Figure 4-8. Time-course of coronal (panels A–D) and sagittal (panels E–H) T_1 -weighted MR images of an ICR mouse before and after injection of 200 μL of $^{18}\text{F}/^{20}\text{O}$ (40 mM) in PBS. Distinct contrast enhancement was observed in the liver of the mouse (indicated by white arrows). See the experimental section for details.

4-3. Conclusions

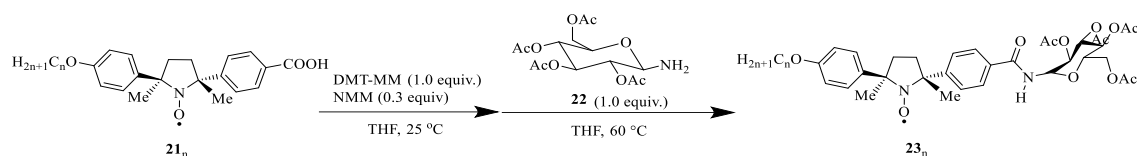
We have prepared highly robust and biocompatible metal-free magnetic mixed micelles which are composed of non-ionic surfactant **18** and hydrophobic nitroxide radical **20_n** in PBS. The time-course stability and *in vitro* MRI contrast ability of the mixed micelles was found to depend on the length (*n*) of the alkyl chain in the nitroxide radicals. In addition, the mixed micelle **18/20₁₄** showed considerable reduction resistance to a large excess of ascorbic acid, little toxicity and sufficient contrast enhancement in the *T*₁-weighted MRI *in vivo*. Such highly biocompatible magnetic mixed micelles composed of nitroxide radicals bearing a D-glucosamine unit is expected to be utilized as a low-molecular-weight cancer targeted MRI contrast agent in line with the theranostic applications of micelles, which are attracting an increasing interest recently [120,121,122].

4-4. Experimental section

4-4-1. General

The surfactant **18** [Tween 80 (DKS Co. Ltd.)] was used as received. Unless otherwise noted, solvents and reagents were reagent grade and used without further purification. Tetrahydrofuran (THF) used for EPR spectroscopy or Grignard reactions was distilled from sodium/benzophenone ketyl under argon. EPR spectra were recorded on JEOL JES-RE2X and Bruker EMX Plus. FT-IR spectrometry was performed with a Shimadzu IRSpirit instrument using a dry KBr powder. Elementary analysis was performed with a Yanaco CHN corder MT-6 instrument at the Center of Organic Elemental Microanalysis of Kyoto University.

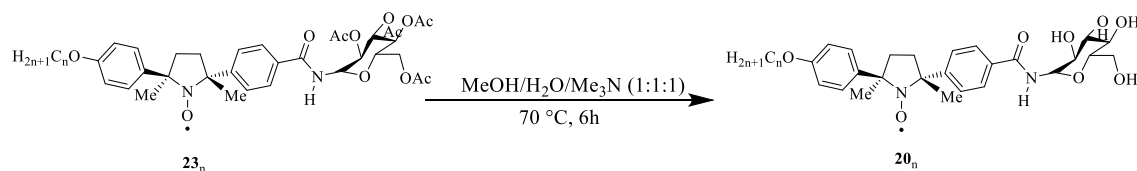
4-4-2. Synthesis



Scheme 4-1. Synthesis of **23_n** ($n = 14, 16$ and 18).

As a typical example, **23₁₈** was obtained as a ca. 1:1 mixture of D-(*R,R*) and D-(*S,S*) diastereomers as follows (Scheme 4-1). 4-(4,6-Dimethoxy-1,3,5-triazin-2-yl)-4-methylmorpholinium chloride (DMT-MM) (174 mg, 0.629 mmol) was added to a solution of (\pm)-**21₁₈** (330 mg, 0.572 mmol) [112] and *N*-methylmorpholine (NMM) (17.4 mg, 0.172 mmol) in THF at 25 °C. After stirring for 15 min, a solution of D-tetraacetylglucosamine (**22**) (238 mg, 0.686 mmol, 1.2 equiv) [114,115,116] was added, and the mixture was stirred for 16 h at 70 °C. The resultant mixture was extracted three times with CH₂Cl₂ (15 ml \times 3). The combined organic layer was dried over MgSO₄ and filtered, and the solvent was evaporated under reduced pressure. The residual solid was purified by flash column chromatography on silica gel eluting with CHCl₃/hexane/diethyl ether (50:40:10 to 60:20:20 v/v/v) to give **23₁₈** as yellow solid (175 mg, 0.193 mmol, 34%).

Similarly, **23₁₄** and **23₁₆** were prepared in 52 % and 74 % yields, respectively, as yellow solids.



Scheme 4-2. Synthesis of **20_n** ($n = 14, 16$ and 18).

As a typical example, **20**₁₈ was obtained as follows. **23**₁₈ (175 mg, 0.193 mmol) was dissolved in a mixture of H₂O, MeOH and trimethylamine (2 mL each) at 25 °C and the mixture was stirred overnight at 25 °C. The resultant solution was acidified with 5 w% H₂SO₄ to pH 6-7 and extracted three times with CH₂Cl₂ (15 ml × 3). The combined organic layer was dried over MgSO₄ and filtered, and the solvent was evaporated under reduced pressure. The residual solid was purified by flash column chromatography on silica gel eluting with CHCl₃/MeOH (90:10 v/v) to give **20**₁₈ as yellow solid (84 mg, 0.114 mmol, 59 %). Similarly, **20**₁₄ and **20**₁₆ were prepared in 41 % and 54 % yields, respectively, as yellow solids. The existence of functional groups in **20**_n (*n* = 14, 16 and 18) was confirmed by FT-IR spectroscopy (Figure 4-9). The HPLC analyses of products **20**_n (*n* = 14, 16 and 18) verified the high purity of each diastereomer mixture (Figure 4-10).

20₁₄: EPR (1.0×10^{-4} M in THF, 25 °C) *g* = 2.0063, *a*_N = 1.32 mT. Anal. Calcd for C₃₉H₅₉N₂O₈ (%): C, 68.49; H, 8.70; N, 4.10. Found (%): C, 68.15; H, 8.97; N, 3.66.

20₁₆: EPR (1.0×10^{-4} M in THF, 25 °C) *g* = 2.0065, *a*_N = 1.32 mT. Anal. Calcd for C₄₁H₆₃N₂O₈·H₂O (%): C, 67.46; H, 8.98; N, 3.84. Found (%): C, 67.19; H, 9.07; N, 3.71.

20₁₈: EPR (1.0×10^{-4} M in THF, 25 °C) *g* = 2.0065, *a*_N = 1.32 mT. Anal. Calcd for C₄₃H₆₇N₂O₈ (%): C, 69.79; H, 9.13; N, 3.79. Found (%): C, 69.60; H, 9.39; N, 3.53.

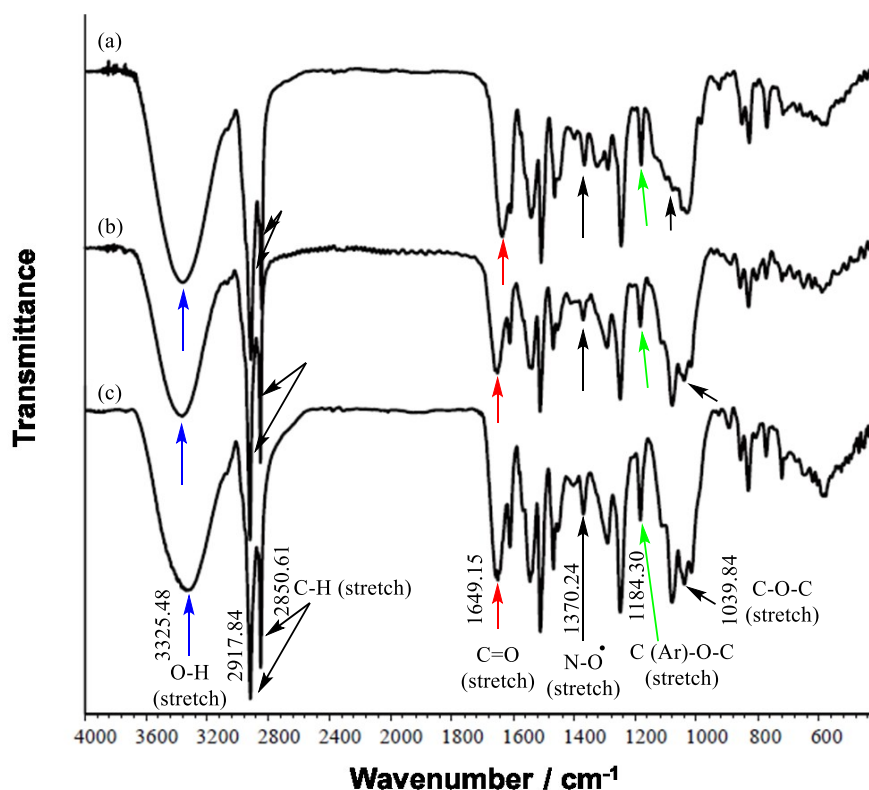


Figure 4-9. FT-IR spectra (KBr) of (a) **20**₁₄ (b) **20**₁₆ and (c) **20**₁₈. The characteristic IR absorptions for the N–O• bond has been assigned in the range 1380–1340 cm⁻¹ [123,124].

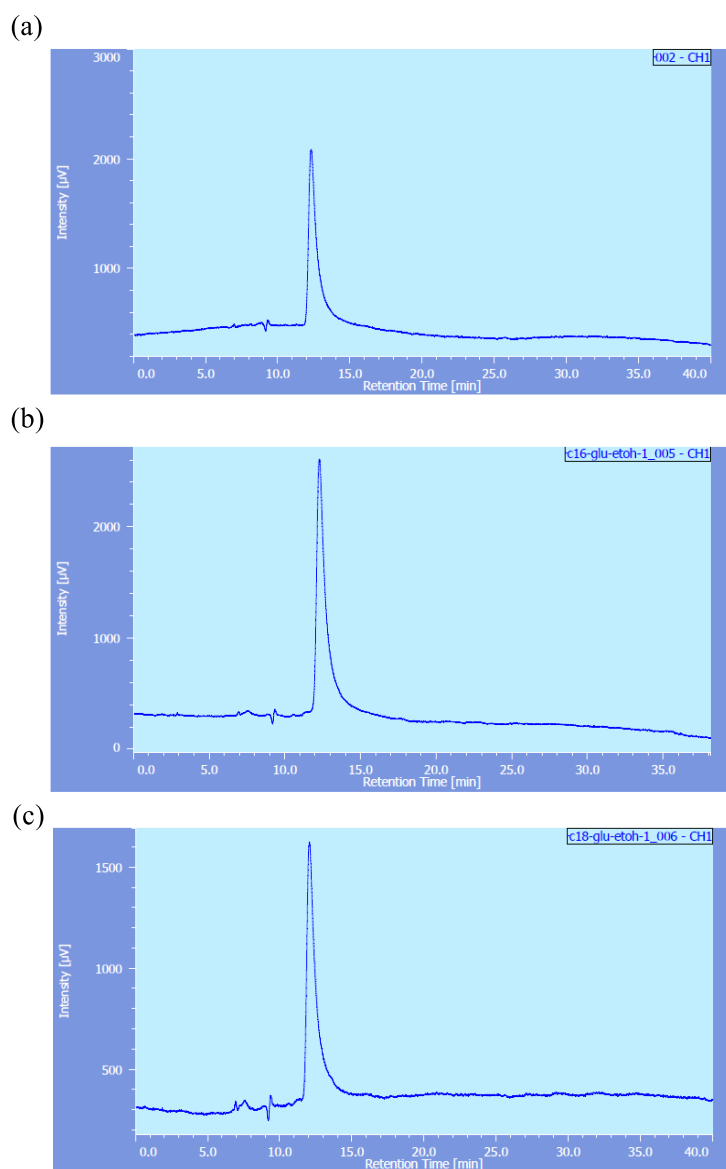


Figure 4-10. HPLC charts of (a) **20**₁₄ (b) **20**₁₆ and (c) **20**₁₈. HPLC analysis was carried out by using a silica gel column (YMC-Pack SIL-06, 0.46 x 30 cm) at 30 °C, a mixture of hexane and ethanol (6:4 v/v) as the mobile phase at a flow rate of 0.5 mL/min, and UV-vis spectrometer (254 nm) as the detector.

4-4-3. Preparation of magnetic mixed micelles 18/20_n (n = 14, 16 and 18) in PBS

As a typical example, **18/20**₁₄ (10 mM for each component) was prepared in PBS as follows. To a glass vial containing **20**₁₄ (13.67 mg, 20 μmol) was added **18** (10 mM) dissolved in PBS (2.0 mL). The mixture was subjected to sonication (Branson Model 5800, frequency 40 kHz) for more than 10 min at 25 °C to give a white suspension. Then the suspension was heated for more than 10 min at 90 °C using a water bath to form a clear yellow dispersion of **18/20**₁₄, which was passed through a 0.45 μm membrane filter. **18/20**₁₆ and **18/20**₁₈ (10 mM each), and **18/20**₁₄ (40 mM each) in PBS were prepared

by the same procedure.

4-4-4. DLS measurement (Table 4-1 and Figure 4-2)

The mean diameter of mixed micelles was determined by using a UPA-UT151 instrument (MicrotrackBEL) at 25 °C. After the samples were passed through a 0.45 μm ϕ disposable membrane filter, the particle size was measured in PBS using an attached cuvette. The mean diameter was calculated on volume and number weighted averages from five measurements for each sample. Only volume average size distributions are described in this paper. Polydispersity index was not available by using the present instrument.

4-4-5. EPR spectroscopy

4-4-5-1. Determination of rotation diffusion coefficient (D_r) (Table 4-2 and 4-3, and Figure 4-4 and 4-5)

The EPR spectra of **18/20**₁₄ (a ratio of 1: 0.01 of **18** to **20**₁₄) were recorded at 100 K in the temperature range of 263 to 298 K on Bruker EMX Plus spectrometer (X-band). The variable temperature unit (Bruker) was used to control the temperature. Microwave powers were chosen carefully, especially in the low-temperature measurement, to prevent the signal saturation arising from prolonged spin-lattice relaxation time of a radical magnetization vector. Modulation amplitudes were kept below 1/2 to 1/3 times of peak-to-peak line widths. For the experiment at 298K the samples were placed into glass capillary tubes (~ 1 mm ϕ). For the experiment at 100 K, the samples in the plastic tubes (~ 4 mm ϕ) were dipped quickly in liq. N₂ to be frozen. The rotation diffusion coefficients and angles (beta and gamma) that define the position of rotation axis of the probe in the g -tensor frame, were determined by nonlinear-least squares simulation of the experimental ESR spectra, i. e. by minimizing the discrepancy (sum of squared deviations) between the experimental and the simulated spectra. The errors of determined parameters were estimated on the basis of covariance matrix at the point of minimum. The magnetic parameters of the radicals (principal values of g - and hfc -tensors) were determined independently from the spectra recorded at 100 K. The detailed EPR fitting procedure was described in the chapter 3.

4-4-5-2. Measurement of reduction resistance of the mixed micelles to a large excess of ascorbic acid (Figure 4-6)

To **18/20**₁₄ (10 mM each) in PBS (1.5 mL) was added 20 equiv of ascorbic acid. The mixture was transferred to a capillary tube (1 mm ϕ) immediately, followed by the measurement of EPR spectra during the process of the radical reduction. The spectra were collected with the following parameters; 1.00 mW of microwave power, 0.079 mT of modulation, 0.10 s of time constant, and 120 sec of sweep time. This experiment was performed twice and the high reproducibility was confirmed.

4-4-6. Evaluation method of *in vitro* cytotoxicity (Figure 4-7a)

HeLa cells (8,200 cells in 100 μ L per well) were seeded at in a 96-well tissue culture plate with Dulbecco's modified Eagle's medium (DMEM) containing 10% fetal bovine serum and 1% penicillin/streptomycin and grown for 24 h at 37 °C with 5% CO₂. Then, each well was treated with a PBS dispersion (10 μ L) of **P18** or **18/20**₁₄. The initial dispersion of the mixed micelles containing 2.5 mM of **18** and **20**₁₄ and diluted dispersion of 1.2, 0.62, 0.31, 0.16, 0.078, 0.039 and 0.020 mM were applied to the cells before incubation. After incubation for 24 h at 37 °C under 5% CO₂, these compounds shown above were removed and then cell toxicity was assayed using CCK-8 kit according to the manual provided by the kit manufacture (Dojindo Molecular Technologies).

4-4-7. *In vivo* toxicology test (Figure 4-7b)

The protocols for the animal experiments were approved by the Shiga University of Medical Science (approval number: 2018-4-1) and were carried out in accordance with the National Institutes of Health Animal Care and Use Protocol (NIH, Bethesda, MD, USA). Female ICR mice (aged 7 weeks, body weight 32 to 34 g) were supplied from Japan SLC Inc. (Shizuoka, Japan) and nine mice were used for the toxicological experiments. Three mice were housed per cage in climate-controlled, circadian-rhythm-adjusted rooms, and were allowed access to food and water *ad libitum*.

To evaluate the toxicity of the mixed micelles to an animal, 200 μ L of **18/20**₁₄ (40 mM each), or controls **18/9** (40 mM) in PBS or PBS were intravenously administered to nine mice which were separated into three groups under anesthesia with 1.5% isoflurane. The body weight of each mouse (30 to 32 g) before injection was normalized to 100 in order to make valid comparisons, and the body weight changes of three different ICR mice were monitored for **18/9**₁₄, **18/9** (employed as *in vivo* MRI contrast agent in the chapter 2) and PBS over one month. The mean body weight values of three measurements at each day were plotted with the standard deviation represented by error bars.

4-4-8. Evaluation method of *in vitro* MRI experiment (Figure 4-3)

In vitro MRI measurement was conducted on a 7-Tesla preclinical scanner (BioSpec 70/20 USR; Bruker BioSpin MRI GmbH, Ettlingen, Germany). The initial PBS dispersion of **18/20**_n (10 mM each) and diluted dispersions of 5.0, 2.5 and 1.2 mM were prepared. These mixed micelles were transferred to plastic tubes and fixed in a sample holder. The MR relaxometry was conducted at 25 °C. MR phantom images were obtained by a rapid acquisition with relaxation enhancement (RARE) pulse sequence with variable repetition time (TR) [echo time (TE) = 11 ms, rare factor = 2, repetition time (TR) = 5,000, 3,000, 1,500, 800, 400, 200, 100 and 50 ms, field of view = 80 \times 40 mm², acquisition matrix size = 256 \times 128, slice thickness = 2.00 mm]. In the acquired images, region-of-interest (ROI) was set on each tube and the mean signal intensities within the ROI were measured for the TR-varied images. *T*₁ values were calculated by fitting a saturation recovery equation to the plot of signal

intensity versus TR by using the image sequence analysis tool in ParaVision 5.1 (Bruker BioSpin).

4-4-9. *In vivo* MRI experiment (Figure 4-8)

All animal procedures for *in vivo* MRI measurement were conducted in accordance with guidelines of animal experiments of Kyoto University (approval number: 30–A–9). Male ICR mice (n = 2, aged 7 weeks, body weight 32 to 34 g; JAPAN SLC. Inc., Shizuoka, Japan) were used. After the induction of anesthesia with isoflurane, mice were placed in a cradle in prone position. The anesthesia was kept with an inhalation of 2% isoflurane in air at 1.4 L/min through a face mask. Respiratory rate and rectal temperature were continuously measured using a pressure-sensitive respiration sensor and thermistor temperature probe, respectively, and monitored using a monitoring system (Model 1025, MR-compatible Small Animal Monitoring & Gating System; SA Instruments, Inc., NY, USA) with a dedicated software (PC-SAM V.5.12; SA Instruments). The body temperature was maintained by a flow of warm air using a heater system (MR-compatible Small Animal Heating System, SA Instruments).

MRI measurements were conducted on a 7-Tesla preclinical scanner (BioSpec 70/20 USR; Bruker BioSpin MRI GmbH, Ettlingen, Germany). A quadrature transmit-receive volume coil (inner diameter 72 mm, T9562; Bruker BioSpin) was used for MR signal detection. After 200 μ L of **18/20**₁₄ (40 mM each) in PBS were intravenously injected into an anesthetized male ICR mouse (body weight: 32 to 34 g) lying prone in an animal holder, MRI data were acquired with a dedicated operation software (ParaVision 5.1; Bruker BioSpin). Two-dimensional multi-slice spin-echo pulse sequence with a fat suppression was used for acquiring T_1 -weighted images. The acquisition parameters were as follows; repetition time (TR) = 200 ms, echo time (TE) = 6.2 ms, field of view (FOV) = 80 \times 40 mm², acquisition matrix size = 256 \times 128, spatial resolution of 312 μ m, coronal and sagittal orientations, slice thickness = 2 mm, number of slices = 8, number of averages = 2, and scan time = 51.2 s.

4-5. Appendix

4-5-1. Stability of 6/20_n

The mixed micelles 6/20_n were prepared at concentration of 10 mM for each component in PBS as with 18/20_n. *In vitro* stability of 6/20_n was found to be similar to that of 18/20_n. 6/20₁₆ and 6/20₁₈ were formed as a clear dispersion immediately after preparation. In addition, the DLS analysis exhibited that their mean diameter gradually increased up to 23 and 16 nm after one week, respectively (Table 4A-1). The micelle 6/20₁₄ collapsed within one day to give white precipitates. From these results summarized in Table 4-4, the relative stability of the micelles 6/20_n in PBS is in the following order; 6/20₁₆, 6/20₁₈ > 18/20₁₄. The mean diameters of 6/20_n in PBS were determined to be 13 to 16 nm by DLS analysis (Table 4A-1 and Figure 4A-1a). Their mean diameters fall in a range of 10 to 100 nm which is required for the most prolonged blood circulation time.

Table 4A-1. Mean diameters and colloidal stability of the mixed micelles 18/20_n (*n* = 14, 16 and 18) in PBS at 30 °C.

Mixed micelle	6/20 ₁₄	6/20 ₁₆	6/20 ₁₈
Diameter by DLS	11 nm ^a	10 nm ^a → 23 nm ^c	14 nm ^a → 16 nm ^c
Colloidal stability	dispersion ^a → precipitates ^b	dispersion ^a → dispersion ^c	dispersion ^a → dispersion ^c

^aImmediately after preparation. ^bAfter 24 h from preparation. ^cAfter 6 days from preparation.

The broad singlet signals were obtained from 6/20_n immediately after preparation. (Figure 4A-1b,c and d).

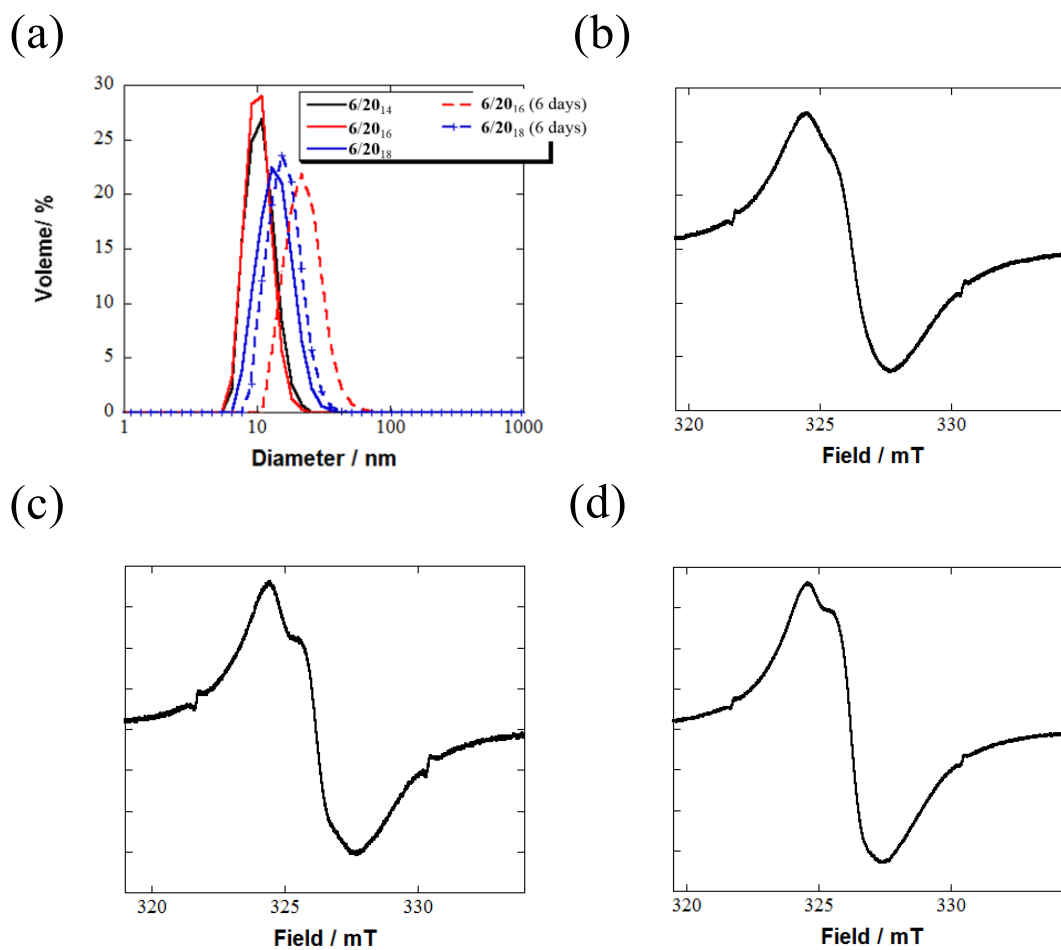


Figure 4A-1. (a) Mean diameters of mixed micelles $6/20_n$ ($n = 14, 16$ and 18) determined by DLS (black solid line: $6/20_{14}$ just after preparation, red solid line: $6/20_{16}$ just after preparation, blue solid line: $6/20_{18}$ just after preparation, red dashed line: $6/20_{16}$ after 6 days, blue dashed line: $6/20_{18}$ after 6 days) and EPR spectra of (b) $6/20_{14}$, (c) $18/20_{16}$ and (d) $6/20_{18}$ at $25\text{ }^\circ\text{C}$ in PBS.

4-5-2. Results of EPR spectral simulation

In Table 4A-2, the author shows the preparation conditions of the mixed micelles used for the EPR simulation in the chapter 4. The author prepared the mixed micelles containing 0.10 mM or 0.25 mM of 20_{14} for both $6/20_{18}$ and $18/20_{18}$ to investigate the effect of radicals' concentration on their mobility in the mixed micelles.

Table 4A-2. Preparation conditions of **6/20**₁₄ or **18/20**₁₄.

Mixed micelle	18/20 ₁₄ with a molar ratio of 1 : 0.01 ^a	18/20 ₁₄ with a molar ratio of 1 : 0.02	6/20 ₁₄ with a molar ratio of 1 : 0.01	6/20 ₁₄ with a molar ratio of 1 : 0.02
---------------	--	---	--	--

^a The result is described above.

Rigid-limit EPR spectra of **18/20**₁₄ with a molar ratio of 1 : 0.02, **6/20**₁₄ with a molar ratio of 1 : 0.01 and **6/20**₁₄ with a molar ratio of 1 : 0.02, and the results of their computer simulation are shown in Table 4A-3 and Figure 4A-2.

Table 4A-3. Magnetic parameters obtained from rigid-limit EPR spectrum recorded at 100 K.

Mixed micelles	g_x	g_y	g_z	A_x / G	A_y / G	A_z / G	Discrepancy ($\times 10^{-9}$)
18/20 ₁₄ (1 : 0.01)	2.0088	2.0067	2.0025	2.130	3.906	32.64	0.973
18/20 ₁₄ (1 : 0.02)	2.0088	2.0067	2.0024	3.345	3.345	32.72	0.560
6/20 ₁₄ (1 : 0.01)	2.0091	2.0061	2.0024	1.548	5.722	33.38	0.525
6/20 ₁₄ (1 : 0.02)	2.0093	2.0060	2.0024	3.496	3.496	33.17	0.233

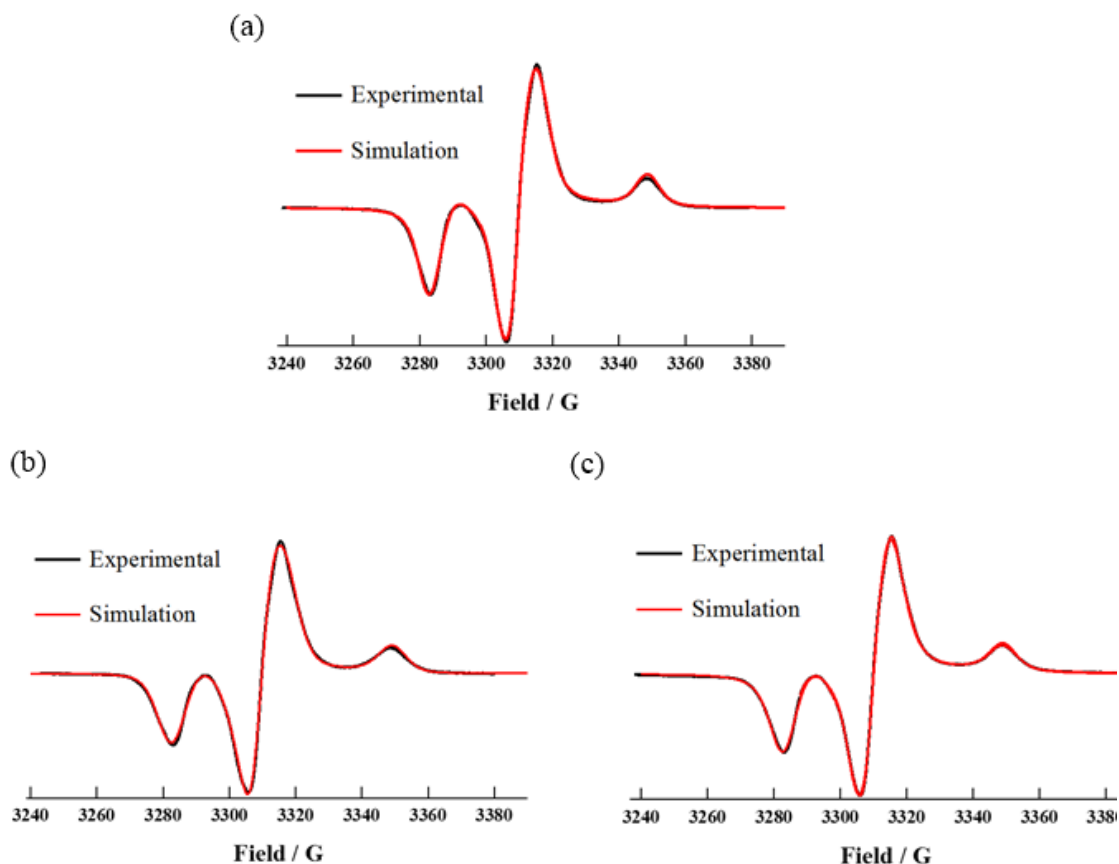


Figure 4A-2. EPR spectra of (a) $18/20_{14}$ with a molar ratio of 1 : 0.02, (b) $6/20_{14}$ with a molar ratio of 1 : 0.01 and (c) $6/20_{14}$ with a molar ratio of 1 : 0.02 and the results of their computer simulation at 100 K. Black lines – experimental spectra, red lines – results of simulation. See the experimental section for details.

Next, the author simulated the slow-motion EPR spectra (263 K – 298 K) of each mixed micelles by using the parameters in Table 4A-3. The simulation results of $18/20_{14}$ (1 : 0.02), $6/20_{18}$ (1 : 0.01) and $6/20_{18}$ (1 : 0.02) were summarized in Table 4A-4. The mark D_z ($\times 10^8$ Hz) denotes the diffusion coefficient for rotation around Z axis and the representative results for simulation of several spectra are presented in Figures 4A-3, 4A-4 and 4A-5.

Table 4A-4. Rotation diffusion coefficients and the angles determining the position of the main rotation axis in g-tensor frame for radical 20_{14} in $18/20_{14}$ (1 : 0.02), $6/20_{14}$ (1 : 0.01) and $6/20_{14}$ (1 : 0.02).

Temp., K	$18/20_{14}$ (1 : 0.02)			$6/20_{14}$ (1 : 0.01)		
	$D_z, 10^8 \text{ s}^{-1}$	Beta ^a , °	Gamma ^a , °	$D_z, 10^8 \text{ s}^{-1}$	Beta ^a , °	Gamma ^a , °
298	3.49	44.8	71.8	4.09	47.7	65
293	3.20	43.9	89.9			
288	2.76	43.1	89.4			
283	2.38	42.1	90.0	3.16	44.1	90.0
281	2.24	41.8	90.0	2.82	44.0	89.9
279	2.02	41.7	90.0	2.62	43.9	90.0
277	1.93	41.0	89.9	2.42	43.4	90.0
275	1.77	40.6	90.0	2.33	42.5	90.0
273	1.56	40.6	90.0	2.05	42.2	89.9
271	1.47	40.2	90.0	1.83	42.0	90.0
269	1.32	39.6	90.0	1.90	39.6	90.0
267	1.33	37.1	90.0	1.77	38.6	90.0
265	1.20	36.7	89.8	1.53	39.3	90.0
263	1.13	35.0	90.0	1.59	30.6	90.0
	$6/20_{14}$ (1 : 0.02)					
298	3.99	46.5	63.0			
293	3.58	45.7	64.4			
288						
283	2.79	43.2	70.1			
281	2.57	43.0	75.9			
279	2.49	42.0	89.9			
277	2.29	41.6	89.9			
275	2.19	40.5	90.0			
273						
271	2.00	39.0	89.8			
269	1.76	38.3	89.8			
267	1.69	36.3	71.7			
265	1.45	35.2	89.2			
263	1.14	33.4	90.0			

^aEuler angles describe the transformation of rotation frame to g-tensor frame. ^bError values are

presented.

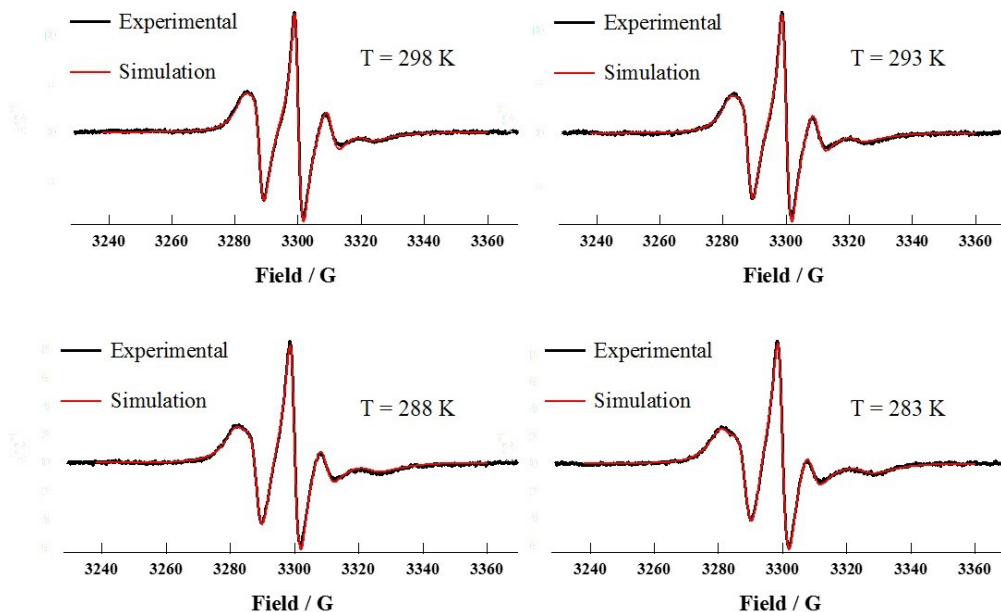


Figure 4A-3. Representative EPR spectra of 18/20₁₄ (a molar ratio of 1 : 0.02) and the results of their computer simulation at high temperatures. Black lines denote the experimental spectra, red lines represent the results of simulation.

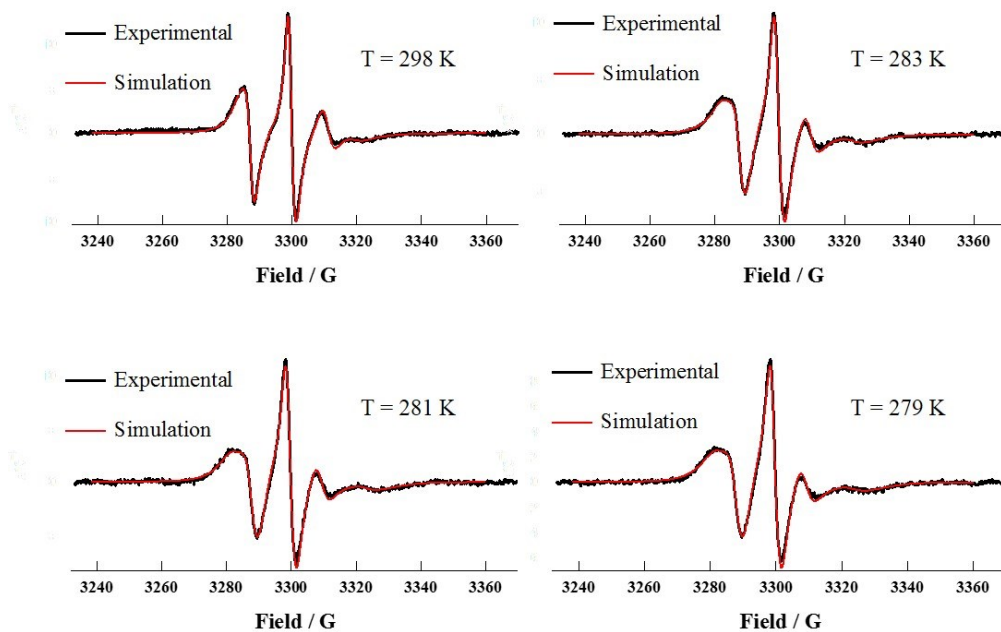


Figure 4A-4. Representative EPR spectra of 6/20₁₄ (a molar ratio of 1 : 0.01) and the results of their computer simulation at high temperatures. Black lines denote the experimental spectra, red lines represent the results of simulation.

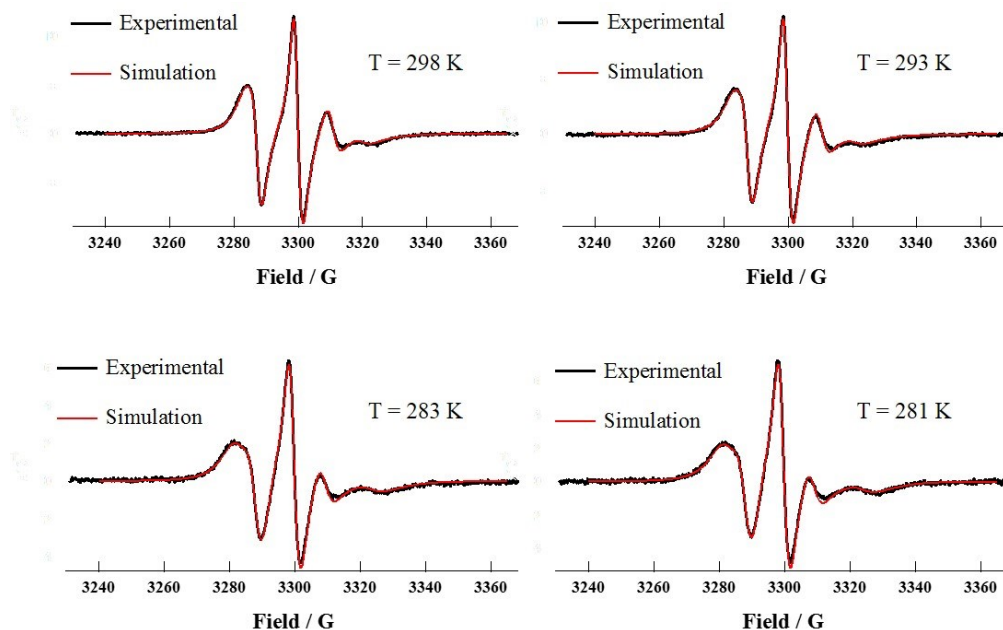


Figure 4A-5. Representative EPR spectra of $6/20_{14}$ (a molar ratio of 1 : 0.02) and the results of their computer simulation at high temperatures. Black lines denote the experimental spectra, red lines represent the results of simulation.

Arrhenius plot for D_z values of the mixed micelles are created by using the simulatinal results in Table 4A-4 (Figure 4A-6).

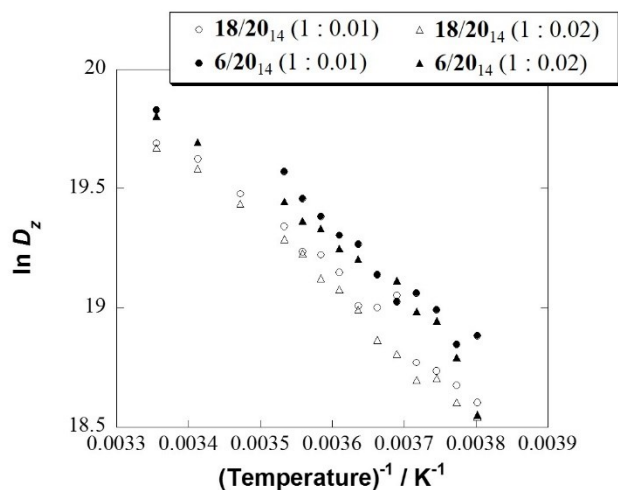


Figure 4A-6. Temperature dependence of rotation diffusion coefficient D_z of 20_{14} in $6/20_{14}$ and $18/20_{14}$ with the ratio of 1 : 0.01, and $6/20_{14}$ and $18/20_{14}$ with the ratio of 1 : 0.02. See the experimental section for details.

It was found that the rotational diffusion of 20_{14} in $18/20_{14}$ was smaller than that in $6/20_{14}$. The linear regression analysis yielded the E_z values of each mixed micelle. Furthermore, D_z values at 273 K were evaluated from the linear equation (Table 4A-5).

Table 4A-5. D_z at 273 K and E_z^a values of 9_{18} in $6/9_{18}$ and $18/9_{18}$ with the ratio of 1 : 0.01, and $6/9_{18}$ and $18/9_{18}$ with the ratio of 1 : 0.02.

Mixed micelle	$18/20_{14}$ with a molar ratio of 1 : 0.01 ^a	$18/20_{14}$ with a molar ratio of 1 : 0.02	$6/20_{14}$ with a molar ratio of 1 : 0.01	$6/20_{14}$ with a molar ratio of 1 : 0.02
D_z / s^{-1}	2.1 ± 1.1	1.7 ± 0.6	2.7 ± 1.6	2.7 ± 1.9
$E_z^a / \text{kJ/mol}$	21.1 ± 1.0	22.3 ± 0.6	19.6 ± 1.1	21.1 ± 1.4

^a These results are described above.

According to Table 4A-5, there is no difference in E_z^a values between the four micelles. This is probably because the internal structure of $18/20_{14}$ is similar to that of $6/20_{14}$ irrespective of the concentration of 20_{14} .

Finally, the author summarized the simuational results based on the concentration of the radicals in the mixed micelles (Figure 4A-7).

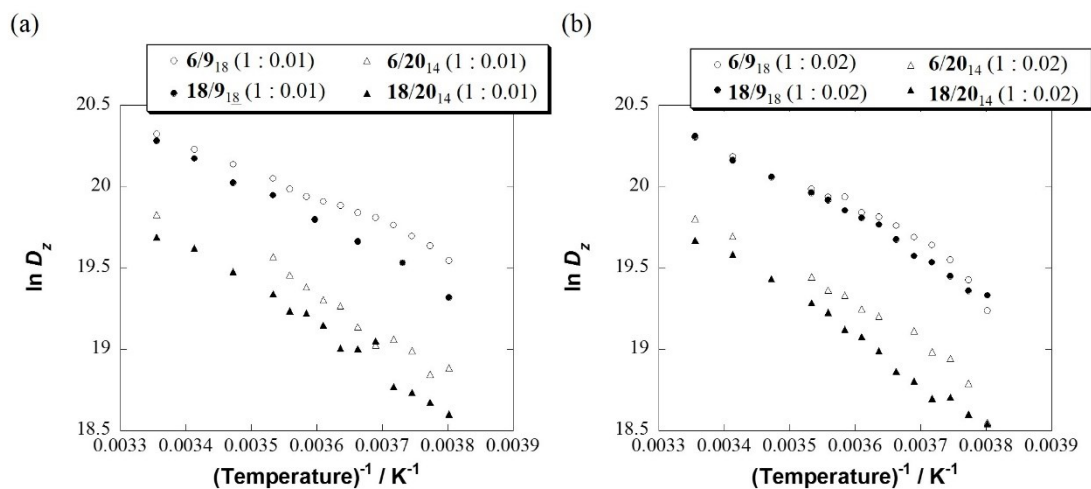


Figure 4A-7. Temperature dependence of rotation diffusion coefficient D_z of $\mathbf{9}_{18}$ or $\mathbf{20}_{14}$ in $\mathbf{6/9}_{18}$, $\mathbf{18/9}_{18}$, $\mathbf{6/20}_{14}$ and $\mathbf{18/20}_{14}$ with the ratio of (a) 1 : 0.01 or (b) 1 : 0.02. See the experimental section for details.

One can see that the D_z values of $\mathbf{20}_{14}$ are smaller than those of $\mathbf{9}_{18}$ in the entire temperature range. This is because that $\mathbf{20}_{14}$ bearing hydrogen-bond donating NH and OH groups should interact with neighboring hydroxy groups of surfactants **6** or **18** via hydrogen bonds to form a highly hydrophobic environment with high viscosity inside the mixed micelles. However, the property of the surfactant used for the formation of the mixed micelle seems not to make an impact on the D_z and E_z^a values.

References

- [1] Lahti, P. M. Structure–property relationships for metal-free organic magnetic materials. *Adv. Phys. Org. Chem.*, **2011**, *45*, 93–169.
- [2] Likhtenshtein, G. I.; Yamauchi, J.; Nakatsuji, S.; Smirnov, A. I.; Tamura, R. *Nitroxides: Applications in Chemistry, Biomedicine, and materials Science*, Wiley-VCH, Weinheim, **2008**.
- [3] Itoh, K.; Kinoshita, M. *Molecular Magnetism New Magnetic Materials*, Kodansha Gordon and Breach Science Publishers, Tokyo, **2000**.
- [4] Sugawara, T.; Komatsu, H.; Suzuki, K. Interplay between magnetism and conductivity derived from spin-polarized donor radicals. *Chem. Soc. Rev.*, **2011**, *40*, 3105–3118.
- [5] Amabilino, D.B.; Veciana, J. in *Magnetism: Molecules to Materials II*, ed. J. S. Miller, J.S.; Drillon, M. Wiley-VCH, Weinheim, **2001**, pp. 1–60.
- [6] Kaszynski, P. Liquid crystalline radicals: An emerging class of organic molecules. ed. By Lahti, P.M.; Dekker, M. New York, 1999, p. 305
- [7] Kats, E.I.; Lebedev, V.V. Some Properties of Ferromagnetic Liquid Crystals. *Mol. Cryst. Liq. Cryst.* **1991**, *209*, 329–337.
- [8] Binnemans, K.; Görrler-Walrand, C. Lanthanide-containing liquid crystals and surfactants. *Chem. Rev.* **2002**, *102*, 2303–2345.
- [9] Dunmur, D.; Tokoroyama, K. in *Physical Properties of Organic Materials* (Eds.: Demus, D.; Goodby, J.; Gray, G.W.; Spiess, H.-W.; Vill, V.), Wiley-VCH, Weinheim, **1999**, pp. 102–112.
- [10] Dierking, I. Textures of liquid crystals. Wiley-VCH Verlag, Weinheim, **2003**, pp. 1–60.
- [11] Uchida, Y.; Suzuki, K.; Tamura, R.; Ikuma, N.; Shimono, S.; Noda, Y.; Yamauchi, J. Anisotropic and inhomogeneous magnetic interactions observed in all-organic nitroxide radical liquid crystals. *J. Am. Chem. Soc.* **2010**, *132*, 9746–9752.
- [12] Suzuki, K.; Uchida, Y.; Tamura, R.; Shimono, S.; Yamauchi, J. Observation of positive and negative magneto-LC effects in all-organic nitroxide liquid crystals by EPR spectroscopy. *J. Mater. Chem.* **2012**, *22*, 6799–6806.
- [13] Suzuki, K.; Takemoto, Y.; Takaoka, S.; Taguchi, K.; Uchida, Y.; Mazhukin, D.G.; Grigor'ev, I.A.; Tamura, R. Chiral all-organic nitroxide biradical liquid crystals showing remarkably large positive magneto-LC effects. *Chem. Commun.* **2016**, *52*, 3935–3938.
- [14] Takemoto, Y.; Zaytseva, E.; Suzuki, K.; Yoshioka, N. Takanishi, Y. Funahashi, M. Uchida, Y.; Akita, T.; Park, J.; Sato, S.; Clevers, S.; Coquerel, G.; Mazhulin, D.; Shimono, S.; Sugiyama, M.; Takahashi, H.; Yamauchi, J.; Tamura, R. Unique superparamagnetic-like behavior observed in non- π -delocalized nitroxide diradical compounds showing discotic liquid crystalline phase. *Chem. Eur. J.* **2018**, *24*, 17293–17302.
- [15] Vorobiev, A.Kh.; Chumakova, N.A.; Pomogailo, D.A.; Suzuki, K.; Noda, Y.; Tamura, R. Determination of structural characteristics of all-organic radical liquid crystals based on analysis of the dipole–dipole broadened EPR spectra. *J. Phys. Chem. B* **2014**, *118*, 1932–1942.
- [16] Uchida, Y.; Iwai, Y.; Akita, T.; Mitome, T.; Suzuki, K.; Tamura, R.; Nishiyama, N. Magnetically transportable core–shell emulsion droplets with an antioxidative all-organic paramagnetic liquid shell. *J. Mater. Chem. B* **2014**, *2*, 4130–4133.
- [17] Stark, W.J. *Angew. Chem. Int. Ed.* **2011**, *50*, 1242–1258.
- [18] Goesmann, H.; Feldmann, C. *Angew. Chem. Int. Ed.* **2010**, *49*, 1362–1395. *Angew. Chem.* 2010, *122*, 1402–1437.
- [19] *Magnetic Nanomaterials: Nanomaterials for the Life Sciences, Vol. 4* (Ed.: C. Kumar), Wiley-VCH, Weinheim, **2009**.

-
- [20] Huang, J.; li, Y.; Orza, Y.A.; Lu, Q.; Guo, P.; Wang, L.; Yang, L.; Mao, H. Magnetic nanoparticle facilitated drug delivery for cancer therapy with targeted and image-guided approaches. *Adv. Funct. Mater.* **2016**, *26*, 3818–3836.
- [21] Al-Ahmady, Z.; Kostarelos, K. Chemical components for the design of temperature-responsive vesicles as cancer therapeutics. *Chem. Rev.* **2016**, *116*, 3883–3918.
- [22] Laurent, S.; Forge, D.; Port, M.; Roch, A.; Robic, C.; Elst, L. V.; Muller, R. N. Magnetic iron oxide nanoparticles: Synthesis, stabilization, vectorization, physicochemical characterizations, and biological Applications. *Chem. Rev.* **2008**, *108*, 2064–2110.
- [23] Lu, A.-H.; Salabas, E. L.; Sheth, F. Magnetic nanoparticles: synthesis, protection, functionalization, and application. *Angew. Chem. Int. Ed.* **2007**, *46*, 1222–1244.
- [24] Corot, C.; Robert, P.; Idée, J.-M.; Port, M. Recent advances in iron oxide nanocrystal technology for medical imaging. *Adv. Drug Delivery Rev.* **2006**, *58*, 1471–1504.
- [25] Piazza, M.; Colombo, M.; Zanoni, I.; Granucci, F.; Tortora, P.; Weiss, J.; Gioannini, T.; Prospero, D.; Peri, F. Uniform lipopolysaccharide (LPS)-loaded magnetic nanoparticles for the investigation of LPS–TLR4 signaling. *Angew. Chem. Int. Ed.* **2011**, *50*, 622–626.
- [26] Chen, H.; Deng, C.; Zhang, X. Synthesis of Fe₃O₄@SiO₂@PMMA core–shell–shell magnetic microspheres for highly efficient enrichment of peptides and proteins for MALDI-ToF MS Analysis. *Angew. Chem. Int. Ed.* **2010**, *49*, 607–611.
- [27] Zhao, L.; Chano, T.; Morikawa, S.; Saito, Y.; Shiino, A.; Shimizu, S.; Maeda, T.; Irie, T.; Aonuma, S.; Okabe, H.; Kimura, T.; Inubushi, T.; Komatsu, N. Hyperbranched Polyglycerol - Grafted Superparamagnetic Iron Oxide Nanoparticles: Synthesis, Characterization, Functionalization, Size Separation, Magnetic Properties, and Biological Applications. *Adv. Funct. Mater.* **2012**, *22*, 5107–5117.
- [28] Mikhaylov, C.; Mikac, U.; Magaeva, A. A.; Itin, V.I.; Naiden, E. P.; Psakhye, I.; Babes, L.; Reinheckel, T.; Peters, C.; Zeiser, R.; Bogoyo, M.; Turk, V.; Psakhye, S.G.; Turk, B.; Vasiljeva, O. Ferri-liposomes as an MRI-visible drug-delivery system for targeting tumours and their microenvironment. *Nat. Nanotechnol.* **2011**, *6*, 594–602.
- [29] Cheong, S.; Ferguson, P.; Feindel, K. W.; Hermans, I. F.; Callaghan, P. T.; Meyer, C.; Slocombe, A.; Su, C.-H.; Cheng, F.-Y.; Yeh, C.-S.; Ingham, B.; Toney, M.F.; Tilley, R. D. Simple synthesis and functionalization of iron nanoparticles for magnetic resonance imaging. *Angew. Chem. Int. Ed.* **2011**, *50*, 4206–4209.
- [30] Zhuang, X.; Xiao, C.; Oyaizu, K.; Chikushi, N.; Chen, X.; Nishide, H. Synthesis of amphiphilic block copolymers bearing stable nitroxyl radicals. *J. Polym. Sci. Part A* **2010**, *48*, 5404–5410.
- [31] Yoshitomi, T.; Suzuki, R.; Mamiya, T.; Matsui, H.; Hirayama, A.; Nagasaki, Y. pH-Sensitive radical-containing-nanoparticle (RNP) for the L-band-EPR imaging of low pH circumstances. *Bioconjugate Chem.* **2009**, *20*, 1792–1798.
- [32] Yoshitomi, T.; Miyamoto, D.; Nagasaki, Y. Design of core–shell-type nanoparticles carrying stable radicals in the core. *Biomacromolecules* **2009**, *10*, 596–601.
- [33] Bye, N.; Hutt, O. E.; Hinton, T. M.; Acharya, D. P.; Waddington, L. J.; Moffat, B. A.; Wright, D. K.; Wang, H. X.; Mulet, X.; Muir, B. W. Nitroxide-loaded hexosomes provide MRI contrast in vivo. *Langmuir* **2014**, *30*, 8898–8906.
- [34] Muir, B. W.; Acharya, D. P.; Kennedy, D. F.; Mulet, X.; Evans, R. A.; Pereira, S. M.; Wark, K. L.; Boyd, B. J.; Nguyen, T.; Hinton, T. M.; Waddington, L. J.; Kirby, N.; Wright, D. K.; Wang, H. X.; Egan, G. F.; Moffat, B. A. Metal-free and MRI visible theranostic lyotropic liquid crystal nitroxide-based nanoparticles. *Biomaterials* **2012**, *33*, 2723–2733.
-

-
- [35] A. Rajca, Y. Wang, M. Boska, J. T. Paletta, A. Olankitwanit, M. A. Swanson, D. G. Mitchell, S. S. Eaton, G. R. Eaton, S. Rajca, *J. Am. Chem. Soc.* **2012**, *134*, 15724–15727.
- [36] Sowers, A.; McCombs, J. R.; Wang, Y.; Palette, J. T.; Morton, S. W.; Dreaden, E. C.; Boska, M.D.; Ottaviani, M. F.; Hammond, P.T.; Rajca, A.; Johnson, J. A. Redox-responsive branched-bottlebrush polymers for in vivo MRI and fluorescence imaging. *Nat. Commun.* **2014**, *5*, 5460–5468.
- [37]. Rai, P.; Mallidi, S.; Zheng, X.; Rahmanzadeh, R.; Mir, Y.; Elrington, S.; Khurshid, A.; Hasan, T. Development and applications of photo-triggered theranostic agents. *Adv. Drug Deliv. Rev.* **2010**, *62*, 1094–1124.
- [38] Li, Y.; Budamagunta, M.S.; Luo, J.; Xiao, W.; Voss, J.C.; Lam, K.S. Probing of the assembly structure and dynamics within nanoparticles during interaction with blood proteins. *ACS Nano* **2012**, *6*, 9485–9495.
- [39]. Roser, M.; Fischer, D.; Kissel, T. Surface-modified biodegradable albumin nano- and microspheres. II. Effect of surface charges on in vitro phagocytosis and biodistribution in rats. *Eur. J. Pharm. Biopharm.* **1998**, *46*, 255–263.
- [40]. Owens III, D. E.; Peppas, N. A. Opsonization, biodistribution, and pharmacokinetics of polymeric nanoparticles. *Int. J. Pharm.* **2006**, *307*, 93–102.
- [41] Nagura, K.; Takemoto, Y.; Moronaga, S.; Uchida, Y.; Shimono, S.; Shiino, A.; Tanigaki, K.; Amano, T.; Yoshino, F.; Noda, Y.; Koizumi, S.; Komatsu, N.; Kato, T.; Yamauchi, J.; Tamura, R. Preparation of robust metal-free magnetic nanoemulsions encapsulating low-molecular-weight nitroxide radicals and hydrophobic drugs directed toward MRI-visible targeted delivery. *Chem. Eur. J.* **2017**, *23*, 15713–15720.
- [42] Chamieh, J.; Davanier, F.; Jannin, V.; Demarne, F.; Cottet, H. Size characterization of commercial micelles and microemulsions by Taylor dispersion analysis. *Inter. J. Pharm.* **2015**, *492*, 46–54.
- [43] Dupont-Leclercq, L.; Giroux, S.; Henry, B.; Rubini, P. Solubilization of amphiphilic carboxylic acids in nonionic micelles: Determination of partition coefficients from pKa measurements and NMR experiments. *Langmuir* **2007**, *23*, 10463–10470.
- [44] Schefer, J.; McDaniel, R.; Schoenborn, B. Small-angle neutron scattering studies on Brij-58 micelles. *J. Phys. Chem.* **1988**, *92*, 729–732.
- [45] Ortony, J.H.; Newcomb, C.J.; Matson, J.B.; Palmer, L.C.; Doan, P.E.; Hoffman, B.M.; Stupp, S.I. Internal dynamics of a supramolecular nanofiber. *Nat. Mater.* **2014**, *13*, 812–816.
- [46] Bales, B.L. A simple, accurate method of correcting for unresolved hyperfine broadening in the EPR of nitroxide spin probes to determine the intrinsic linewidth and Heisenberg Spin Exchange Frequency. *J. Magn. Reson.* **1980**, *38*, 193–205.
- [47] Sachse, J.H.; King, M.D.; Marsh, D. ESR determination of lipid translational diffusion coefficients at low spin-label concentrations in biological membranes, using exchange broadening, exchange narrowing, and dipole-dipole interactions. *J. Magn. Reson.* **1987**, *71*, 385–404.
- [48] Matsumoto, K. Utility decay rates of T₁-weighted magnetic resonance imaging contrast based on redox-sensitive paramagnetic nitroxyl contrast agents. *Biol. Pharm. Bull.* **2009**, *32*, 711–716.
- [49] Matsumoto, K.; Yakumar, H.; Narazaki, M.; Nakagawa, H.; Anzai, K.; Ikehara, H.; Ikota, N. Modification of nitroxyl contrast agents with multiple spins and their proton T₁ relaxivity. *Magn. Reson. Imag.* **2008**, *26*, 117–121.
- [50] Bardelang, D.; Hardy, M.; Ouari, O.; Tordo, P. in *Encyclopedia of Radicals in Chemistry, Biology and Materials, Vol.4 Polymers and Materials* (Eds: Chatgililoglu, C.; Studer, A.), John Wiley & Sons, Chichester, **2012**, pp. 1965–2015.
- [51] *Dynamic Contrast-Enhanced Magnetic Resonance Imaging in Oncology* (Eds.: Jackson, A.; Buckley, D. L.; Parker, G. J. M.), Springer-Verlag, Berlin Heidelberg, **2005**.
-

-
- [52] Wan, X.; Fu, T-C.; Funk, A.; London, R. E. Differential clearance of nitroxide MRI contrast agents from rat cerebral ventricles. *Brain Res. Bull.* **1995**, *36*, 91–96.
- [53] Matsumoto, K.; Narazaki, M.; Ikehira, H.; Anzai, K.; Ikota, N. Comparisons of EPR imaging and T₁-weighted MRI for efficient imaging of nitroxyl contrast agents. *J. Magn. Reson.* **2007**, *187*, 155–162.
- [54] Delpierre, G. R.; Lamchen, M. Nitrones. Part I. Cycloaddition of unsymmetrical olefins to the 1-pyrroline 1-oxides. *J. Chem. Soc.*, **1963**, 4693–4701.
- [55] Ishigaki, T.; Hoshikawa, A.; Yonemura, M.; Kamiyama, T.; Oishi, R.; Aizawa, K.; Sakuma, T.; Tomita, Y.; Arai, M.; Hayashi, M.; Ebata, K.; Takano, Y.; Komatsuzaki, K.; Asano, H.; Takano, Y.; Kasao, T. IBARAKI materials design diffractometer (iMATERIA)—Versatile neutron diffractometer at J-PARC. *Nucl. Instrum. Methods Phys. Res., Sect. A* **2009**, *600*, 189–191.
- [56] Zhang, F.; Ilavsky, J.; Long, G.G.; Quintana, J.P.G.; Allen, A.J.; Jemian, P.R. Glassy carbon as an absolute intensity calibration standard for small-angle scattering. *P. Metall. Mater. Trans. A* **2010**, *41*, 1151–1158.
- [57] Roe, R. *Methods of X-ray and Neutron Scattering in Polymer Science*; Oxford University Press: New York, 2000.
- [58] Caravan, P. Strategies for increasing the sensitivity of gadolinium based MRI contrast agents. *Chem. Soc. Rev.* **2006**, *35*, 512–523.
- [59] Zhao, L.; Shiino, A.; Qin, H.; Kimura, T.; Komatsu, N. Synthesis, characterization, and magnetic resonance evaluation of polyglycerol-functionalized detonation nanodiamond conjugated with gadolinium(III) complex. *J. Nanosci. Nanotechnol.* **2015**, *15*, 1076–1082.
- [60] Chan, K. W.; Wong, W. Small molecular gadolinium(III) complexes as MRI contrast agents for diagnostic imaging. *Coord. Chem. Rev.* **2007**, *251*, 2428–2451.
- [61] Braverman, I. M.; Cowper, S. Nephrogenic systemic fibrosis. *F1000 Med. Rep.* **2010**, *2*, 84–87.
- [62] Davies, G. L.; Kramberger, I.; Davis, J. J. Environmentally responsive MRI contrast agents. *Chem. Commun.* **2013**, *49*, 9704–9721.
- [63] Reiter, T.; Ritter, O.; Prince, M. R.; Nordbeck, P.; Wanner, C.; Nagel, E.; Bauer, W. R. Minimizing risk of nephrogenic systemic fibrosis in cardiovascular magnetic resonance. *J. Cardiovasc. Magn. Reson.* **2012**, *14*, 31–41.
- [64] Thomsen, H. S.; Morcos, S. K.; Almén, T. Bellin, M. Bertolotto, M.; Bongartz, G.; Clement, O.; Leander, P.; Heinz-Peer, G.; Reimer, P.; Stacul, F.; Van der Molen, A.; Webb, J.A.W. Nephrogenic systemic fibrosis and gadolinium-based contrast media: updated ESUR contrast medium safety committee guidelines. *Eur. Radiol.* **2013**, *23*, 307–318.
- [65] Winalski, C. S.; Shortkroff, S.; Mulkern, R. V.; Schneider, E.; Rosen, G. M. Magnetic resonance relaxivity of dendrimer-linked nitroxides. *Magn. Reson. Med.* **2002**, *48*, 965–972.
- [66] Garmendia, S.; Mantione, D.; Castro, S. A.; Jehanno, C.; Lezama, L.; Hedrick, J. L.; Mecerreyes, D.; Salassa, L.; Sardon, H. Polyurethane based organic macromolecular contrast agents (PU-ORCAs) for magnetic resonance imaging. *Polym. Chem.* **2017**, *8*, 2693–2701.
- [67] Nguyen, H. V. T.; Chen, Q.; Paletta, J. T.; Harvey, P.; Jiang, Y.; Zhang, H.; Boska, M. D.; Ottaviani, M. F.; Jasanoff, A.; Rajca, A.; Johnson, J. A. Nitroxide-based macromolecular contrast agents with unprecedented transverse relaxivity and stability for magnetic resonance imaging of tumors. *ACS Cent. Sci.* **2017**, *3*, 800–811.
- [68] Zhelev, Z.; Bakalova, R.; Aoki, I.; Matsumoto, K.; Gadjeva, V.; Anzaib, K.; Kanno, I. Nitroxyl radicals as low toxic spin-labels for non-invasive magnetic resonance imaging of blood–brain barrier permeability for conventional therapeutics. *Chem. Commun.* **2009**, *45*, 53–55.
-

-
- [69] Emoto, M.C.; Yamada, K.; Yamato, M.; Fujii, H.G. Novel ascorbic acid-resistant nitroxide in a lipid emulsion: An efficient brain imaging contrast agent for MRI of small rodents. *Neuroscience Letters* **2013**, *546*, 11–15.
- [70] Lu, X.; Zhang, Z.; Xia, Q.; Hou, M.; Yan, C.; Chen, Z.; Xu, Y.; Liu, R. Glucose functionalized carbon quantum dot containing organic radical for optical/MR dual-modality bioimaging. *Mater. Sci. Eng. C* **2018**, *82*, 190–196.
- [71] Chen, C.; Kang, N.; Xu, T.; Wang, D.; Ren, L.; Guo, X. Core-shell hybrid upconversion nanoparticles carrying stable nitroxide radicals as potential multifunctional nanoprobe for upconversion luminescence and magnetic resonance dual-modality imaging. *Nanoscale* **2015**, *7*, 5249–5261.
- [72] Kerwin, B. A. Polysorbates 20 and 80 used in the formulation of protein biotherapeutics: structure and degradation pathways. *J. Pharm. Sci.* **2008**, *97*, 2924–2935.
- [73] Bhattacharjee, J.; Verma, G.; Aswal, V. K.; Date, A. A.; Nagarsenker, M. S.; Hassan, P. A. Tween 80-sodium deoxycholate mixed micelles: structural characterization and application in doxorubicin delivery. *J. Phys. Chem. B* **2010**, *114*, 16414–16421.
- [74] Strickley, R. G. Solubilizing excipients in oral and injectable formulations. *Pharm. Res.* **2004**, *21*, 201–230.
- [75] Mohanty, P. S.; Dietsch, H.; Rubatat, L.; Stradner, A.; Matsumoto, K.; Matsuoka, H.; Schurtenberger, P. Synthesis and characterization of novel functional electrosterically stabilized colloidal particles prepared by emulsion polymerization using a strongly ionized amphiphilic diblock copolymer. *Langmuir* **2009**, *25*, 1940–1948.
- [76] Lozinsky, E.; Martin, V. V.; Berezina, T. A.; Shames, A. I.; Weis, A. L.; Likhtenshtein, G. I. Dual fluorophore-nitroxide probes for analysis of vitamin C in biological liquids. *J. Biochem. Biophys. Methods* **1999**, *38*, 29–42.
- [77] Hideg, E.; Kalai, T.; Hideg, K.; Vass, I. Photoinhibition of photosynthesis in vivo results in singlet oxygen production detection via nitroxide-induced fluorescence quenching in broad bean leaves. *Biochemistry* **1998**, *37*, 11405–11411.
- [78] Matsuoka, Y.; Yamato, M.; Yamasaki, T.; Mito, F.; Yamada, K. Rapid and convenient detection of ascorbic acid using a fluorescent nitroxide switch. *Free Radic. Biol. Med.* **2012**, *53*, 2112–2118.
- [79] Harrison, F. E.; May, J. M. Vitamin C function in the brain: vital role of the ascorbate transporter SVCT2. *Free Radic. Biol. Med.* **2009**, *46*, 719–730.
- [80] Vianello, F.; Momo, F.; Scarpa, M.; Rigo, A. Kinetics of nitroxide spin label removal in biological systems: an in vitro and in vivo ESR study. *Magn. Reson. Imaging* **1995**, *13*, 219–226.
- [81] Levine, M.; Padayatty, S. J.; Espey, M. G. Vitamin C: a concentration-function approach yields pharmacology and therapeutic discoveries. *Adv. Nutr.* **2011**, *2*, 78–88.
- [82] Yamasaki, T.; Mito, F.; Matsuoka, Y.; Yamato, M.; Yamada, K. In *Nitroxides - Theory, Experiment and Applications*, Kokorin, A. I., Ed.; INTECH, Rijeka, Croatia, **2012**, Chapter 8.
- [83] Zhuang, X.; Xiao, C.; Oyaizu, K.; Chikushi, N.; Chen, X.; Nishide, H. Synthesis of amphiphilic block copolymers bearing stable nitroxyl radicals. *J. Poly. Sci. Part A: Polym. Chem.* **2010**, *48*, 5404–5414.
- [84] Yoshitomi, T.; Miyamoto, D.; Nagasaki, Y. Design of core-shell-type nanoparticles carrying stable radicals in the core. *Biomacromolecules*, **2009**, *10*, 596–601.
- [85] Dobrynin, S. A.; Glazachev, Y. I.; Gatilov, Y. V.; Chernyak, E. I.; Salnikov, G. E.; Kirilyuk, I. A. Synthesis of 3,4-bis(hydroxymethyl)-2,2,5,5-tetraethylpyrrolidin-1-oxyl via 1,3-dipolar cycloaddition of azomethine ylide to activated alkene. *J. Org. Chem.* **2018**, *83*, 5392–5397.
-

-
- [86] Kirilyuk, I.A.; Bobko, A.A.; Semenov, S.V.; Komarov, D.A.; Irtegov, I.G.; Grigor'ev, I.A.; Bagryanskaya, E. Effect of sterical shielding on the redox properties of imidazoline and imidazolidine nitroxides. *J. Org. Chem.* **2015**, *80*, 9118–9125.
- [87] Paletta, J.T.; Pink, M.; Foley, B.; Rajca, S. Synthesis and reduction kinetics of sterically shielded pyrrolidine nitroxides. *Org. Lett.* **2012**, *14*, 5322–5325.
- [88] Marx, L.; Chiarelli, R.; Guiberteau, T.; Rassat, A. A comparative study of the reduction by ascorbate of 1,1,3,3-tetraethylisoindolin-2-yloxyl and of 1,1,3,3-tetramethylisoindolin-2-yloxyl. *J. Chem. Soc., Perkin Trans. 1*, **2000**, 1181–1182.
- [89] Livramento, J. B.; Tóth, E.; Sour, A.; Borel, A.; Merbach, A. E.; Ruloff, R. High Relaxivity confined to a small molecular space: A metallostar-based, potential MRI contrast agent. *Angew. Chem. Int. Ed.* **2005**, *44*, 1480–1484.
- [90] Caravan, P.; Farrar, C. T.; Frullano, L.; Uppal, R. Influence of molecular parameters and increasing magnetic field strength on relaxivity of gadolinium- and manganese-based T₁ contrast agents. *Contrast Media Mol. Imaging* **2009**, *4*, 89–100.
- [91] de Sousa, P. L.; Livramento, J. B.; Helm, L.; Merbach, A. E.; Meme W.; Doan, B. T.; Beloeil, J. C.; Prata, M. I.; Santos, A. C.; Geraldés, C. F.; Tóth, E. *In vivo* MRI assessment of a novel Gd^{III}-based contrast agent designed for high magnetic field applications. *Contrast Media Mol. Imaging* **2008**, *3*, 78–85.
- [92] Vorobiev, A. K.; Chumakova, N. A. In *Nitroxides - Theory, Experiment and Applications*, Kokorin, A. I., Ed.; INTECH, Rijeka, Croatia, **2012**, Chapter 3.
- [93] Budil, D. E.; Lee, S.; Saxena, S.; Freed, J. H. Nonlinear-least-squares analysis of slow-motion EPR spectra in one and two dimensions using a modified levenberg-marquardt algorithm. *J. Magn. Reson., Ser. A.* **1996**, *120*, 155–189.
- [94] Israelachvili, J. N. “Intermolecular and surface forces”, 3rd Ed., Academic Press, UK, 2011; Chapter 20.
- [95] Long, J. A.; Rankin, B. M.; Ben-Amotz, D. Micelle structure and hydrophobic hydration. *J. Am. Chem. Soc.* **2015**, *137*, 10809–10815.
- [96] Vorobiev, A. Kh.; Chumakova, N. A. Determination of orientation distribution function of anisotropic paramagnetic species by analysis of ESR spectra angular dependence. *J. Magn. Reson.* **2005**, *175*, 146–157.
- [97] Yankova, T. S.; Chumakova, N. A.; Pomogailo, D. A.; Vorobiev, A. Kh. Spin probe orientation distribution functions in aligned nematic liquid crystal. *Magn. Reson. Solids* **2011**, *13*, 10–13.
- [98] Molecular Imaging and Contrast Agent Database (MICAD) Internet, Bethesda (MD), National Center for Biotechnology Information (US), 2004–2013, <http://www.ncbi.nlm.nih.gov/books/NBK5330/>.
- [99] Malayeri, A. A.; Brooks, K.; Bryant, L. H.; Evers, R.; Kumar, P.; Reich, D. S.; Bluemke, D. A. NIH perspective on reports of gadolinium deposition in the brain. *J. Am. Coll. Radiol.* **2016**, *13*, 237–241.
- [100] Gale, E. M.; Caravan, P.; Rao, A. G.; McDonald, R. J.; Winfeld, M.; Fleck, R. J.; Gee, M. S. Gadolinium-based contrast agents in pediatric magnetic resonance imaging. *Pediatr. Radiol.* **2017**, *47*, 507–521.
- [101] Radbruch, A.; Weberling, L. D.; Kieslich, P. J.; Eidel, O.; Burth, S.; Kickingereider, P.; Heiland, S.; Wick, W.; Schlemmer, H. P.; Bendszus, M. Gadolinium retention in the dentate nucleus and globus pallidus is dependent on the class of contrast agent. *Radiology* **2015**, *275*, 783–791.
-

-
- [102] Kanda, T.; Fukusato, T.; Matsuda, M.; Toyoda, K.; Oba, H.; Kotoku, J.; Haruyama, T.; Kitajima, K.; Furui, S. Gadolinium-based contrast agent accumulates in the brain even in subjects without severe renal dysfunction: Evaluation of autopsy brain specimens with inductively coupled plasma mass spectroscopy. *Radiology* **2015**, *276*, 228–232.
- [103] Gulani, V.; Calamante, F.; Shellock, F. G.; Kanal, E.; Reeder, S. B. Gadolinium deposition in the brain: summary of evidence and recommendations. *Lancet. Neurol.* **2017**, *16*, 564–70.
- [104] Fraum, T. J.; Ludwig, D. R.; Bashir, M. R.; Fowler, K.J. Gadolinium-based contrast agents: A comprehensive risk assessment. *J. Magn. Reson. Imaging* **2017**, *46*, 338–353.
- [105] Afzal, V.; Brasch, R. C.; Nitecki, D. E.; Wolff, S. Nitroxyl spin label contrast enhancers for magnetic resonance imaging studies of acute toxicity and mutagenesis. *Invest. Radiol.* **1984**, *19*, 549–552.
- [106] Keana, J. F. W.; Pou, S.; Rosen, G. M. Nitroxides as potential contrast enhancing agents for MRI application: Influence of structure on the rate of reduction by rat hepatocytes, whole liver homogenate, subcellular fractions, and ascorbate. *Magn Reson Med.* **1987**, *3*, 83–88.
- [107] Saphier, O.; Silberstein, T.; Shames, A. I.; Likhtenshtein, G. I.; Maimon, E.; Mankuta, D.; Mazor, M.; Katz, M.; Meyerstein, D.; Meyerstein, N. The reduction of a nitroxide spin label as a probe of human blood antioxidant properties. *Free Radic. Res.* **2003**, *37*, 301–308.
- [108] Jiang, X.; Xin, H.; Ren, Q.; Gu, J.; Zhu, L.; Du, F.; Feng, C.; Xie, Y.; Sha, X.; Fang, X. Nanoparticles of 2-deoxy-D-glucose functionalized poly(ethyleneglycol)-co-poly(trimethylene carbonate) for dual-targeted drug delivery in glioma treatment. *Biomaterials* **2014**, *35*, 518–529.
- [109] Xiong, F.; Xiong, C.; Hua, X.; Shan, X.; Zhang, Y.; Gu, N. Preparation, characterization of 2-deoxy-D-glucose functionalized dimercaptosuccinic acid-coated maghemite nanoparticles for targeting tumor cells. *Pham. Res.* **2012**, *29*, 1087–1097.
- [110] Ranjbar-Navazi, Z.; Eskandani, M.; Johari-Ahar, M.; Nemati, A.; Akbari, H.; Davaran, S.; Omid, Y. Doxorubicin-conjugated D-glucosamine- and folate- bi-functionalised InP/ZnS quantum dots for cancer cells imaging and therapy. *J. Drug Target.* **2018**, *3*, 267–277.
- [111] Korotcov, A. V.; Ye, Y.; Chen, Y.; Zhang, F.; Huang, S.; Lin, S.; Sridhar, R.; Achilefu, S.; Wang, P. C. Glucosamine-linked near-infrared fluorescent probes for imaging of solid tumor xenografts. *Mol Imaging Biol.* **2012**, *14*, 443–451.
- [112] Uchida, Y.; Uematsu, T.; Nakayama, Y.; Takahashi, H.; Tsue, H.; Tanaka, K.; Tamura, R. Partial resolution of racemic trans-4-[5-(4-alkoxyphenyl)-2,5-dimethylpyrrolidine-1-oxyl-2-yl]benzoic acids by the diastereomer method with (R)- or (S)-1-phenylethylamine. *Chirality* **2008**, *20*, 282–287.
- [113] Uchida, Y.; Tamura, R.; Ikuma, N.; Shimono, S.; Yamauchi, J.; Aoki, Y.; Nohira, H. Synthesis and characterization of novel all-organic liquid crystalline radicals. *Mol. Cryst. Liq. Cryst.* **2007**, *479*, 1251–1259.
- [114] Zhang, Q.; Lebl, T.; Kulczynska, A.; Botting, N. P. The synthesis of novel hexa-¹³C-labelled glucosinolates from [¹³C₆]-D-glucose. *Tetrahedron* **2009**, *65*, 4781–4876.
- [115] Soli, E. D.; Manoso, A. S.; Patterson, M. C.; DeShong, P. Azide and cyanide displacements via hypervalent silicate intermediates. *J. Org. Chem.* **1999**, *64*, 3171–3177.
- [116] Muhizi, T.; Grelier, S.; Coma, V. Synthesis and antibacterial activity of aminodeoxyglucose derivatives against *Listeria innocua* and *Salmonella typhimurium*. *J. Agric. Food Chem.*, **2009**, *57*, 8770–8775.
- [117] European Food Safety Authority (EFSA). Opinion of the scientific panel on dietetic products, nutrition and allergies on a request from the commission related to the tolerable upper intake level of vitamin C (L-Ascorbic acid, its calcium, potassium and sodium salts and L-Ascorbyl-6-palmitate). *EFSA J.* **2004**, *59*, 1–21.
-

-
- [118] Hyodo, F.; Matsumoto, K.; Matsumoto, A.; Mitchell, J. B.; Krishna, M. C. Probing the intracellular redox status of tumors with magnetic resonance imaging and redox-sensitive contrast agents. *Cancer Res.* **2006**, *66*, 9921–9928.
- [119] Hyodo, F.; Chuang, K.H.; Goloshevsky, A.G.; Sulima, A.; Griffiths, G.L.; Mitchell, J.B.; Koretsky, A.P.; Krishna, M.C. Brain redox imaging using blood–brain barrier permeable nitroxide MRI contrast agent, *J. Cereb. Blood Flow Metab.* **2008**, *28*, 1165–1174.
- [120] Ma, Y.; Huang, J.; Song, S.; Chen, H.; Zhang, Z. Cancer-targeted nanotheranostics: Recent advances and perspectives. *Small* **2016**, *12*, 4936–4954.
- [121] Sumer, B.; Gao, J. Theranostic nanomedicine for cancer. *Nanomedicine* **2008**, *3*, 137–140.
- [122] Movassaghian, S.; Merkel, O. M.; Torchilin, V. P. Applications of polymer micelles for imaging and drug delivery. *Wiley Interdiscip. Rev.: Nanomed. Nanobiotechnol.*, **2015**, *7*, 691–707.
- [123] Rintoul, L.; Micallef, A. S.; Bottle, S. E. *Spectrochimica Acta Part A* **2008**, *70*, 713–717
- [124] Stable radicals Fundamental and Applied Aspects of Odd-Electron Compounds (Eds.: R. G. Higgs), John Wiley & Sons, Chichester, **2010**.

List of publications

1. Nagura, K.; Takemoto, Y.; Moronaga, S.; Uchida, Y.; Shimono, S.; Shiino, A.; Tanigaki, K.; Amano, T.; Yoshino, F.; Noda, Y.; Koizumi, S.; Komatsu, N.; Kato, T.; Yamauchi, J.; Tamura, R. Preparation of robust metal-free magnetic nanoemulsions encapsulating low-molecular-weight nitroxide radicals and hydrophobic drugs directed toward MRI-visible targeted delivery. *Chem. Eur. J.* **2017**, *23*, 15713–15720. (Chapter 2)
2. Nagura, K.; Bogdanov, A.; Chumakova, N.; Vorobiev, A. Kh.; Moronaga, S.; Imai, H.; Matsuda, T.; Noda, Y.; Maeda, T.; Koizumi, S.; Sakamoto, K.; Amano, T.; Yoshino, F.; Kato, T.; Komatsu, N.; Tamura, R. Size-tunable MRI-visible nitroxide-based magnetic mixed micelles: Preparation, stability and theranostic application. *Nanotechnology*, in press. (Chapter 3)
3. Nagura, K.; Takemoto, Y.; Yoshino, F.; Bogdanov, A.; Chumakova, N.; Vorobiev, A. Kh.; Imai, H.; Matsuda, T.; Shimono, S.; Kato, T.; Komatsu, N.; Tamura, R. Magnetic mixed micelles composed of a non-ionic surfactant and nitroxide radicals containing a D-glucosamine unit: Preparation, stability and biomedical application. *Pharmaceutics* **2019**, *11*, 42. (Chapter 4)

Patent

4. 田村類・名倉康太、“有機ニトロキシドラジカル化合物、その製造方法、ナノエマルジョン粒子及びその用途”、特願 2016-044450

Acknowledgement

The present study has been performed at Kyoto University under Prof. Emer. Rui Tamura and Prof. Naoki Komatsu. This work concerns with preparation and properties of nitroxide radicals in mixed micelles formed from a non-ionic surfactant.

First of all, the author appreciates to Prof. Emer. Tamura and Prof. Komatsu for their supports and advises. The author sincerely appreciates Prof. Satoru Hiroto and Prof. Tatsuhisa Kato for thoroughly and strictly checking the thesis. The author sincerely appreciates Prof. Andrey Kh. Vorobiev, Dr. Natalia Chumakova and Dr. Alexey Bogdanov for their many experimental supports including measurement and simulation of EPR spectra during his stay at Moscow State University. The author gives his deepest thanks to Prof. Hirohito Tsue and Dr. Hiroki Takahashi for their positive contributions to this work.

The author is deeply grateful to Dr. Akihiko Shiino, Dr. Kenji Tanigaki, Dr. Hirohiko Imai, Prof. Tetsuya Matsuda, Mr. Tsukuru Amano and Ms. Fumi Yoshino for MRI and toxicological experiments, and Dr. Yohei Noda and Prof. Satoshi Koizumi for SANS experiment. They kindly gave the author precious advises for this work. The author also sincerely appreciates Dr. Satoshi Shimono and Dr. Yusa Takemoto for kind advises. The author also thanks old and new members of the research group of Prof. Emer. Tamura and Prof. Komatsu.

Last but not the least, the author sincerely thanks his family for the continuous support, love and encouragement.